



Universiteit Gent
Faculteit Wetenschappen
Vakgroep Fysica en Sterrenkunde

² No title yet

³ No sub-title neither, obviously...

⁴ Alexis Fagot

5



Thesis to obtain the degree of
Doctor of Philosophy in Physics
Academic years 2012-2017



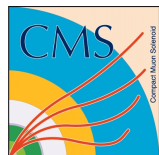


Universiteit Gent
Faculteit Wetenschappen
Vakgroep Fysica en Sterrenkunde

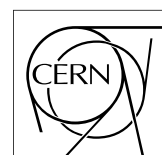
Promotoren: Dr. Michael Tytgat
Prof. Dr. Dirk Ryckbosch

Universiteit Gent
Faculteit Wetenschappen
Vakgroep Fysica en Sterrenkunde
Proeftuinstraat 86, B-9000 Gent, België
Tel.: +32 9 264.65.28
Fax.: +32 9 264.66.97

17



Thesis to obtain the degree of
Doctor of Philosophy in Physics
Academic years 2012-2017



Acknowledgements

¹⁹ Ici on remerciera tous les gens que j'ai pu croiser durant cette aventure et qui m'ont permis de passer
²⁰ un bon moment

²¹ *Gent, ici la super date de la mort qui tue de la fin d'écriture*
²² *Alexis Fagot*

Table of Contents

23

24	Acknowledgements	i
25	Nederlandse samenvatting	vii
26	English summary	ix
27	1 Introduction	1-1
28	1.1 A story of High Energy Physics	1-1
29	1.2 Organisation of this study	1-1
30	2 Investigating the TeV scale	2-1
31	2.1 The Standard Model of Particle Physics	2-2
32	2.1.1 A history of particle physics	2-2
33	2.1.2 Construction and test of the model	2-11
34	2.1.3 Investigating the TeV scale	2-12
35	2.2 The Large Hadron Collider & the Compact Muon Solenoid	2-14
36	2.2.1 LHC, the most powerful particle accelerator	2-14
37	2.2.1.1 Particle acceleration	2-15
38	2.2.2 CMS, a multipurpose experiment	2-19
39	2.2.3 High Luminosity LHC	2-22
40	2.3 Muon Phase-II Upgrade	2-24
41	3 Physics of Resistive plate chambers	3-1
42	3.1 Principle	3-1
43	3.1.1 Electron drift velocity	3-4
44	3.2 Rate capability and time resolution of Resistive Plate Chambers	3-4
45	3.2.1 Operation modes	3-4
46	3.2.2 Detector designs and performance	3-6
47	3.2.2.1 Double-gap RPC	3-7
48	3.2.2.2 Multigap RPC (MRPC)	3-8
49	3.2.2.3 Charge distribution and performance limitations	3-9
50	3.3 Signal formation	3-12
51	3.4 Gas transport parameters	3-12
52	4 Longevity studies and Consolidation of the present CMS RPC subsystem	4-1
53	4.1 Resistive Plate Chambers at CMS	4-1
54	4.1.1 Overview	4-1
55	4.1.2 The present RPC system	4-2
56	4.1.3 Pulse processing of CMS RPCs	4-3
57	4.2 Testing detectors under extreme conditions	4-4
58	4.2.1 The Gamma Irradiation Facilities	4-7

59	4.2.1.1	GIF	4-7
60	4.2.1.2	GIF++	4-9
61	4.3	Preliminary tests at GIF	4-11
62	4.3.1	Resistive Plate Chamber test setup	4-11
63	4.3.2	Data Acquisition	4-13
64	4.3.3	Geometrical acceptance of the setup layout to cosmic muons	4-13
65	4.3.3.1	Description of the simulation layout	4-14
66	4.3.3.2	Simulation procedure	4-16
67	4.3.3.3	Results	4-17
68	4.3.4	Photon flux at GIF	4-17
69	4.3.4.1	Expectations from simulations	4-17
70	4.3.4.2	Dose measurements	4-22
71	4.3.5	Results and discussions	4-23
72	4.4	Longevity tests at GIF++	4-24
73	4.4.1	Description of the Data Acquisition	4-27
74	4.4.2	RPC current, environmental and operation parameter monitoring	4-28
75	4.4.3	Measurement procedure	4-29
76	4.4.4	Longevity studies results	4-29
77	5	Investigation on high rate RPCs	5-1
78	5.1	Rate limitations and ageing of RPCs	5-1
79	5.1.1	Low resistivity electrodes	5-1
80	5.1.2	Low noise front-end electronics	5-1
81	5.2	Construction of prototypes	5-1
82	5.3	Results and discussions	5-1
83	6	Conclusions and outlooks	6-1
84	6.1	Conclusions	6-1
85	6.2	Outlooks	6-1
86	A	A data acquisition software for CAEN VME TDCs	A-1
87	A.1	GIF++ DAQ file tree	A-1
88	A.2	Usage of the DAQ	A-2
89	A.3	Description of the readout setup	A-3
90	A.4	Data read-out	A-3
91	A.4.1	V1190A TDCs	A-4
92	A.4.2	DataReader	A-6
93	A.4.3	Data quality flag	A-10
94	A.5	Communications	A-12
95	A.5.1	V1718 USB Bridge	A-13
96	A.5.2	Configuration file	A-13
97	A.5.3	WebDCS/DAQ intercommunication	A-17
98	A.5.4	Example of inter-process communication cycle	A-18
99	A.6	Software export	A-18
100	B	Details on the offline analysis package	B-1
101	B.1	GIF++ Offline Analysis file tree	B-1
102	B.2	Usage of the Offline Analysis	B-2
103	B.2.1	Output of the offline tool	B-3
104	B.2.1.1	ROOT file	B-3

105	B.2.1.2 CSV files	B-5
106	B.3 Analysis inputs and information handling	B-6
107	B.3.1 Dimensions file and IniFile parser	B-6
108	B.3.2 TDC to RPC link file and Mapping	B-7
109	B.4 Description of GIFT++ setup within the Offline Analysis tool	B-9
110	B.4.1 RPC objects	B-9
111	B.4.2 Trolley objects	B-10
112	B.4.3 Infrastructure object	B-11
113	B.5 Handeling of data	B-12
114	B.5.1 RPC hits	B-13
115	B.5.2 Clusters of hits	B-14
116	B.6 DAQ data Analysis	B-15
117	B.6.1 Determination of the run type	B-16
118	B.6.2 Beam time window calculation for efficiency runs	B-17
119	B.6.3 Data loop and histogram filling	B-18
120	B.6.4 Results calculation	B-19
121	B.6.4.1 Rate normalisation	B-19
122	B.6.4.2 Rate and activity	B-21
123	B.6.4.3 Strip masking tool	B-23
124	B.6.4.4 Output CSV files filling	B-25
125	B.7 Current data Analysis	B-29

¹²⁶

Nederlandse samenvatting –Summary in Dutch–

¹²⁸ Le resume en Neerlandais (j'aurais peut-être pu apprendre la langue juste pour ça...).

¹²⁷

English summary

¹³⁰ Le meme résume mais en Anglais (on commencera par la hein!).

List of Figures

131

132 2.1	Through the gold foil experiment Rutherford could show that most of the mass of atoms was contained in a positively charged nucleus and could then propose a more accurate atomic model than that of Thomson.	2-3
133		
134		
135 2.2	Figure 2.2a: Meson octet. Figure 2.2b: Baryon octet. Figure 2.2c: Baryon decuplet.	2-8
136		
137		
138 2.3	The elementary particles of the Standard Model are showed along with their names and properties. Their interactions with the strong, weak and electromagnetic forces have been explicated using color squares. In the left column, the scalar higgs boson is depicted, while the central is focused on the matter particles, the fermions, and the right on the force carriers, the gauge bosons. The role of the Higgs boson in electroweak symmetry breaking is highlighted, and the corresponding way properties of the various particles differ in the (high-energy) symmetric phase (top) and the (low-energy) broken-symmetry phase (bottom) are showed.	2-11
139		
140		
141		
142		
143		
144 2.4	CERN accelerator complex.	2-15
145		
146 2.5	Pictures of the different accelerators. From top to bottom: first the LINAC 2 and the <i>Pb</i> source of LINAC 3. Then the Booster and the LEIR. Finally, the PS, the SPS and the LHC.	2-17
147		
148 2.6	Figure 2.6a: schematics of the LHC cryodipoles. 1: Superconducting Coils, 2: Beam pipe, 3: Heat exchanger Pipe, 4: Helium-II Vessel, 5: Superconducting Bus-bar, 6: Iron Yoke, 7: Non-Magnetic Collars, 8: Vacuum Vessel, 9: Radiation Screen, 10: Thermal Shield, 11: Auxiliary Bus-bar Tube, 12: Instrumentation Feed Throughs, 13: Protection Diode, 14: Quadrupole Bus-bars, 15: Spool Piece Bus-bars. Figure 2.6b: magnetic field and resulting motion force applied on the beam particles.	2-18
149		
150		
151		
152		
153		
154 2.7	Figure 2.7a: picture of the LHC quadrupoles. Figure 2.7b: magnetic fields and resulting focussing force applied on the beam by 2 consecutive quadrupoles.	2-19
155		
156 2.8	Picture of the CMS barrel. The red outer layer is the muon system hosted into the red iron return yokes. The calorimeters are the blue cylinder inside in magnet solenoid and the tracker is the inner yellow cylinder built around the beam pipe.	2-20
157		
158		
159 2.9	View of the CMS apparatus and of its different components.	2-20
160		
161 2.10	Slice showing CMS sub-detectors and how particles interact with them.	2-21
162		
163 2.11	CMS tracker.	2-21
164		
165 2.12	Figure 2.12a: picture of the ECAL. Figure 2.12b: picture of the lead tungstate crystals composing the ECAL.	2-22
166		
167 2.13	CMS hadron calorimeter.	2-22
168		
169 2.14	Detailed timeline of for LHC and HL-LHC operation until 2028 and operation projection until 2038. This timeline only describes the operation plans after LS1.	2-23
170		
171 2.15	Absorbed dose in the CMS cavern after an integrated luminosity of 3000 fb. R is the transverse distance from the beamline and Z is the distance along the beamline from the Interaction Point at Z=0.	2-25
172		

170	2.16	A quadrant of the muon system, showing DTs (yellow), RPCs (light blue), and CSCs (green). The locations of new forward muon detectors for Phase-II are contained within the dashed box and indicated in red for GEM stations (ME0, GE1/1, and GE2/1) and dark blue for improved RPC (iRPC) stations (RE3/1 and RE4/1).	2-25
171			
172	2.17	RMS of the multiple scattering displacement as a function of muon p_T for the proposed forward muon stations. All of the electromagnetic processes such as bremsstrahlung and magnetic field effect are included in the simulation.	2-26
173			
174	3.1	Different phases of the avalanche development in the RPC gas volume subjected to a constant electric field E_0 . a) An avalanche is initiated by the primary ionisation caused by the passage of a charged particle through the gas volume. b) Due to its growing size, the avalanche starts to locally influence the electric field. c) The electrons, lighter than the cations reach the anode first. d) The ions reach the cathode. While the charges have not recombined, the electric field in the small region around the avalanche stays affected and locally blind the detector.	3-2
175			
176	3.2	Effeciency (circles and stars with 30 mV and 100 mV thresholds respectively) and streamer probability (opened circles) as function of the operating voltatge of a 2 mm single gap HPL RPC flushed with a gas mixture containing (a) 5%, (b) 2%, (c) 1% and (d) no SF_6 [33].	3-3
177			
178	3.3	Movement of the charge carriers in an RPC. Figure 3.3a: Voltage across an RPC whose electrode have a relative permittivity of 5 at the moment the tension s applied. Figure 3.3b: After the charge carriers moved, the electrodes are charged and there is no voltage drop over the electrodes anymore. The full potential is applied on the gas gap only. Figure 3.3c: The streamer discharge initiated by a charged particle transports electrons and cations towards the anode and cathode respectively.	3-5
179			
180	3.4	Typical oscilloscope pulses in streamer mode (Figure 3.4a) and avalanche mode(Figure 3.4b). In the case of streamer mode, the very small avalanche signal is visible.	3-5
181			
182	3.5	Rate capability comparison for the streamer and avalanche mode of operation. An order of magnitude in rate capability for a maximal efficiency drop of 10% is gained by using the avalanche mode over the streamer mode.	3-6
183			
184	3.6	Possible double-gap RPC layouts: a) "standard" 1D double-gap RPC, as used in CMS experiment, where the anodes are facing each other and a 1D read-out plane is sandwiched in between them, b) double read-out double-gap RPC as used in AT-LAS experiment, where the cathodes are facing each other and 2 read-out planes are used on the outer surfaces. This last layout can offer the possibility to use a 2D reconstruction by using orthogonal read-out planes.	3-7
185			
186	3.7	Comparison of performance of CMS double and single gap RPCs using cosmic muons [44]. Figure 3.7a: Comparison of efficiency sigmoids. Figure 3.7b: Voltage distribution at 95% of maximum efficiency. Figure 3.7c: $\Delta_{10\%}^{90\%}$ distribution.	3-7
187			
188	3.8	Presentation of ALICE MRPC using 250 μm gas gaps, 620 μm outer glass electrodes and 550 μm inner floating electrodes. More details on the labels are given in [45].	3-8
189			
190	3.9	Particle identification applied to electrons in the STAR experiment. The identification is performed combining ToF and dE/dx measurements [50].	3-9
191			
192	3.10	Comparison of the detector performance of ALICE ToF MRPC [51] at fixed applied voltage (in blue) and at fixed effective voltage (in red). The effective voltage is kept fixed by increasing the applied voltage accordingly to the current drawn by the detector.	3-9
193			
194	3.11	Ratio between total induced and drifting charge have been simulated for single gap, double-gap and multigap layouts [52]. The total induced charge for a double-gap RPC is a factor 2 higher than for a multigap.	3-10
195			
196			
197			
198			
199			
200			
201			
202			
203			
204			
205			
206			
207			
208			
209			
210			
211			
212			
213			
214			
215			
216			
217			

218	3.12 Charge spectra have been simulated for single gap, double-gap and multigap layouts [52]. It appears that when single gap shows a decreasing spectrum, double and multigap layouts exhibit a spectrum whose peak is detached from the origin. The detachment gets stronger as the number of gaps increases.	3-11
222	3.13 The maximal theoretical efficiency is simulated for single gap, double-gap and multi-gap layouts [52] at a constant gap thickness of 2 mm and using an effective Townsend coefficient of 9 mm^{-1}	3-11
225	4.1 Signals from the RPC strips are shaped by the FEE described on Figure 4.1a. Output LVDS signals are then read-out by a TDC module connected to a computer or converted into NIM and sent to scalers. Figure 4.1b describes how these converted signals are put in coincidence with the trigger.	4-3
229	4.2 Description of the principle of a CFD. A comparison of threshold triggering (left) and constant fraction triggering (right) is shown in Figure 4.2a. Constant fraction triggering is obtained thanks to zero-crossing technique as explained in Figure 4.2b. The signal arriving at the input of the CFD is split into three components. A first one is delayed and connected to the inverting input of a first comparator. A second component is connected to the noninverting input of this first comparator. A third component is connected to the noninverting input of another comparator along with a threshold value connected to the inverting input. Finally, the output of both comparators is fed through an AND gate.	4-4
238	4.3 (4.3a) Extrapolation from 2016 data of single hit rate per unit area in the barrel region. (4.3b) Extrapolation from 2016 data of single hit rate per unit area in the endcap region.	4-6
241	4.4 Background Fluka simulation compared to 2016 Data at $L = 10^{34} \text{ cm}^{-2} \cdot \text{s}^{-1}$ in the fourth endcap disk region. A mismatch in between simulation and data can be observed. [To be understood.]	4-7
244	4.5 Layout of the test beam zone called X5c GIF at CERN. Photons from the radioactive source produce a sustained high rate of random hits over the whole area. The zone is surrounded by 8 m high and 80 cm thick concrete walls. Access is possible through three entry points. Two access doors for personnel and one large gate for material. A crane allows installation of heavy equipment in the area.	4-8
249	4.6 ^{137}Cs decays by β^- emission to the ground state of ^{137}Ba (BR = 5.64%) and via the 662 keV isomeric level of ^{137}Ba (BR = 94.36%) whose half-life is 2.55 min.	4-9
251	4.7 Floor plan of the GIF++ facility. When the facility downstream of the GIF++ takes electron beam, a beam pipe is installed along the beam line (z-axis). The irradiator can be displaced laterally (its center moves from $x = 0.65 \text{ m}$ to 2.15 m), to increase the distance to the beam pipe.	4-9
255	4.8 Simulated unattenuated current of photons in the xz plane (Figure 4.8a) and yz plane (Figure 4.8b) through the source at $x = 0.65 \text{ m}$ and $y = 0 \text{ m}$. With angular correction filters, the current of 662 keV photons is made uniform in xy planes.	4-10
258	4.9 Description of the RPC setup. Dimensions are given in mm. A tent containing RPCs is placed at 1720 mm from the source container. The source is situated in the center of the container. RE-4-2-BARC-161 chamber is 160 mm inside the tent. This way, the distance between the source and the chambers plan is 2060 mm. Figure 4.9a provides a side view of the setup in the xz plane while Figure 4.9b shows a top view in the yz plane.	4-11

- 264 4.10 RE-4-2-BARC-161 chamber is inside the tent as described in Figure 4.9. In the top
265 right, the two scintillators used as trigger can be seen. This trigger system has an
266 inclination of 10° relative to horizontal and is placed above half-partition B2 of the
267 RPCs. PMT electronics are shielded thanks to lead blocks placed in order to protect
268 them without stopping photons from going through the scintillators and the chamber. 4-12
- 269 4.11 Hit distributions over all 3 partitions of RE-4-2-BARC-161 chamber is showed on
270 these plots. Top, middle and bottom figures respectively correspond to partitions A,
271 B, and C. These plots show that some events still occur in other half-partitions than
272 B2, which corresponds to strips 49 to 64, in front of which the trigger is placed, con-
273 tributing to the inefficiency of detection of cosmic muons. In the case of partitions
274 A and C, the very low amount of data can be interpreted as noise. On the other hand,
275 it is clear that a little portion of muons reach the half-partition B1, corresponding to
276 strips 33 to 48. 4-13
- 277 4.12 Results are derived from data taken on half-partition B2 only. On the 18th of June
278 2014, data has been taken on chamber RE-2-BARC-161 at building 904 (Prevessin
279 Site) with cosmic muons providing us a reference efficiency plateau of $(97.54 \pm$
280 $0.15)\%$ represented by a black curve. A similar measurement has been done at GIF
281 on the 21st of July with the same chamber giving a plateau of $(78.52 \pm 0.94)\%$
282 represented by a red curve. 4-14
- 283 4.13 Representation of the layout used for the simulations of the test setup. The RPC is
284 represented as a yellow trapezoid while the two scintillators as blue cuboids looking
285 at the sky. A green plane corresponds to the muon generation plane within the sim-
286 ulation. Figure 4.9a shows a global view of the simulated setup. Figure 4.9b shows
287 a zommed view that allows to see the 2 scintillators as well as the full RPC plane. . . 4-15
- 288 4.14 γ flux $F(D)$ is plot using values from table 4.1. As expected, the plot shows similar
289 attenuation behaviours with increasing distance for each absorption factors. 4-18
- 290 4.15 Figure 4.15a shows the linear approximation fit done via formulae 4.7 on data from
291 table 4.2. Figure 4.15b shows a comparison of this model with the simulated flux
292 using a and b given in figure 4.15a in formulae 4.4 and the reference value $D_0 =$
293 50cm and the associated flux for each absorption factor F_0^{ABS} from table 4.1 . . . 4-20
- 294 4.16 Dose measurements has been done in a plane corresponding to the tents front side.
295 This plan is 1900 mm away from the source. As explained in the first chapter, a
296 lens-shaped lead filter provides a uniform photon flux in the vertical plan orthogonal
297 to the beam direction. If the second line of measured fluxes is not taken into account
298 because of lower values due to experimental equipments in the way between the
299 source and the tent, the uniformity of the flux is well showed by the results. 4-22
- 300 4.17 4-23
- 301 4.18 Evolution of the maximum efficiency for RE2 (4.18a) and RE4 (4.18b) chambers
302 with increasing extrapolated γ rate per unit area at working point. Both irradiated
303 (blue) and non irradiated (red) chambers are shown. 4-25
- 304 4.19 Evolution of the working point for RE2 (4.19a) and RE4 (4.19b) with increasing
305 extrapolated γ rate per unit area at working point. Both irradiated (blue) and non
306 irradiated (red) chambers are shown. 4-25
- 307 4.20 Evolution of the maximum efficiency at HL-LHC conditions, i.e. a background hit
308 rate per unit area of 300 Hz/cm², with increasing integrated charge for RE2 (4.20a)
309 and RE4 (4.20b) detectors. Both irradiated (blue) and non irradiated (red) chambers
310 are shown. The integrated charge for non irradiated detectors is recorded during test
311 beam periods and stays small with respect to the charge accumulated in irradiated
312 chambers. 4-26

313	4.21 Comparison of the efficiency sigmoid before (triangles) and after (circles) irradiation for RE2 (4.21a) and RE4 (4.21b) detectors. Both irradiated (blue) and non irradiated (red) chambers are shown.	4-26
314		
315		
316	4.22 Evolution of the Bakelite resistivity for RE2 (4.22a) and RE4 (4.22b) detectors. Both irradiated (blue) and non irradiated (red) chambers are shown.	4-27
317		
318	4.23 Evolution of the noise rate per unit area for the irradiated chamber RE2-2-BARC-9 only.	4-27
319		
320	A.1 (A.1a) View of the front panel of a V1190A TDC module [58]. (A.1b) View of the front panel of a V1718 Bridge module [59]. (A.1c) View of the front panel of a 6U 6021 VME crate [60].	A-3
321		
322		
323	A.2 Module V1190A <i>Trigger Matching Mode</i> timing diagram [58].	A-4
324		
325	A.3 Structure of the ROOT output file generated by the DAQ. The 5 branches (<code>EventNumber</code> , <code>number_of_hits</code> , <code>Quality_flag</code> , <code>TDC_channel</code> and <code>TDC_TimeStamp</code>) are visible on the left panel of the ROOT browser. On the right panel is visible the histogram cor- responding to the variable <code>nHits</code> . In this specific example, there were approximately 50k events recorded to measure the gamma irradiation rate on the detectors. Each event is stored as a single entry in the <code>TTree</code>	A-10
326		
327		
328		
329		
330	A.4 The effect of the <code>quality_flag</code> is explained by presenting the content of <code>TBranch</code> <code>number_of_hits</code> of a data file without <code>Quality_flag</code> in Figure A.4a and the con- tent of the same <code>TBranch</code> for data corresponding to a <code>Quality_flag</code> where all TDCs were labelled as <code>GOOD</code> in Figure A.4b taken with similar conditions. It can be noted that the number of entries in Figure A.4b is slightly lower then in Figure A.4a due to the excluded events.	A-12
331		
332		
333		
334		
335		
336	A.5 Using the same data as previously showed in Figure A.4, the effect of the quality flag is explained by presenting the reconstructed hit multiplicity of a data file with- out <code>Quality_flag</code> in Figure A.5a and the reconstructed content of the same RPC partition for data corresponding to a <code>Quality_flag</code> where all TDCs were labelled as <code>GOOD</code> in Figure A.5b taken with similar conditions. The artificial high content of bin 0 is completely suppressed.	A-12
337		
338		
339		
340		
341		
342	A.6 WebDCS DAQ scan page. On this page, shifters need to choose the type of scan (Rate, Efficiency or Noise Reference scan), the gamma source configuration at the moment of data taking, the beam configuration, and the trigger mode. These in- formation will be stored in the DAQ ROOT output. Are also given the minimal measurement time and waiting time after ramping up of the detectors is over before starting the data acquisition. Then, the list of HV points to scan and the number of triggers for each run of the scan are given in the table underneath.	A-14
343		
344		
345		
346		
347		
348		
349	B.1 Example of expected hit time distributions in the cases of efficiency (Figure B.1a) and noise/gamma rate per unit area (Figure B.1b) measurements as extracted from the raw ROOT files. The unit along the x-axis corresponds to ns. The fact that "the" muon peak is not well defined in Figure B.1a is due to the contribution of all the RPCs being tested at the same time that don't necessarily have the same signal arrival time. Each individual peak can have an offset with the ones of other detectors. The inconsistancy in the first 100 ns of both time distributions is an artefact of the TDCs and are systematically rejected during the analysis.	B-16
350		
351		
352		
353		
354		
355		
356		
357	B.2 The effect of the quality flag is explained by presenting the reconstructed hit multi- plicity of a data file without <code>Quality_flag</code> . The artificial high content of bin 0 is the effect of corrupted data.	B-19
358		
359		

- 360 B.3 Display of the masking tool page on the webDCS. The window on the left allows the
361 shifter to edit `ChannelsMapping.csv`. To mask a channel, it only is needed to set the
362 3rd field corresponding to the strip to mask to 0. It is not necessary for older mapping
363 file formats to add a 1 for each strip that is not masked as the code is versatile and
364 the default behaviour is to consider missing mask fields as active strips. The effect
365 of the mask is directly visible for noisy channels as the corresponding bin turns red.
366 The global effect of masking strips will be an update of the rate value showed on the
367 histogram that will take into consideration the rejected channels. B-24

List of Tables

368

369	3.1 Properties of the most used electrode materials for RPCs.	3-4
370	4.1 Total photon flux ($E\gamma \leq 662$ keV) with statistical error predicted considering a	
371	^{137}Cs activity of 740 GBq at different values of the distance D to the source along	
372	the x-axis of irradiation field [55].	4-17
373	4.2 Correction factor c is computed thanks to formulae 4.5 taking as reference $D_0 =$	
374	50 cm and the associated flux F_0^{ABS} for each absorption factor available in table 4.1.	4-19
375	4.3 The data at D_0 in 1997 is taken from [55]. In a second step, using Equations 4.8	
376	and 4.9, the flux at D can be estimated in 1997. Then, taking into account the	
377	attenuation of the source activity, the flux at D can be estimated at the time of the	
378	tests in GIF in 2014. Finally, assuming a sensitivity of the RPC to γ $s = 2 \cdot 10^{-3}$,	
379	an estimation of the hit rate per unit area is obtained.	4-21
380	A.1 Inter-process communication cycles in between the webDCS and the DAQ through	
381	file string signals.	A-19

382

List of Acronyms

383

List of Acronyms

384

385

A

386

388 AFL

Almost Full Level

389

390

B

391

393 BARC

Bhabha Atomic Research Centre

394 BLT

Block Transfer

395 BNL

Brookhaven National Laboratory

396 BR

Branching Ratio

397

398

C

399

401 CAEN

Costruzioni Apparecchiature Elettroniche Nucleari S.p.A.

402 CERN

European Organization for Nuclear Research

403 CFD

Constant Fraction Discriminator

404 CMB

Cosmic Microwave Background

405 CMS

Compact Muon Solenoid

406 CSC

Cathode Strip Chamber

407

408

D

410

411 DAQ

Data Acquisition

412 DCS

Detector Control Software

413 DQM

Data Quality Monitoring

414 DT

Drift Tube

415

416

E

417

418

419 **ECAL** electromagnetic calorimeter

420

421 **F**

423

424 **FCC** Future Circular Collider

425 **FEE** Front-End Electronics

426 **FEB** Front-End Board

427

428

429 **G**

430

431 **GE-/-** Find a good description

432 **GE1/1** Find a good description

433 **GE2/1** Find a good description

434 **GEANT** GEometry ANd Tracking - a series of software toolkit platforms developed by CERN

435 **GEM** Gas Electron Multiplier

437 **GIF** Gamma Irradiation Facility

438 **GIF++** new Gamma Irradiation Facility

439

440

441 **H**

442

443 **HCAL** hadron calorimeter

444 **HL-LHC** High Luminosity LHC

445 **HPL** High-pressure laminate

446 **HV** High Voltage

447

448

449 **I**

450

451 **iRPC** improved RPC

452 **IRQ** Interrupt Request

453 **ISR** Intersecting Storage Rings

454

455

456 **L**

457

458 **LEIR** Low Energy Ion Ring

459 **LEP** Large Electron-Positron

460 **LHC** Large Hadron Collider

461 **LS1** First Long Shutdown

462	LS2	Second Long Shutdown
463	LS3	Third Long Shutdown
464	LV	Low Voltage
465	LVDS	Low-Voltage Differential Signaling

466

467

M

469

470	MC	Monte Carlo
471	MCNP	Monte Carlo N-Particle
472	ME-/	Find good description
473	ME0	Find good description
474	MRPC	Multigap RPC

475

476

N

478

479	NIM	Nuclear Instrumentation Module logic signals
-----	-----	--

480

481

P

483

484	PMT	PhotoMultiplier Tube
485	PS	Proton Synchrotron
486	PU	pile-up

487

488

Q

490

491	QCD	Quantum Chromodynamics
492	QED	Quantum Electrodynamics

493

494

R

496

497	RE-/	Find a good description
498	RE2/2	Find a good description
499	RE3/1	Find a good description
500	RE3/2	Find a good description
501	RE4/1	Find a good description
502	RE4/2	Find a good description
503	RE4/3	Find a good description
504	RMS	Root Mean Square

505 ROOT a framework for data processing born at CERN
506 RPC Resistive Plate Chamber

507

508

S

510

511 SC Synchrocyclotron
512 SLAC Stanford Linear Accelerator Center
513 SM Standard Model
514 SPS Super Proton Synchrotron
515 SUSY supersymmetry

516

517

T

519

520 TDC Time-to-Digital Converter
521 TDR Technical Design Report
522 ToF Time-of-flight

523

524

W

526

527 webDCS Web Detector Control System

1

Introduction

528

529

⁵³⁰ **1.1 A story of High Energy Physics**

⁵³¹ **1.2 Organisation of this study**

2

532

533

Investigating the TeV scale

534 „We may regard the present state of the universe as the effect of the
535 past and the cause of the future. An intellect which at any given mo-
536 ment knew all of the forces that animate nature and the mutual posi-
537 tions of the beings that compose it, if this intellect were vast enough
538 to submit the data to analysis, could condense into a single formula
539 the movement of the greatest bodies of the universe and that of the
540 lightest atom; for such an intellect nothing could be uncertain and
541 the future just like the past would be present before its eyes.”

542

543 - Pierre Simon de Laplace, *A Philosophical Essay on Probabilities*, 1814

544 Throughout history, physics experiment became more and more powerful in order to investigate
545 finer details of nature and helped understanding the elementary blocks of matter and the fundamental
546 interactions that bond them in the microscopic world. Nowadays, the Standard Model (SM) of
547 particle physics is the most accurate theory designed to explain the behaviour of particles and was
548 able to make very precise predictions that are constantly verified, although some hints of new physics
549 are visible as bricks are still missing to have a global comprehension of the Universe.

550 To highlight the limits of the SM and test the different alternative theories, ever more powerful
551 machines are needed. This is in this context that the Large Hadron Collider (LHC) has been thought
552 and built to accelerate and collide particles at energies exceeding anything that had been done be-
553 fore. Higher collision energies and high pile-up imply the use of enormous detectors to measure the
554 properties of the interaction products. The Compact Muon Solenoid (CMS) is a multipurpose ex-
555 periment that have been designed to study the proton-proton collisions of the LHC and give answers
556 on various high energy physics scenari. Nevertheless, the luminosity delivered by the collider will
557 in the future be increased to levels beyond the original plans to improve its discovery potential giv-
558 ing no choice to experiments such as CMS to upgrade their technologies to cope with the increased
559 radiation levels and detection rates.

560 **2.1 The Standard Model of Particle Physics**

561 In this early 21st century it is now widely accepted that matter is made of elementary blocks referred
562 to as *elementary particles*. The physics theory that classifies and describes the best the behaviour
563 and interaction of such elementary particles is the so called Standard Model that formalizes 3 of
564 the 4 fundamental interactions (electromagnetic, weak and strong interactions). It's development
565 took place during the 20th century thanks to a strong collaboration in between the theoretical and
566 experimental physicists.

567 **2.1.1 A history of particle physics**

568 The idea that nature is composed of elementary bricks, called *atomism*, is not contemporary as it
569 was already discussed by Indian or Greek philosophers during antiquity. In Greece, atomism has
570 been rejected by Aristotelianism as the existance of *atoms* would imply the existance of a void that
571 would violate the physical principles of Aristotle philosophy. Aristotelianism has been considered
572 as a reference in the european area until the 15th century and the italian *Rinascimento* where antic
573 text and history started to be more deeply studied. The re-discovery of Platon's philosophy would
574 allow to open the door to alternative theories and give a new approach to natural sciences where
575 experimentation would become central. A new era of knowledge was starting. By the begining of
576 the 17th century, atomism was re-discovered by philosophers and the very first attempt to estimate
577 an *atom* size would be provided by Magnetus in 1646. Although his *atoms* correspond to what would
578 nowadays be called *molecules*, Magnetus achieved feats by calculating that the number of molecules
579 in a grain of incense would be of the order of 10^{18} simply by considering the time necessary to smell
580 it everywhere in a large church after the stick was lit on. It is now known that this number only falls
581 short by 1 order of magnitude.

582 An alternative philosophy to atomism popularized by Descartes was corpuscularianism. Built on
583 ever divisible corpuscles, contrary to atoms, it's principles would be mainly used by alchemists like
584 Newton who would later develop a corpuscular theory of light. Boyle would combine together ideas
585 of both atomism or corpuscularianism leading to mechanical philosophy. The 18th century have

seen the development of engineering providing philosophical thought experiments with repeatable demonstration and a new point of view to explain the composition of matter and Lavoisier would greatly contribute to chemistry and atomism by publishing in 1789 a list of 33 chemical elements corresponding to what is now called *atoms*. In the early 19th century Dalton would summarize the knowledge on composition of matter and Fraunhofer would invent the spectrometer and discover the spectral lines. The rise of atomic physics, chemistry and mathematical formalism would unravel the different atomic elements and ultimately, the 20th century would see the very first sub-atomic particles.

Discovery of the inner structure of the atom

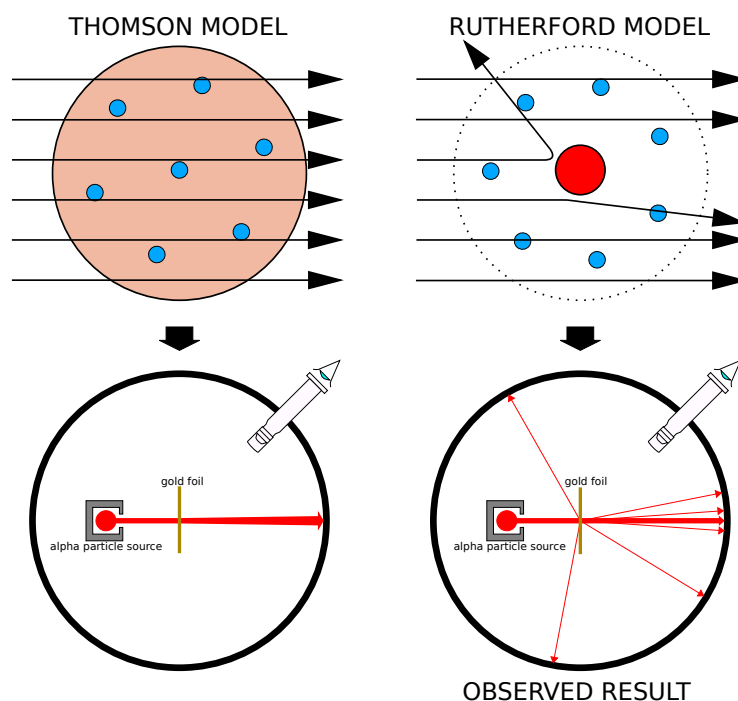


Figure 2.1: Through the gold foil experiment Rutherford could show that most of the mass of atoms was contained in a positively charged nucleus and could then propose a more accurate atomic model than that of Thomson.

The negative *electron* would be the first to be discovered in 1897 by Thomson after 3 decades of research on cathode rays by proving that the electrification observed in an electroscope, as reported by Perrin, was due to the rays themselves and that they had to be composed of electrically charged particles. In 1900, Becquerel would show the *beta rays* emitted by radium had the same charge over mass ratio than what measured by Thomson for cathode rays, pointing to electrons as a constituent of atoms. In 1907, Rutherford and Royds showed that *alpha* particles, once captured in a tube and subjected to an electric spark causing an electron avalanche, where helium ions as they could combine with 2 electrons to form a ${}^4\text{He}$. This discovery was directly followed by the constraint of the atom structure in 1909 through the gold foil experiment in which the deflection angle of alpha particles fired at a very thin gold foil was measured and highlighted atoms where mainly empty with

605 nearly all its mass contained into a tiny positively charged *nucleus*. With these two observations,
 606 he could formulate the Rutherford model of the atom in 1911, shown together with the Thomson
 607 plum pudding model in Figure 2.1. The link in between atomic number and number of positive and
 608 negative charges contained into the atoms would fast be understood and the different kind of element
 609 transmutation appeared to be purely nuclear processes making clear that the electromagnetic nature
 610 of chemical transformation could not possibly change nuclei. Thus a new branch in physics appeared
 611 to study nuclei exclusively: the nuclear physics.

612 Moreover, in 1913 quantum physics would be introduced into the atomic model by Bohr based
 613 on the assumptions of Plank to explain spectral lines, and other observed quantum effects. The same
 614 year, Moseley would confirm Bohr's model and Debye would extend it by introducing elliptical
 615 orbits.

616 By studying alpha emission and the product of their interaction with nitrogen gas, Rutherford
 617 reported in 1919 the very first nuclear reaction leading to the discovery that the hydrogen nucleus was
 618 composed of a single positively charged particle that was later baptised *proton*. This idea came from
 619 1815 Prout's hypothesis proposing that all atoms are composed of "*protyles*" (i.e. hydrogen atoms).
 620 By using scintillation detectors, Rutherford could highlight typical hydrogen nuclei signature and
 621 understand that the impact of alpha particles with nitrogen would knock out an hydrogen nucleus
 622 and produce an oxygen 17, as explicated in Formula 2.1 and would then postulate that protons are
 623 building bricks of all elements.



624 With this assumption and the discovery of isotopes together with Aston, elements with identical
 625 atomic number but different masses, Rutherford would propose that all elements' nuclei but hydrogen's are composed of both charged particles, protons, and of chargeless particles, which he called
 626 *neutrons*, and that these neutral particles would help maintaining nuclei as one, as charged protons
 627 were likely to electrostatically repulse each other, and introduced the idea of a new force, a *nuclear*
 628 force. Though the first idea concerning neutrons was a bond state of protons and electrons as it was
 629 known that the beta decay, emitting electrons, was taking place in the nucleus, it was then showed
 630 that such a model would hardly be possible due to Heisenberg's uncertainty principle and by the
 631 recently measured *spin* of both protons and electrons. The spin, discovered through the study of
 632 the emission spectrum of alkali metals, would be understood as a "two-valued quantum degree of
 633 freedom" and formalized by Pauli and extended by Dirac, to take the relativist case into account.
 634 Measured to be $\frac{1}{2}\hbar$ for both, it was impossible to arrange an odd number of half integer spins and
 635 obtain a global nucleus spin that would be integer. Finally, in 1932, following the discovery of a new
 636 neutral radiation, Chadwick could discover the neutron as an uncharged particle with a mass similar
 637 to that of the proton whose half integer spin would reveal to be the solution to explain the nuclear
 638 spin.
 639

640 Development of the Quantum Electrodynamics

641 Historically, the development of the quantum theory revolved around the question of emission and
 642 absorption of discrete amount of energy through light. Einstein used the initial intuition of Plank
 643 about the black-body radiation to develop in 1905 a model to explain the photoelectric effect in
 644 which light was described by discrete quanta now called *photons*. For this model, Einstein introduced
 645 the concept of wave-particle duality as classical theory was not able to describe the phenomenon.
 646 With the new understanding of atoms and of their structure, classical theories also proved unable

647 to explain atoms stability. Indeed, using classical mechanics, electrons orbiting around a nucleus
 648 should radiate an energy proportional to their angular momentum and thus lose energy through
 649 time and the spectrum of energy emission should then be continuous, but it was known since the
 650 19th century and the discovery of spectral lines that the emission spectrum of material was discrete.

651 This was Bohr who first suggested that a quantum description of the atom was necessary in 1913.
 652 Using the correspondence principle stating that at large enough numbers the quantum calculations
 653 should give the same results than the classical theory, he proposed the very first quantum model
 654 of the hydrogen atom explaining the line spectrum by introducing the principal quantum number
 655 n describing the electron shell. This model would then be improved by Sommerfeld that would
 656 quantize the z-component of the angular momentum, leading to the second and third quantum
 657 numbers, or azimuthal and magnetic quantum number, l and m defining for the second the orbital
 658 angular momentum of the electrons on their shells and thus, the shape of the orbital, and for the third
 659 the available orbital on the subshell for each electron. Nevertheless, although the model was not only
 660 limited to spherical orbitals anymore, making the atom more realistic, the Zeeman effect couldn't be
 661 completely explained by just using n , l and m . A solution would be brought after the discovery of
 662 Pauli in 1924, as Uhlenbeck, Goudsmit, and Kramers proposed in 1925 the idea of intrinsic rotation
 663 of the electron, introducing a new angular momentum vector associated to the particle itself, and
 664 not to the orbital, and associated to a new quantic number s , the *spin* projection quantum number
 665 explaining the lift of degeneracy to an even number of energy levels.

666 The introduction of the *spin* happened 1 year after another attempt of improvement of the theory
 667 was made by De Broglie in his PhD thesis. The original formulation of the quantum theory only
 668 considered photons as energy quanta behaving as both waves and particles. De Broglie proposed
 669 that all matter are described by waves and that their momentum is proportional to the oscillation of
 670 quantized electromagnetic field oscillators. This interpretation was able to reproduce the previous
 671 version of the quantum energy levels by showing that the quantum condition involves an integer
 672 multiple of 2π , as shown by Formula 2.2.

$$p = \hbar k \Leftrightarrow \int pdx = \hbar \int kdx = 2\pi\hbar n \quad (2.2)$$

673 Although the intuition of De Broglie about the wave-particle duality of all matter, his interpretation
 674 was semiclassical and it's in 1926 that the first fully quantum mechanical wave-equation would
 675 be introduced by Schrödinger to describe electron-like particles, reproducing the previous semiclassical
 676 formulation without inconsistencies. This complexe equation describes the evolution of the
 677 wave function Ψ of the quantum system, defined by its position vector \mathbf{r} and time t as an energy
 678 conservation law, in which the hamiltonian of the system \hat{H} is explicit, by solving the Equation 2.3.

$$i\hbar \frac{\partial}{\partial t} |\Psi(\mathbf{r}, t)\rangle = \hat{H} |\Psi(\mathbf{r}, t)\rangle \quad (2.3)$$

679 In 1927, Dirac would go further in his paper about emission and absorption of radiation by
 680 proposing a second quantization not only of the physical process at play but also of the electromagnetic
 681 field, providing the ingredients to the first formulation of *Quantum Electrodynamics (QED)*
 682 and the description of photon emission by electrons dropping into a lower energy state in which the
 683 final number of particles is different than the initial one. To complete this model to the many-body
 684 wave functions of identical particles, Jordan included creation and annihilation operators for fields
 685 obeying Fermi-Dirac statistics leading to a model describing particles that would be referred to as
 686 *fermions*. Nevertheless, in order to properly treat electromagnetism, the incorporation of the relativ-

687 ity theory developed by Einstein. Including gravity into quantum physics still is a challenge nowa-
 688 days, but in 1928 Pauli and Jordan would show that special relativity's coordinate transformations
 689 could be applied to quantum fields as the field commutators were Lorentz invariant. Finally derived
 690 the same year, the Dirac equation, shown as Equation 2.4, similarly to Schrödinger's equation, is a
 691 single-particle equation but it incorporates special relativity in addition to quantum mechanics rules.
 692 It features the 4×4 gamma matrices γ^μ built using 2×2 Pauli matrices and unitary matrix, the
 693 4-gradient ∂_μ , the rest mass m of any half integer spin massive particle described by the wave func-
 694 tion $\psi(x, t)$, also called a Dirac spinor, and the speed of light c . In addition to perfectly reproduce
 695 the results obtained with quantum mechanics so far, it also provided with *negative-energy solutions*
 696 that would later be interpreted as a new form of matter, *antimatter* and give a theoretical justifica-
 697 tion to the Pauli equation that was phenomenologically constructed to account for the spin as in the
 698 non-relativistic limit, the Dirac equation is similar.

$$i\hbar\gamma^\mu\partial_\mu\psi - mc\psi = 0 \quad (2.4)$$

699 The successes of the QED was soon followed with theoretical problems as computations of any
 700 physical process involving photons and charged particles were showed to be only reliable at the first
 701 order of perturbation theory. At higher order of the theory, divergent contributions were appearing
 702 giving nonsensical results. Only two effects were contributing to these infinities.

- 703 • The self-energy of the electron (or positron), the energy that the particle has due its own
 704 interaction with its environment.
- 705 • The vacuum polarization, virtual electron–positron pairs produced by a background electro-
 706 magnetic field in the vacuum which is not an "empty" space. These virtual pairs affect the
 707 charge and current distributions generated by the original electromagnetic field.

708 Solving this apparent problem was done by carefully defining the concepts of each observables,
 709 for example mass or charge, as these quantities are understood within the context of a non-interacting
 710 field equation, and that from the experiment point of view, they are abstractions as what is measured
 711 are "renormalized observables" shifted from there "bare" value by the interaction taking place in
 712 the measuring process. The infinities needed to be connected to corrections of mass and charge
 713 as those are fixed to finite values by experiment. This was the intuition of Bethe in 1947 who
 714 successfully computed the effect of such *renormalization* in the non-relativist case. Fully covariant
 715 formulations of QED including renormalization was achieved by 1949 by Tomonaga, Schwinger,
 716 Feynman and Dyson and Feynman is now famous for his association of diagrams to the term of
 717 the scattering matrix, greatly simplifying the representation and computation of interactions as the
 718 diagrams directly corresponded the measurable physical processes and would then be used in every
 719 quantum field theories. With the resolution of infinities, QED had mostly reached its final form,
 720 being still today the most accurate physical theory and would serve as a model to build all other
 721 quantum field theories.

722 Development of the quark model and Quantum Chromodynamics

723 To explain the nuclear force that holds *nucleons* (protons and neutrons) together, Yukawa theoreti-
 724 cally proposed in 1934 the existence of a force carrier called *meson* due to it's predicted mass in
 725 the range in between the electron and nucleon masses. Discovered in 1936 by Anderson and Ned-
 726 dermeyer, and confirmed using bubble chambers in 1937 by Street and Stevenson, a first meson

⁷²⁷ candidate was observed in the decay products of cosmic rays. Assuming it had the same electric
⁷²⁸ charge than electrons and protons, this particle was observed to have a curvature due to magnetic
⁷²⁹ field that was sharper than protons but smoother than electrons resulting in a mass in between that
⁷³⁰ of electrons and protons. But its properties were not compatible with Yukawa's theory, which was
⁷³¹ emphasized by the discovery of a new candidate in 1947, again in cosmic ray products using photo-
⁷³²graphic emulsions.

⁷³³ This new candidate, although it had a similar mass than the already believed *meson*, would rather
⁷³⁴ decay into it. For distinction, the first candidate would then be renamed "*mu meson*" when the second
⁷³⁵ would be the "*pi meson*". The *mu meson* was behaving like a heavy electron and didn't participate
⁷³⁶ in the strong interaction whereas the pion was believed to be the carrier of the nuclear interaction.
⁷³⁷ This lead to classify the *mu* in a new category of particles called *leptons* together with the electron
⁷³⁸ that shared similar properties and *the neutrino*, and be renamed *muon*. The *pi meson* was finally
⁷³⁹ found to be a triplet of particles: a positively charged, a negatively charged, and a neutral particle.
⁷⁴⁰ The neutral *pi meson* has been more difficult to identify as it wouldn't leave tracks on emulsions nor
⁷⁴¹ on bubble chambers and needed to be studied via it's decay products. It was ultimately identified in
⁷⁴² University of California's cyclotron in 1950 through the observation of its decay into 2 photons.

⁷⁴³ Also discovered in 1947 but in cloud chamber photographs, the *K meson* as also been an im-
⁷⁴⁴ portant step towards the establishment of the Standard Model. A triplet of particle, 2 charged and a
⁷⁴⁵ neutral, with a mass roughly half that of a proton, were reported. These particles were baptised *K*
⁷⁴⁶ *meson* in contrast to the "light" *pi* and *mu* "L-mesons". The particularity of the *K* were there very
⁷⁴⁷ slow decays with a typical lifetime of the order of 10^{-10} s much greater than the 10^{-23} s of *pi*-proton
⁷⁴⁸ reactions. The concept of *strangeness*, a new quantum number was then introduced by Pais as an
⁷⁴⁹ attempt to explain this phenomenon as *strange* particles appeared as a pair production of a strange
⁷⁵⁰ and anti-strange particle.

⁷⁵¹ With the development of synchrotrons, the particle *zoo* would grow to several dozens during the
⁷⁵² 1950s as higher energies were reachable through acceleration. In 1961, a first classification system,
⁷⁵³ called Eightfold Way, was proposed by Gell-Mann and finding its roots in the Gell-Mann–Nishijima
⁷⁵⁴ formula, which relates the electric charge *Q*, the third component of the isospin *I*₃, the *baryon*
⁷⁵⁵ number *B* and the strangeness *S*, as explicitated in Formula 2.5. The isospin was a quantum number
⁷⁵⁶ introduced in 1932 to explain symmetries of the newly discovered neutron using representation
⁷⁵⁷ theory of SU(2). The baryon number, was introduced by Nishijima as a quantum number for baryons,
⁷⁵⁸ i.e. particles of the same family as nucleons. The mesons were classified in an octet and baryons of
⁷⁵⁹ spin $\pm \frac{1}{2}$ and $\pm \frac{3}{2}$ were respectively classified into an octet and a decuplet, as shown in Figure 2.2. To
⁷⁶⁰ complete the baryon decuplet, Gell-Mann predicted the existance of baryon Ω^- which would later
⁷⁶¹ be discovered in 1964.

$$Q = I_3 + \frac{1}{2}(B + S) \quad (2.5)$$

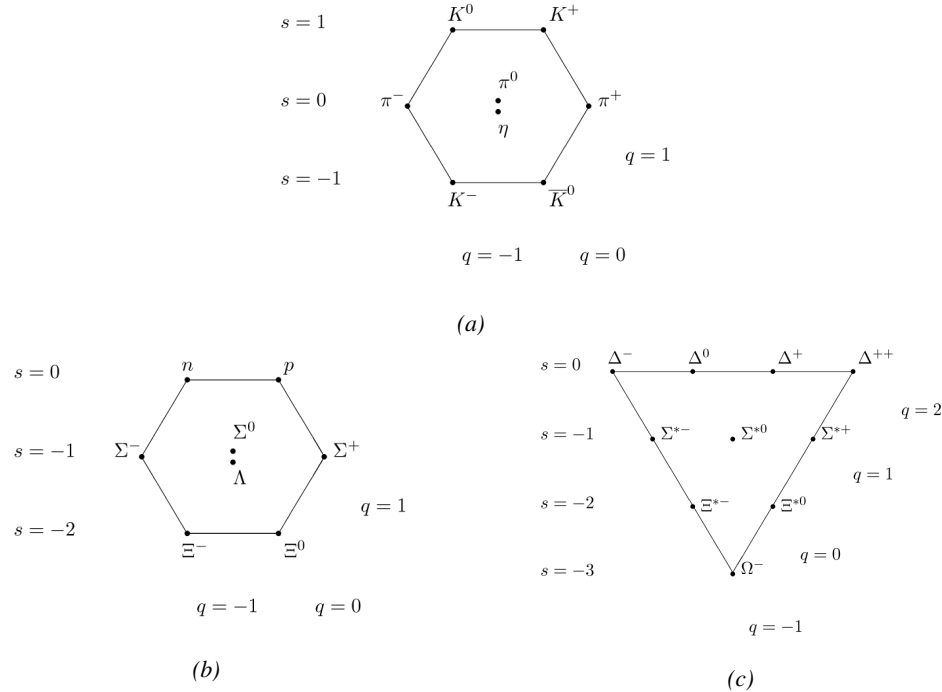


Figure 2.2: Figure 2.2a: Meson octet. Figure 2.2b: Baryon octet. Figure 2.2c: Baryon decuplet.

Strong of this classification using an SU(3) flavor symmetry, Gell-Mann, and independently Zweig, would propose a full theoretical model in which *hadrons* (strongly interacting particles, i.e. mesons and baryons) were not elementary particles anymore. They would rather be composed with 3 flavors of particles called *quarks* and there anti-particles. The 3 flavors were called *up*, *down* and *strange*. *Up* and *down* would be used to explain the nucleons and non-strange mesons, while *strange* would come into the composition of hadrons showing strangeness. *Up* and *down* flavors would be discovered in 1968 thanks to the deep inelastic scattering experiments conducted at the Stanford Linear Accelerator Center (SLAC), and *strange* could only be indirectly validated even though it provided a robust explanation to *kaon* (K) and *pion* (π). However, in the decade following the Gell-Mann-Zweig quark model proposition, several improvement to the model were brought, first by Glashow and Bjorken the same year that predicted the existence of a fourth quark flavor, the *charm*, that would equalize the then known number of quarks and leptons and finally in 1973 by Kobayashi and Maskawa that would increase the number of quarks to 6 to explain the experimental observation of CP violation. These two quarks would be referred to as *top* and *bottom* for the first time in 1975. It's only after these additions to the quark model that finally the *charm* would be discovered in 1974 at both SLAC and Brookhaven National Laboratory (BNL). A meson where the *charm* was bound with an *anti-charm*, called J/ψ , would help convince the physics community of the validity of the model. The *top* would be discovered soon after in 1977 in Fermilab and indicate the existence of the *bottom* that would resist to discovery until Fermilab's experiments CDF and D \emptyset in 1995 due to its very large mass and the energy needed to produce it.

As remarked by Struminsky, the original quark model proposal composed of 3 quarks should possess an additional quantum number due to mesons such as Ω^- or Δ^{++} . Indeed, these mesons are composed of 3 identical quarks, respectively 3 *strange* and *up* quark, with parallel spins, which

should be forbidden by the exclusion principle. Independentle, Greenberg and Han-Nambu proposed an additional SU(3) degree of freedom possessed by the quarks, that would later be refered to as *color charge gauge*, that could interact through *gluons*, the gauge boson octet corresponding to this degree of freedom. Nevertheless, as observing free quarks proved to be impossible, two visions of the quarks were argued mainly due to the failures to observe these particles free to prove their existence. On one side, Gell-Mann proposed to see quarks as mathematical construct instead of real particles, as they are always confined, implying that quantum field theory would not describe entirely the strong interaction. Opposed to this vision, Feynman on the contrary argued that quarks were real particles, that he would call *partons*, that should be described as all other particles by a distribution of position and momentum. The implications of quarks as point-like particles would be verified at SLAC and the concept of *color* would be added to the quark model in 1973 by Fritzsch and Leutwyler together with Gell-Mann to propose a description of the strong interaction through the theory of Quantum Chromodynamics (QCD). The discovery the same year of asymptotic freedom within the QCD by Groos, Politzer and Wilczek, allowed for very precise predictions thanks to the perturbation theory. Nowadays, the confinement of quarks is studied in experiments such as ALICE, through exploration of the quark-gluon plasma.

801 The Weak interaction, spontaneous symmetry breaking, the Higgs mechanism and the Elec- 802 troweak unification

The weak interaction is the process that causes radioactive decays. Thanks to the neutron discovery, Fermi could explain in 1934 the beta radiations through the beta decay process in which the neutron decays into a proton by emitting an electron. Though the missing energy observed during this process triggered a huge debate about the apparent non conservation of energy, momentum and spin of the process, Fermi, as Pauli before him, proposed that the missing energy was due to a neutral not yet discovered particle that would then be baptised *neutrino*. The impossibility to detect such a particle would leave some members of the scientific community sceptical, but hints of energy conservation and of the existence of the neutrino were provided by measuring the energy spectrum of electrons emitted through beta decay, as there was a strict limit on their energy. It's only 30 years later in 1953 that it would be discovered by the team of Cowan and Reines using the principle of inverse beta decay described through Formula 2.6. The experiment consisted in placing water tanks sandwiched in between liquid scintillators near a nuclear reactor with an estimated neutrino flux of $5 \times 10^{13} \text{ s}^{-1} \text{ cm}^{-2}$. However, in order to explain the absence of some reactions in the experiment of Cowan and Reines, and constraint the beta decay theory of Fermi and extend it to the case of the muon, Konopinski and Mahmoud proposed in 1953 that the muon decay would eject a particle similar to the neutrino and thus predicted the existence of a muon neutrino that would be different than the one involved in the beta decay, related to the electron. With this, the idea of lepton number would arise. The muon neutrino would successfully be detected in 1962 by Lederman, Schwartz and Steinberger.

$$\bar{\nu} + p \rightarrow n + e^+ \quad (2.6)$$

The theory could not be valid though as the probability of interaction, called cross-section, would have been increasing without bond with the square of the energy. Fermi assumed in a two vector current coupling but Lee and Yang noted that an axial current could appear and would violate parity. The experiment of Wu in 1956 would confirm the parity violation and Gamow and Teller would try to account for it by describing Fermi's interaction through allowed (parity-violating) and superallowed

827 (parity-conserving) decays. But the success of QED as a quantum field theory would spark the
828 development of such a theory to describe the weak interaction.

829 As previously discussed, the great success of QED was built on an underlying symmetry, inter-
830 preted as a gauge invariance so that the effect of the force is the same in all space-time coordinates,
831 and of the possibility to renormalize it in order to absorb the infinities. Independently in 1958,
832 Glashow, and Salam and Ward used 1957 Schwinger ideas about vector intermediary for the decay
833 processes, could find a way to unite both the electromagnetic and weak interaction into a gauge
834 theory involving 4 gauge bosons, 3 of which were massive and carried out the weak interaction and
835 a massless boson carrying the electromagnetic interaction. Among the 3 massive bosons, 2 were
836 charged and 1 was neutral, similarly to the previously theorized *pi meson* vector of the Yukawa
837 model and all have a mass much greater than nucleons and thus a very short life time implying a
838 finite very short range contrary to the contact interaction originally proposed by Fermi.

839 Breakthrough in other fields of physics contributed in giving theoretical support and interpreta-
840 tion to the unified electroweak theory. The stepping stone would be the use of spontaneous symmetry
841 breaking that was inspired to Nambu at the end of the 1950s following the development of the BCS
842 superconductivity mechanism in 1957. Cooper had shown that BCS pairs, pairs of electrons bound
843 together at low temperature, could have lower energy than the Fermi energy and where responsi-
844 ble for superconductivity. This lead to the discovery of Goldstone-Nambu bosons as a result of the
845 spontaneous breaking of the chiral symmetry in a theory describing nucleons and mesons devel-
846 opped by Nambu and Jona-Lasinio in 1961, and now understood as a low-energy approximation of
847 QCD. Similarly to mechanism of energy gap appearance in superconductivity, the nucleon mass
848 is suggested to the result of a self-energy of a fermion field and is studied through a four-fermion
849 interaction in which, as a consequence of the symmetry, bound states of nucleon-antinucleon pairs
850 appear and can be regarded as virtual pions. Though the symmetry is maintained in the equations,
851 the ground state is not preserved. Goldstone would later the same year show that the bound states
852 corresponds to spinless bosons with zero mass.

853 Although the model in itself didn't revolutionize particle physics, spontaneous symmetry break-
854 ing would be generalized to quantum field theories. As all fundamental interactions are described
855 using gauge theories based on underlying symmetries, processes such as the chiral symmetry break-
856 ing would be introduced soon after the publication of Nambu and Jona-Lasinio. In 1962, Anderson,
857 following an idea of Schwinger who suggested that zero-mass vector bosons were not necessarily
858 required to describe the conservation of baryons contrary to the bosons emerging from chiral sym-
859 metry breaking, discussed the implications of spontaneous symmetry breaking in particles physics.
860 A model was finally independently built in 1964 by Brout and Englert, Higgs, and Guralnik, Hagen,
861 and Kibble, who discovered that combining an additional field into a gauge theory in order to break
862 the symmetry, the resulting gauge bosons acquire a nonzero mass. Moreover, Higgs stated that this
863 implied the existence of at least one new massive, i.e. self-interacting, scalar boson, that are now
864 known as *Higgs bosons* corresponding to this additional field. The Higgs mechanism today specifi-
865 cally refers to the process through which the gauge bosons of the weak interaction acquire mass. In
866 1968, Weinberg could point to the Higgs mechanism to integrate a Higgs field into a new version
867 of the electroweak theory in which the spontaneous symmetry breaking mechanism of the Higgs
868 field would explicitly explain the masses of the weak interaction gauge bosons and the zero-mass
869 of photons.

2.1.2 Construction and test of the model

The Standard Model of particle physics was built in the middle of the 1970s after the experimental confirmation of the existence of quarks. It is based on the assembly of the models previously introduced and describing the fundamental interactions, except for gravitation, and their gauge bosons as well as the way elementary "matter" particles interact with the fields associated with these force carriers. In this sense, the development of QED and the unification of the electroweak interaction, of the Yukawa interaction and of QCD, and of the Higgs mechanism made it possible to explain most of contemporary physics.

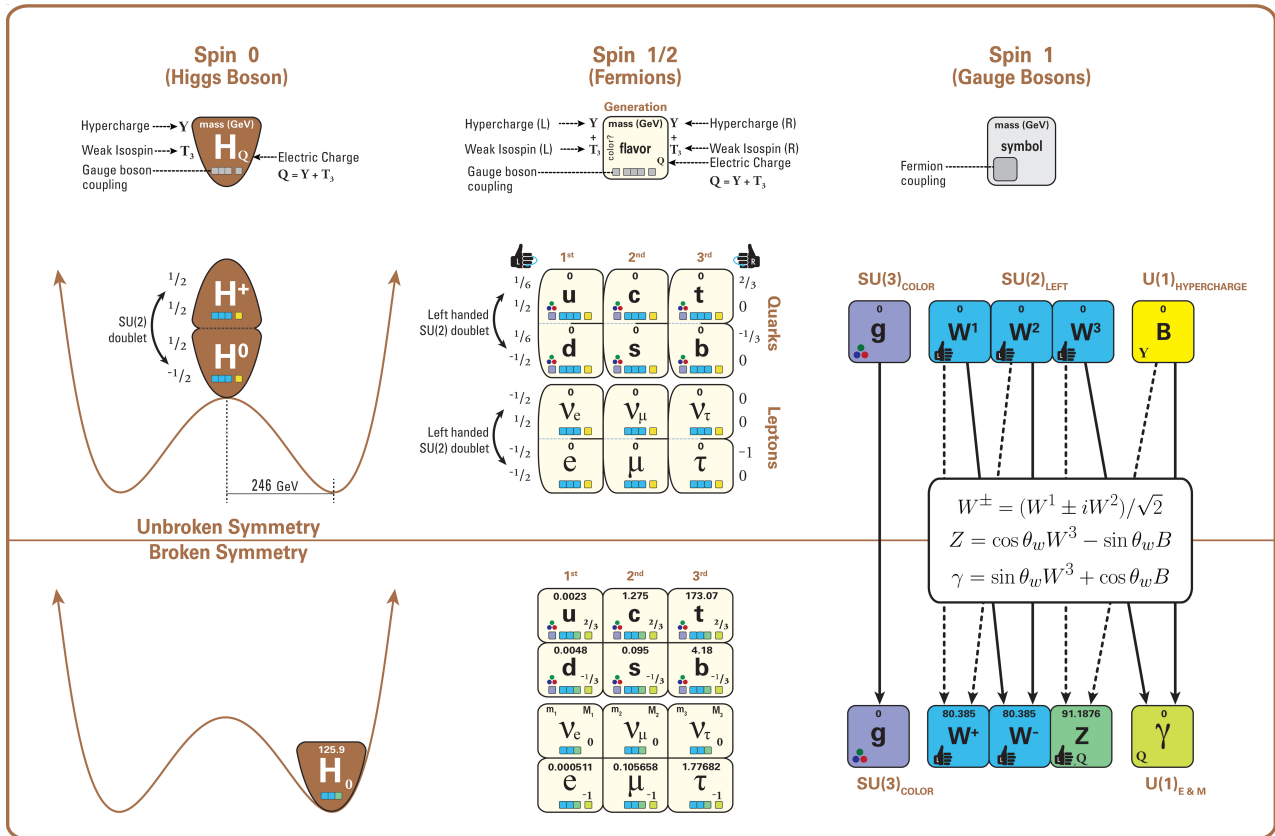


Figure 2.3: The elementary particles of the Standard Model are showed along with their names and properties. Their interactions with the strong, weak and electromagnetic forces have been explicited using color squares. In the left column, the scalar higgs boson is depicted, while the central is focused on the matter particles, the fermions, and the right on the force carriers, the gauge bosons. The role of the Higgs boson in electroweak symmetry breaking is highlighted, and the corresponding way properties of the various particles differ in the (high-energy) symmetric phase (top) and the (low-energy) broken-symmetry phase (bottom) are showed.

In the SM, "matter" particles, are described by 12 fermion fields of spin $\frac{1}{2}$ obeying the Fermi-Dirac statistics, i.e. subjected to the Pauli exclusion principle. To each fermion is associated its corresponding antiparticle. The fermions are classified according to the way they interact and, thus, according to the charges they carry. 6 of them are classified as quarks (u , d , c , s , t , and b) and are subjected to all interactions and the 6 others as leptons (e^- , μ^- , τ^- , ν_e , ν_μ , and ν_τ). Leptons

883 are not subjected to the strong interaction and among them, the 3 neutrinos only interact weakly as
 884 they are neutral particles, which explains why they are so difficult to detect. The gauge boson fields
 885 are the gluons g for the strong interaction, the photon γ for the electromagnetic interaction and the
 886 weak bosons W^+ , W^- , and Z^0 for the weak interaction. Finally, the Higgs field H^0 is responsible,
 887 through the spontaneous symmetry breaking, of the mixing of the massless electroweak boson fields
 888 W_1 , W_2 , W_3 , and B leading to the observable states γ , W^+ , W^- , and Z^0 that can gain mass while
 889 interacting with the Higgs field. This picture of the SM is summarized through Figure 2.3 where the
 890 antifermions are not showed.

891 When the model was first finalized, the existence of the weak gauge bosons, of the charm, of the
 892 third quark generation composed of top and bottom quarks to explain the observed CP violation was
 893 not proven but the predictions were measured with good precision in the years following. First, the
 894 charm quark would be discovered in 1974, followed by the bottom quark in 1977. The weak bosons
 895 would be discovered during the next decade in 1983. The top quark would resist until 1995 due to
 896 its very large mass but would offer the last piece of the elementary QCD particles. The very last
 897 predicted elementary particle of the model that was not observed yet would prove to be very difficult
 898 to observe. the Higgs boson needed the start of the LHC to finaly be oberved in 2012. A few years
 899 more of tests were necessary to measure its properties to confirm the observation of a scalar boson
 900 compatible with the predicted Higgs boson H^0 . Eventhough only quark-antiquark (mesons) and 3
 901 quark states (baryons) were observed, exotic hadrons were not forbidden by QCD and no limit of
 902 quark is imposed by the theory. Moreover, gluons could form bond states by themselves and with
 903 quarks. These two types of states are called *glueballs* and *hybrid hadrons*. For decades, experi-
 904 ments have been conducted without confirmation of such possible states existing. Nevertheless, in
 905 2014, tetraquarks were observed by LHCb, one of LHC's main experiments, and in 2015, the same
 906 experiment reported the discovery of pentaquarks making the SM one of the best tested theories of
 907 physics.

908 2.1.3 Investigating the TeV scale

909 Even though the SM is a well tested theory, several hints of physics going beyond its scope have
 910 been observed. First of all, gravity is not explained through this model and huge difficulties are en-
 911 countered when trying to include gravitation. The strength of gravitational interaction is expected to
 912 be negligible at the scale of elementary particles, nevertheless, adding gravitation in the perspective
 913 of developing a "theory of everything" leads to divergent integrals that could not be fixed through
 914 renormalization.

915 Moreover, the SM considers neutrinos to be massless but it was shown in the late 1960s by the
 916 Homestake experiment that the flux of solar neutrinos (i.e. ν_e) measured didn't match the predicted
 917 values due to neutrino oscillations, confirmed in the early 2000s by the Sudbury Neutrino Obser-
 918 vatory. This oscillation implies that neutrinos that can be observed are a superposition of massive
 919 neutrino states. The research on neutrino oscillation is already quite advanced with experiments
 920 looking at atmospheric, reactor or beam neutrinos in order to determine the elements of the mixing
 921 matrix similar to the CKM matrix describing the mixing of quarks. Nevertheless, no answer to the
 922 origin of neutrino mass is provided.

923 Another intriguing fact is that the universe is dominated by matter. However, the SM predicted
 924 that matter and antimatter should have been created in equal amounts and no mechanism is able to
 925 explain this matter-antimatter asymmetry. Although this asymmetry is seen from the visible uni-
 926 verse, it may be possible that other unknown regions of the Universe are dominated by antimatter.

927 Another possibility to explain the apparent asymmetry would be the existence of a electric dipole
928 in any fundamental particle that would permit matter and antimatter particles to decay at different
929 rates.

930 The discrepancy of velocity dispersion of stars in galaxies with respect to the visible mass they
931 contain is known since the end of the 19th century where Kelvin proposed that this problem could
932 be solved if a "*great majority of [the stars] would be dark bodies*". Throughout the 20th century,
933 physicists like Kapteyn, Zwicky, showed the first hints of a "*dark matter*" by studying star veloc-
934 ities and galactic clusters, followed by robust measurements of galaxy rotation curves by Babcock
935 which suggested that the mass-to-luminosity ratio was different from what would be expected from
936 watching the visible light. Later in the 1970s, Rubin and Ford from direct light observations and
937 Rogstad and Shostak from radio measurements showed that the radial velocity of visible objects in
938 galaxies was increasing with increasing distance to the center of the galaxy. Finally observation of
939 lensing effect by galaxy clusters, temperature distribution of hot gas in galaxies and clusters, and
940 the anisotropies in the Cosmic Microwave Background (CMB) kept on pointing to a "*dark matter*".
941 From all the data accumulated, the visible matter would only account to no more than 5% of the total
942 content on the visible universe. Alternative theories have tried to investigate modified versions of
943 the General Relativity as this theory is only well tested at the scale of the solar system but is not suf-
944 ficiently tested on wider ranges or even theories in which gravitation is not a fundamental force but
945 rather an emergent one, but so far, such theories have difficulties to reproduce all the experimental
946 observations as easily as through dark matter.

947 A possible theory to offer dark matter candidates would be supersymmetry (SUSY) which pro-
948 poses a relationship in between bosons and fermions. In this model, each elementary particle,
949 through a spontaneous spacetime symmetry breaking mechanism would have a *super partner* from
950 the other family of particles. On top of providing heavy dark matter candidates, supersymmetry
951 could also help solving the *Hierarchy problem*, the very large scale difference in between the weak
952 interaction and gravity, although, as mentioned before, in the case gravity is found not to be a funda-
953 mental force, this problem would automatically fade.

954

955 All these different aspects of physics beyond the Standard Model of particle physics and the
956 Standard model itself can be tested through the use of very energetic and intense hadron and ion col-
957 liders. The LHC at CERN is a perfect tool to seek answers to these open questions except maybe for
958 the gravity as gravity is extremely weak at particles level. For example, one of LHCb experiment's
959 goal is to investigate CP-violation and thus baryonic asymmetry. In 2017, the collaboration has an-
960 nounced to have so far a 3.3σ statistical significance over a CP-violation through the study of the
961 decays of Λ_b^0 and $\overline{\Lambda}_b^0$ into a proton (or antiproton) and 3 pions. Many analysis teams are also working
962 hard on supersymmetry both in ATLAS and CMS collaborations, the two multipurpose experiments
963 of LHC, even though no evidence of a supersymmetrical theory was seen, the few hint having the
964 tendency to confirm the standard model. These experiments also have the possibility to investigate
965 ways to explain Majorana neutrino mass through Yukawa interactions of scalar particles.

966 The higher the center-of-mass energy, the smaller details the experiments will be able to see, the
967 heavier the potential particle creation barrier will be, the stronger the cross-section of certain rare
968 decay channels will be. As a comparison, with collisions happening at 14 TeV, the LHC is approxi-
969 mately 2 orders of magnitude more sensitive to the Higgs than the Tevatron was with its already very
970 powerful 2 TeV. All these advantages eventually lead to new discoveries and deeper understanding
971 of the models describing our Universe. But the LHC only is a step forward to gather more precise
972 tests of the Standard Model and new knowledge about the physics beyond it. A successful physics

973 campaign will probably serve to justify the building of new accelerators with even greater discovery
 974 potential like for example the Future Circular Collider (FCC) that would push even further the study
 975 of the unanswered questions of contemporary physics.

976 2.2 The Large Hadron Collider & the Compact Muon Solenoid

977 Throughout its history, CERN has played a leading role in high energy particle physics. Large re-
 978 gional facilities such as CERN were thought after the second world war in an attempt to increase
 979 international scientific collaboration and allows scientists to share the forever increasing costs of
 980 experiment facilities required due to the need for increasing the energy in the center of mass to
 981 deeper probe matter. The construction of the first accelerators at the end of the 50s, the Synchro-
 982 cyclotron (SC) and the Proton Synchrotron (PS), was directly followed by the first observation of
 983 antinuclei in 1965 [1]. Strong from the experience of the Intersecting Storage Rings (ISR), the very
 984 first proton-proton collider that showed hints that protons are not elementary particles, the Super
 985 Proton Synchrotron (SPS) was built in the 70s to investigate the structure of protons, the preference
 986 for matter over antimatter, the state of matter in the early universe or exotic particles, and lead to
 987 the discovery in 1983 of the W and Z bosons [2–5]. These newly discovered particles and the elec-
 988 troweak interaction would then be studied in details by the Large Electron-Positron (LEP) collider
 989 that will help to prove in 1989 that there only are three generations of elementary particles [6]. The
 990 LEP would then be dismantled in 2000 to allow for the LHC to be constructed in the existing tunnel.

991 2.2.1 LHC, the most powerful particle accelerator

992 The LHC has always been considered as an option to the future of CERN. At the moment of the
 993 construction of the LEP beneath the border between France and Switzerland, the tunnel was built in
 994 order to accomodate what would be a Large Hadron Collider with a dipole field of 10 T and a beam
 995 energy in between 8 and 9 TeV [7] directly followed in 1985 with the creation of a 'Working Group
 996 on the Scientific and Technological Future of CERN' to investigate such a collider [8]. The decision
 997 was finally taken almost 10 years later, in 1994, to construct the LHC in the LEP tunnel [9] and the
 998 approval of the 4 main experiments that would take place at the 4 interaction points would come in
 999 1997 [10] and 1998 [11]:

- 1000 • ALICE [12] has been designed in the purpose of studying quark-gluon plasma that is believed
 1001 to have been a state of matter that existed in the very first moment of the universe.
- 1002 • ATLAS [13] and CMS [14] are general purpose experiments that have been designed with
 1003 the goal of continuing the exploration of the Standard Model and investigate new physics.
- 1004 • LHCb [15] has been designed to investigate the preference of matter over antimatter in the
 1005 universe through the CP violation.

1006 These large scale experiments, as well as the full CERN accelerator complex, are displayed on
 1007 Figure 2.4. The LHC is a 27 km long hadron collider and the most powerful accelerator used for
 1008 particle physics since 2008 [16]. The LHC was originally designed to collide protons at a center-
 1009 of-mass energy of 14 TeV and luminosity of $10^{34} \text{ cm}^{-2}\text{s}^{-1}$, as well as Pb ions at a center-of-mass
 1010 energy of 2.8 TeV/A with a peak luminosity of $10^{27} \text{ cm}^{-2}\text{s}^{-1}$. Run 1 of LHC, when the center-of-
 1011 mass energy only was half of the nominal LHC energy, was enough for both CMS and ATLAS to

discover the Higgs boson [17] and for LHCb to discover pentaquarks [18] and confirm the existance of tetraquarks [19]. Nevertheless, after the Third Long Shutdown (LS3) (2024-2026), the accelerator will be in the so called High Luminosity LHC (HL-LHC) configuration [20], increasing its instantaneous luminosity to $10^{35} \text{ cm}^{-2}\text{s}^{-1}$ for pp collisions and to $4.5 \times 10^{27} \text{ cm}^{-2}\text{s}^{-1}$, boosting the discovery potential of the LHC. The HL-LHC phase should last at least another 10 years depending on the breakthrough this machine would lead to. Already a new accelerating device, the FCC, as been proposed to prepare the future of high energy physics after the LHC.

CERN's Accelerator Complex

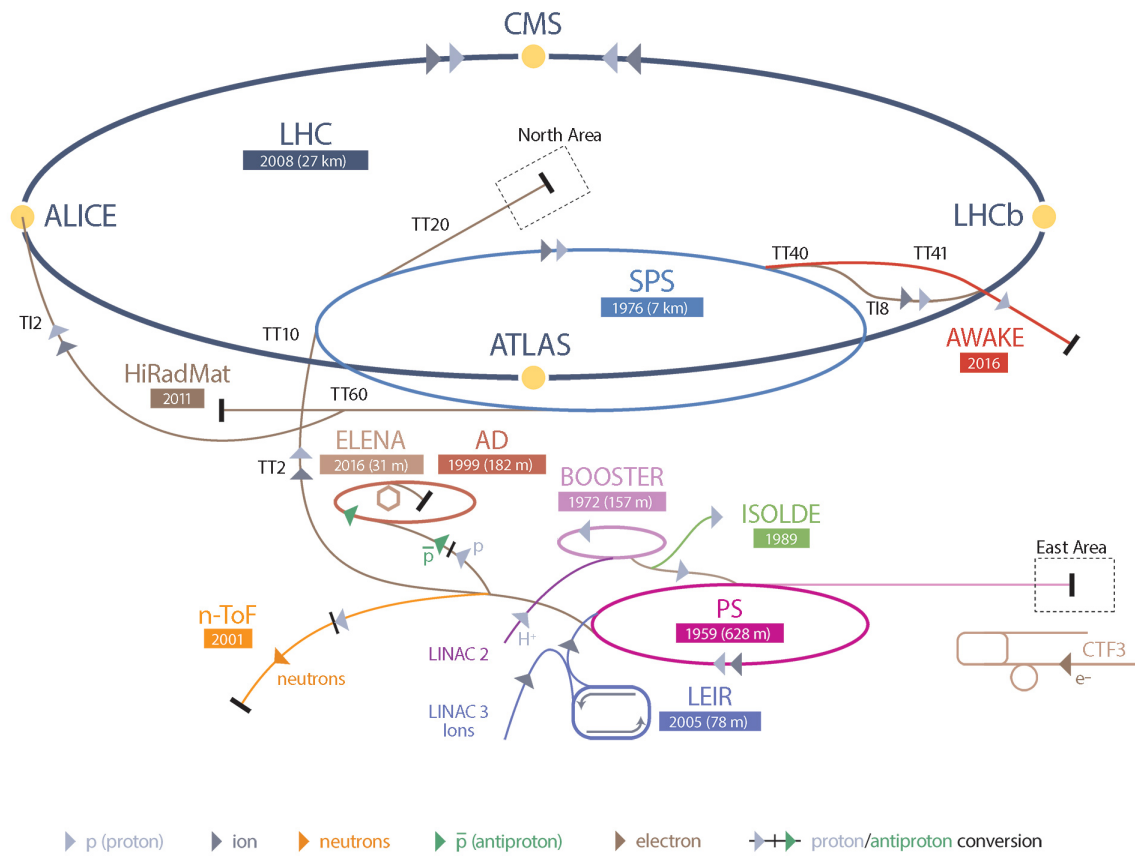


Figure 2.4: CERN accelerator complex.

2.2.1.1 Particle acceleration

The LHC is the last of a long series of accelerating devices. Before being accelerated by the LHC, the particles need to pass through different acceleration stages. All these acceleration stages are visible on Figure 2.4 and pictures of the accelerators are showed in Figure 2.5.

The story of accelerated protons at CERN starts with a bottle of hydrogen gas injected into the source chamber of the linear particle accelerator *LINAC 2* in which a strong electric field strips the

1026 electron off the hydrogen molecules only to keep their nuclei, the protons. The cylindrical conductors,
1027 alternatively positively or negatively charged by radiofrequency cavities, accelerate protons by
1028 pushing them from behind and pulling them from the front and ultimately give them an energy of
1029 50 MeV, increasing their mass by 5% in the process.

1030

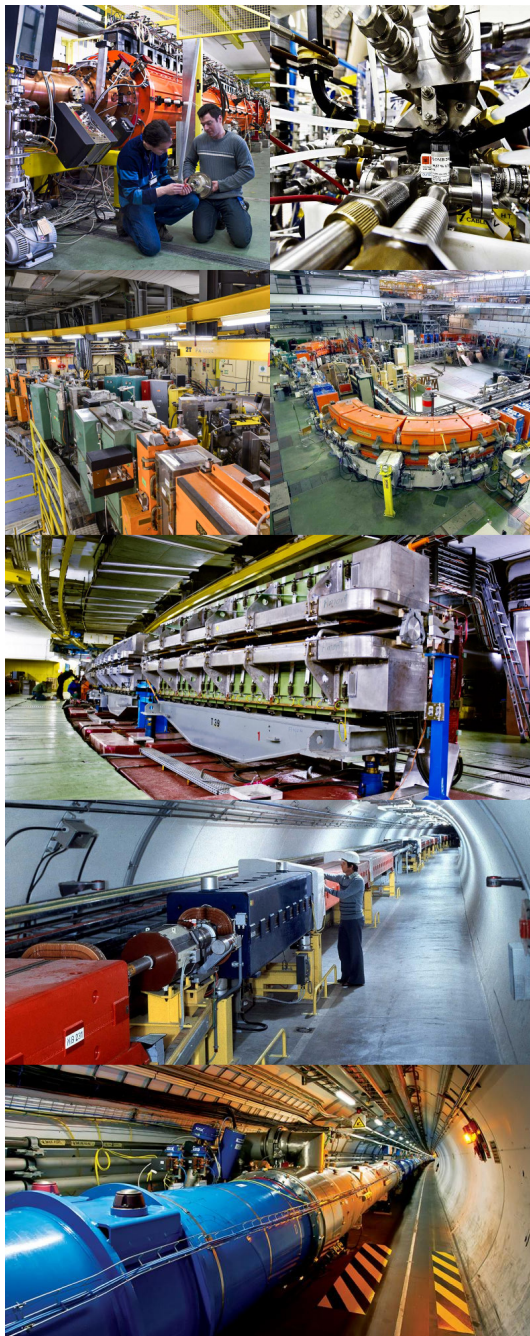


Figure 2.5: Pictures of the different accelerators. From top to bottom: first the LINAC 2 and the Pb source of LINAC 3. Then the Booster and the LEIR. Finally, the PS, the SPS and the LHC.

When exiting the LINAC 2, the protons are divided into 4 bunches and injected into the 4 superimposed synchrotron rings of the *Booster* where they are then accelerated to reach an energy of 1.4 GeV before being injected into the *PS*. Before the Booster was operational in 1972, the protons were directly injected into the *PS* from the LINAC 2 but the low injection energy limited the amount

of protons that could be accelerated at once by the PS. With the Booster, the PS accepts approximately 100 times more particles.

1037

The 4 proton bunches are thus sent as one to the PS where their energy eventually reaches 26 GeV. Since the 70s, the main goal of this 628 m circumference synchrotron has been to supply other machines with accelerated particles. Nowadays, not only the PS accelerates protons, it also accelerates heavy ions from the *Low Energy Ion Ring (LEIR)*. Indeed, the LHC experiments are not only designed to study *pp*-collisions but also *Pb*-collisions. Lead is first injected into the dedicated linear collider *LINAC 3*, that accelerate the ions using the same principle than *LINAC 2*. Electrons are stripped off the lead ions all along the acceleration process and eventually, only bare nuclei are injected in the LEIR whose goal is to transform the long ion pulses received into short dense bunches for LHC. Ions injected and stored in the PS were accelerated by the LEIR from 4.2 MeV to 72 MeV.

1047

Directly following the PS, is finally the last acceleration stage before the LHC, the 7 km long *SPS*. The SPS accelerates the protons to 450 GeV and inject proton in both LHC accelerator rings that will increase their energy up to 7 TeV. When the LHC runs with heavy lead ions for ALICE and LHCb, ions are injected and accelerated to reach the energy of 2.8 TeV/A.

1052

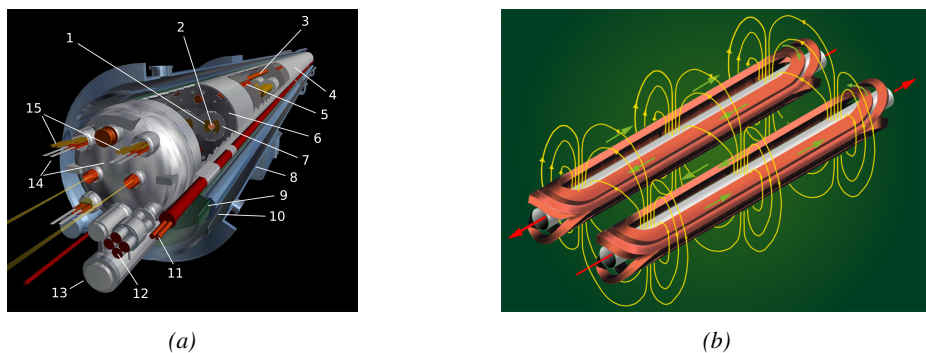


Figure 2.6: Figure 2.6a: schematics of the LHC cryodipoles. 1: Superconducting Coils, 2: Beam pipe, 3: Heat exchanger Pipe, 4: Helium-II Vessel, 5: Superconducting Bus-bar, 6: Iron Yoke, 7: Non-Magnetic Collars, 8: Vacuum Vessel, 9: Radiation Screen, 10: Thermal Shield, 11: Auxiliary Bus-bar Tube, 12: Instrumentation Feed Throughs, 13: Protection Diode, 14: Quadrupole Bus-bars, 15: Spool Piece Bus-bars. Figure 2.6b: magnetic field and resulting motion force applied on the beam particles.

1053

The LHC beams are not continuous and are rather organised in bunch of particles. When in *pp*-collision mode, the beams are composed of 2808 bunches of 1.15×10^{11} protons separated by 25 ns. When in *Pb* collision mode, the 592 *Pb* bunches are on the contrary composed of 2.2×10^8 ions separated by 100 ns. The two parallel proton beams of the LHC are contained in a single twin-bore magnet due to the space restriction in the LEP tunnel. Indeed, building 2 completely separate accelerator rings next to each other was impossible. The dipoles of the 1232 twin-bore magnets are showed in Figure 2.6 alongside the magnetic field generated along the dipole section to accelerate the particles. The dipoles generate a nominal field of 8.33 T, needed to give protons and lead nucleons their nominal energy. Some 392 quadrupoles, presented in Figure 2.7, are also used to focus to the beams, as well as other multipoles to correct smaller imperfections.

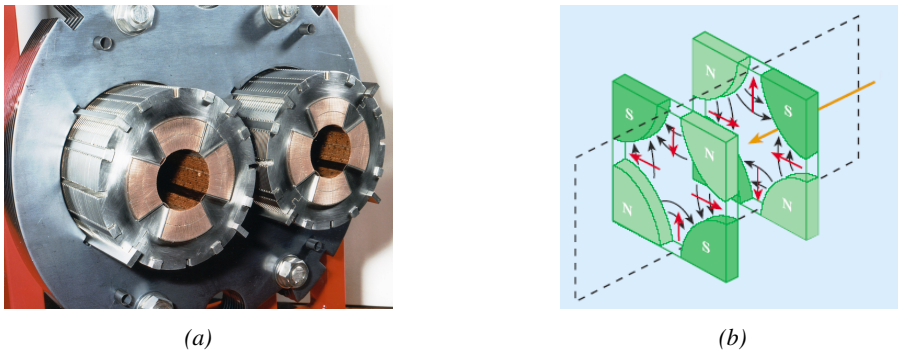


Figure 2.7: Figure 2.7a: picture of the LHC quadrupoles. Figure 2.7b: magnetic fields and resulting focussing force applied on the beam by 2 consecutive quadrupoles.

1063 2.2.2 CMS, a multipurpose experiment

1064 Among the four main LHC experiments is the Compact Muon Solenoid used as a multipurpose tool to
 1065 investigate the SM and physics beyond its scope. Proposed through a letter of intention in 1992 [14],
 1066 and as its name suggests, this very compact detector's uses the muons as a clear tag of most of SM
 1067 and new physics interesting channels. In the original 1997 Technical Design Report (TDR) [21], the
 1068 very first sentences were stating that "*Muons are an unmistakable signature of most of the physics*
 1069 *LHC is designed to explore. The ability to trigger on and reconstruct muons at the highest luminosities is central to the concept of CMS, the Compact Muon Solenoid.*" CMS participated in the
 1070 discovery of the Higgs boson and the measurement of its properties and couplings together with
 1071 ATLAS and is also actively involved in the search for SUSY and heavy ion collisions. Other exotic
 1072 physics are also being investigated using the data collected by CMS.
 1073

1074 The CMS apparatus in itself is the heaviest detector ever built starring a 15m diameter and a
 1075 29 m length for a total weight of 14 kT. A thick 4 T solenoid magnet located at the beam interaction
 1076 point hosts trackers and calorimeters. Extending in all directions around the magnet, heavy iron
 1077 return yokes are installed to extend the magnetic field and support a muon system. The apparatus
 1078 consists of a barrel, referring to the magnet and the detectors contained in it and the part of the
 1079 muon system built directly in the cylinder around the magnet, and of 2 endcaps in the forward and
 1080 backward region of the detector that closes the apparatus and complete the detection coverage along
 1081 the beam line. A front view on the barrel is provided in Figure 2.8 while a detailed view of the
 1082 apparatus is given in Figure 2.9.

1083 In order to efficiently detect all long leaving particles and measure their properties with good
 1084 precision, the CMS detector uses an onion like layout around of the interaction point in order to
 1085 maximize the covered solid angle. As detailed in Figure 2.10, in the innermost region of the detector,
 1086 closest to the interaction point, the silicon tracker records the trajectory of charged particles. Around
 1087 it, the electromagnetic calorimeter (ECAL) stops and measure the energy deposition of electrons
 1088 and photons. In the next layer, the hadron calorimeter (HCAL), hadrons are stopped and their energy
 1089 measured. These layers are contained inside of the magnet of CMS, the superconducting solenoid.
 1090 Outside of the magnet are the muon chambers embedded into iron return yokes used to control the
 1091 magnetic field and gives muons, the only particles traveling completely through the whole detector, a
 1092 double bending helping in reconstructing their energy and trajectory. Note that photons and neutral
 1093 hadrons are differentiated from electrons and charged hadrons in the calorimeters by the fact that

¹⁰⁹⁴ don't interact with the silicon tracker and that they are not influenced by the magnetic field.

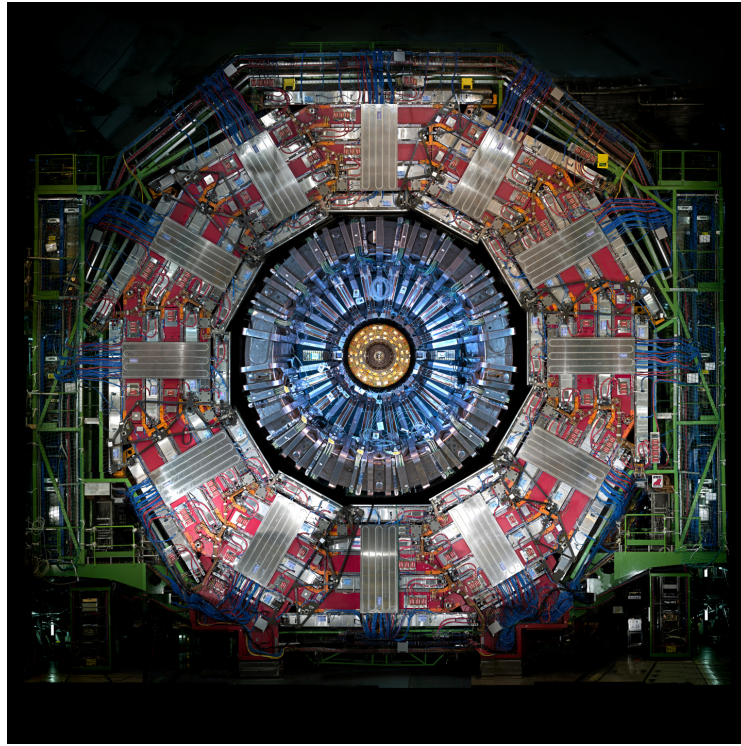


Figure 2.8: Picture of the CMS barrel. The red outer layer is the muon system hosted into the red iron return yokes. The calorimeters are the blue cylinder inside in magnet solenoid and the tracker is the inner yellow cylinder built around the beam pipe.

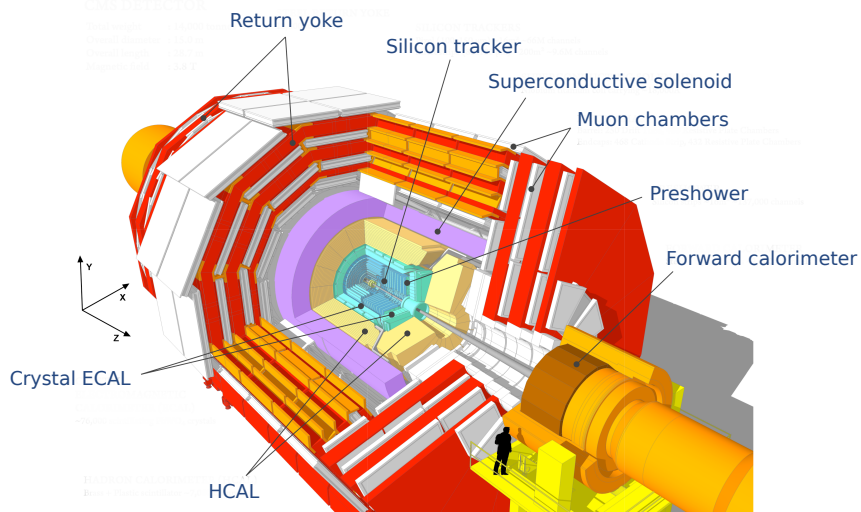


Figure 2.9: View of the CMS apparatus and of its different components.

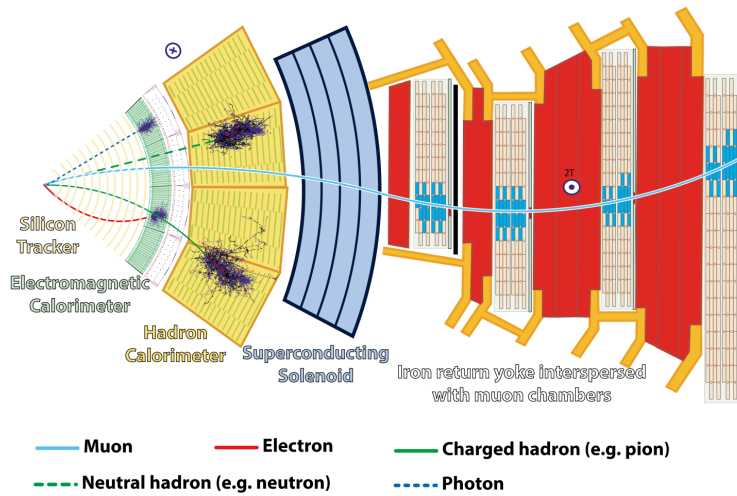


Figure 2.10: Slice showing CMS sub-detectors and how particles interact with them.

1095 The silicon tracker visible on Figure 2.11 is divided into 2 different sub-systems: the *pixel detector* at the very core and the *microstrip detector* around it. This system is composed of 75 million
 1096 individual readout channels with up to 6000 channels per squared centimeter for the pixels making
 1097 it the world's biggest silicon detector. This density allows for measurements of the particle tracks
 1098 with a precision of the order of $10\ \mu\text{m}$. This is necessary to reconstruct all the different interaction
 1099 vertices with precision and have a precise measure of the curvature of the charged particles traveling
 1100 through the magnetic field to estimate their charge and momentum.
 1101

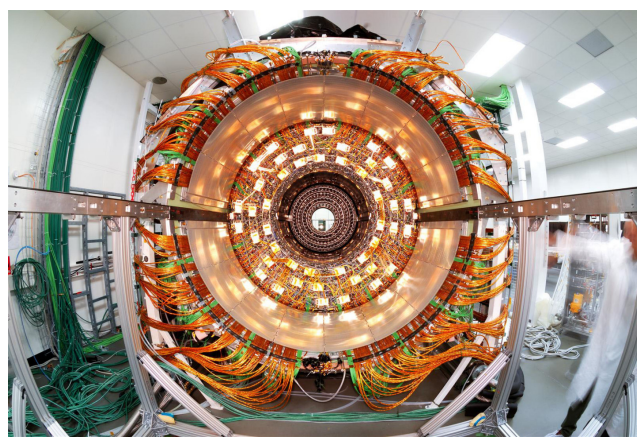


Figure 2.11: CMS tracker.

1102 The ECAL directly surrounding the tracker is composed of crystals of lead tungstate, PbWO_4 , a
 1103 very dense but optically transparent material used to stop high energy electrons and photons. These
 1104 crystal blocks basically are extremely dense scintillators which scintillate in fast, short light bursts
 1105 proportionally to the energy deposition. The light is yielded rapidly and contained at 80% in the
 1106 corresponding 25 ns lasting bunch crossing. Each crystal is isolated from the other by the carbon
 1107 fiber matrix they are embedded in. It is composed of a barrel containing more than 60,000 crystals

and of closing endcaps containing another 15,000 crystals. In front of the ECAL endcap is installed a preshower detector made out of two layers of lead and silicon strip detectors to increase the spatial resolution close to the beam line for pion-photon and single-double photon discrimination purposes. Figure 2.12 shows the calorimeter inside of the magnet and the crystals.

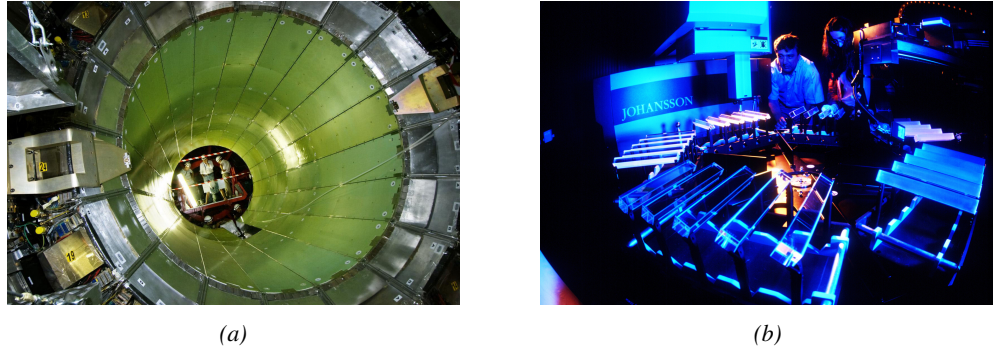


Figure 2.12: Figure 2.12a: picture of the ECAL. Figure 2.12b: picture of the lead tungstate crystals composing the ECAL.

The next layer is the HCAL measuring the hadrons momentum and providing indirect hints of non interacting neutral particles, such as neutrinos, as missing transverse momentum. Several layers of brass or steel are interleaved with plastic scintillators readout by photodiodes using wavelength-shifting fibers. The HCAL is also composed of a barrel, showed in Figure 2.13 and of endcaps. It also features forward calorimeters on both sides of CMS in the region very close to the beam line at high pseudorapidity ($3.0 < |\eta| < 5.0$). The role of these forward calorimeters, made using steel and quartz fibers, is to measure very energetic hadrons.

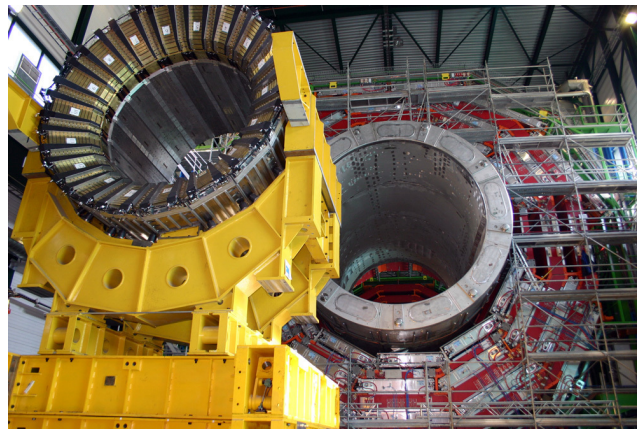


Figure 2.13: CMS hadron calorimeter barrel.

2.2.3 High Luminosity LHC

The very first proton beam successfully circulated in the LHC in September 2008 directly followed by an incident leading to mechanical damage that would delay the LHC program for a year until November 2009, the very first collisions at a center-of-mass energy of 7 TeV taking place in March

1123 2010. The energy of the beam would be increased after a First Long Shutdown (LS1) starting early
 1124 2013 after less than 3 years of data taking. Nevertheless, this first data taking period at only 7 TeV
 1125 was sufficient to claim the discovery of a new particle compatible with the Higgs boson in July 2012.
 1126 During the 2 years of shutdown, the upgrade of the accelerator allowed for several maintainances
 1127 along the beam pipes, repair and consolidation of magnet connection and high-current splices. But
 1128 not only the LHC was upgraded. Indeed, the experiments at the 4 collision points also took the
 1129 advantage of this time to upgrade their system in prevision of the next LHC run (Run-II) until
 1130 2018 and the Second Long Shutdown (LS2) as the luminosity and energy of the beam would be
 1131 continuously increasing. By the end of Run-II, the luminosity will have reached twice its nominal
 1132 value when the center-of-mass energy has already got close to its nominal value by reaching an
 1133 historical 13 TeV for the first time in 2017.

1134 The next long shutdown will occur at the end of this year and will again be the occasion for simi-
 1135 lar maintenance and consolidation in prevision of Run-III and the future upgrade of LS3. Still, the
 1136 main occupation of LS2 on LHC side will be the upgrade of LHC injectors. On the experiments side,
 1137 LHCb and ALICE will, in a very tight schedule, implement major upgrades while ATLAS and CMS
 1138 will wait until LS3 to upgrade their detectors in prevision of high luminosity LHC-Phase-II. ALICE
 1139 main challenge is an upgrade of their apparatus to cope with the 50 kHz $Pb - Pb$ collisions. Simi-
 1140 larly, LHCb will upgrade their frontend readout electronics to cope with the full 40 MHz collisions
 1141 delivered by LHC. ATLAS will perform standard maintenance and CMS will focus on the urgent up-
 1142 grade of the pixel detector and on the installation of new muon detectors in order to take profit of LS2
 1143 time to mitigate the upgrade of detectors foreseen during LS3. Run-III will start in 2021 with the LHC
 1144 at its nominal center-of-mass energy and will bring LHC-Phase-I to an end at the end of 2023. By
 1145 then the luminosity will only increase to reach 2.5 times the nominal luminosity but during these 3
 1146 years of run, the LHC will deliver as much integrated luminosity as what what brought during the al-
 1147 most 7 years of both Run-I and II of data taking. Phase-I will end with an overall 300 fb^{-1} delivered.
 1148



Figure 2.14: Detailed timeline of for LHC and HL-LHC operation until 2028 and operation projection until 2038. This timeline only describes the operation plans after LS1.

After approximately 15 years of operation, the LHC will undergo a new series of upgrade during the LS3 in order to boost its discovery potential. This moment onward is what is referred to HL-LHC or Phase-II as showed in Figure 2.14. The goal is to aim to a luminosity 5 to 7 times stronger than the nominal one trying to reach even 10 times this value if possible. Increasing the luminosity means that the beam size at the collision points needs to be reduced to boost the number of collisions per bunch. For this purpose, new focusing and bending magnets and collimators will be installed at the collision points as well as newly developed "*crab cavities*" that will tilt the particle bunches just prior to the collisions by giving them transverse momentum and thus increasing their meeting area. In addition, the full proton injection line will be upgraded.

Over its full lifetime, the HL-LHC is expected to deliver an outstanding integrated luminosity of 3000 fb^{-1} leading, in the case of Higgs studies, to measuring the couplings of the boson to a precision of 2 to 5% thanks to the estimated 15 millions of Higgs created each year providing a more precise measurement of potential deviations from the theoretical predictions. SUSY studies would also see their limits pushed away and could lead to a new breakthrough. SUSY is a particularly important topic as it could give an answer to why the Higgs boson can stay so light while coupled to heavy particles by introducing the contributions of the super partners on top of providing dark matter candidates. Finally, the increase of luminosity will give the possibility to investigate "exotic" mode like for example the models introducing extra dimensions to explain the hierarchy problem.

On the experiments side, the pile-up (PU) will be increased up to 150 to 200 interactions per bunch crossing in ATLAS and CMS, making necessary an strong upgrade of the trigger system and of the inner trackers and of the calorimeters. Both ATLAS and CMS will also need to upgrade the muon trigger at the level of the endcaps mainly focusing on the coverage near the beam line in order to increase the detection acceptance and event selection. Moreover, the increased luminosity will also lead to an increased background rate and a faster ageing of the detectors. This PhD work takes place into this very specific context of muon detector consolidation and certification for the HL-LHC period in order to provide the CMS experiment with robust detectors that will live through the next 20 years of HL-LHC.

2.3 Muon Phase-II Upgrade

After the more than two years lasting LS1, the LHC delivered its very first Run-II proton-proton collisions early 2015. LS1 gave the opportunity to the LHC and to the its experiments to undergo upgrades. The accelerator is now providing collisions at center-of-mass energy of 13 TeV and bunch crossing rate of 40 MHz, with a peak luminosity exceeding its design value. During the first and upcoming second LHC Long Shutdown, the CMS detector is also undergoing a number of upgrades to maintain a high system performance [21].

From the LHC Phase-2 or HL-LHC period onwards, i.e. past LS3, the performance degradation due to integrated radiation as well as the average number of inelastic collisions per bunch crossing, or pileup, will rise substantially and become a major challenge for the LHC experiments, like CMS that are forced to address an upgrade program for Phase-II [22]. Simulations of the expected distribution of absorbed dose in the CMS detector under HL-LHC conditions, show in figure 4.16 that detectors placed close to the beamline will have to withstand high irradiation, the radiation dose being of the order of a few tens of Gy.

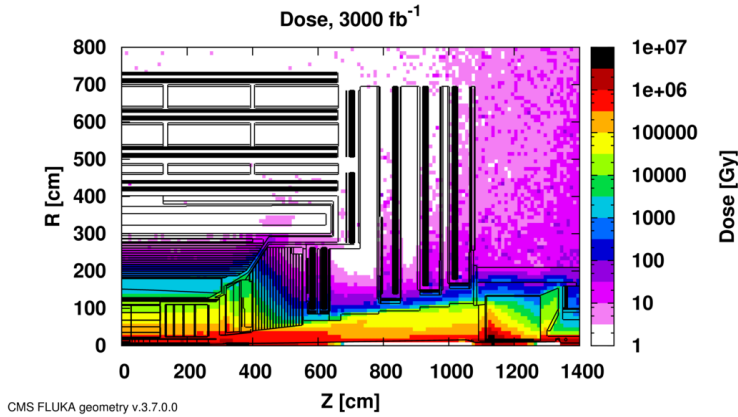


Figure 2.15: Absorbed dose in the CMS cavern after an integrated luminosity of 3000 fb^{-1} . R is the transverse distance from the beamline and Z is the distance along the beamline from the Interaction Point at $Z=0$.

The measurement of small production cross-section and/or decay branching ratio processes, such as the Higgs boson coupling to charge leptons or the $B_s \rightarrow \mu^+ \mu^-$ decay, is of major interest and specific upgrades in the forward regions of the detector will be required to maximize the physics acceptance on the largest possible solid angle. To ensure proper trigger performance within the present coverage, the muon system will be completed with new chambers. In figure 2.16 one can see that the existing Cathode Strip Chambers (CSCs) will be completed by Gas Electron Multipliers (GEMs) and Resistive Plate Chambers (RPCs) in the pseudo-rapidity region $1.6 < |\eta| < 2.4$ to complete its redundancy as originally scheduled in the CMS Technical Proposal [23].

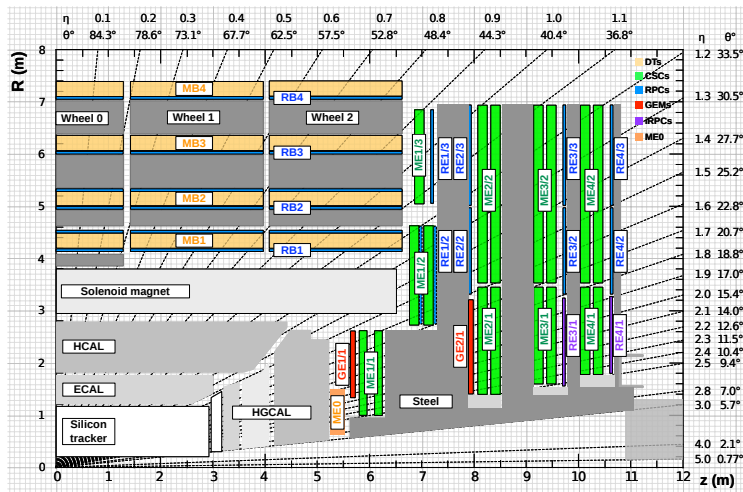


Figure 2.16: A quadrant of the muon system, showing DTs (yellow), RPCs (light blue), and CSCs (green). The locations of new forward muon detectors for Phase-II are contained within the dashed box and indicated in red for GEM stations (ME0, GE1/1, and GE2/1) and dark blue for improved RPC (iRPC) stations (RE3/1 and RE4/1).

RPCs are used by the CMS first level trigger for their good timing performances. Indeed, a very good bunch crossing identification can be obtained with the present CMS RPC system, given their

fast response of the order of 1 ns. In order to contribute to the precision of muon momentum measurements, muon chambers should have a spatial resolution less or comparable to the contribution of multiple scattering [21]. Most of the plausible physics is covered only considering muons with $p_T < 100$ GeV thus, in order to match CMS requirements, a spatial resolution of $\mathcal{O}(\text{few mm})$ the proposed new RPC stations, as shown by the simulation in figure 2.17. According to preliminary designs, RE3/1 and RE4/1 readout pitch will be comprised between 3 and 6 mm and 5 η -partitions could be considered.

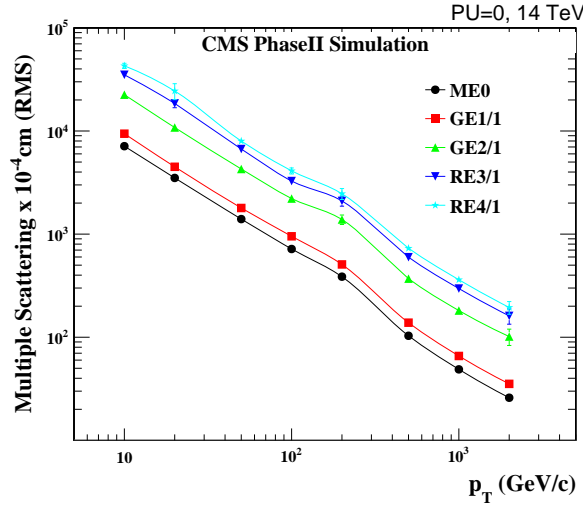


Figure 2.17: RMS of the multiple scattering displacement as a function of muon p_T for the proposed forward muon stations. All of the electromagnetic processes such as bremsstrahlung and magnetic field effect are included in the simulation.

3

1207

1208

Physics of Resistive plate chambers

1209 A Resistive Plate Chamber (RPC) is a gaseous detector using the same physical processes described
1210 in Chapter 3. It has been developed in 1981 by Santonico and Cardarelli [24], under the name of
1211 *Resistive Plate Counter*, as an alternative to the local-discharge spark counters proposed in 1978
1212 by Pestov and Fedotovich [25, 26]. Working with spark chambers implied using high-pressure gas
1213 and high mechanical precision which the RPC simplified by formerly using a gas mixture of argon
1214 and butane flowed at atmospheric pressure and a constant and uniform electric field propagated
1215 in between two parallel electrode plates. Moreover, a significant increase in rate capability was
1216 introduced by the use of electrode plate material with high bulk resistivity, preventing the discharge
1217 from growing throughout the whole gas gap. Indeed, the effect of using resistive electrodes is that
1218 the constant electric field is locally canceled out by the development of the discharge, limiting its
1219 growth.

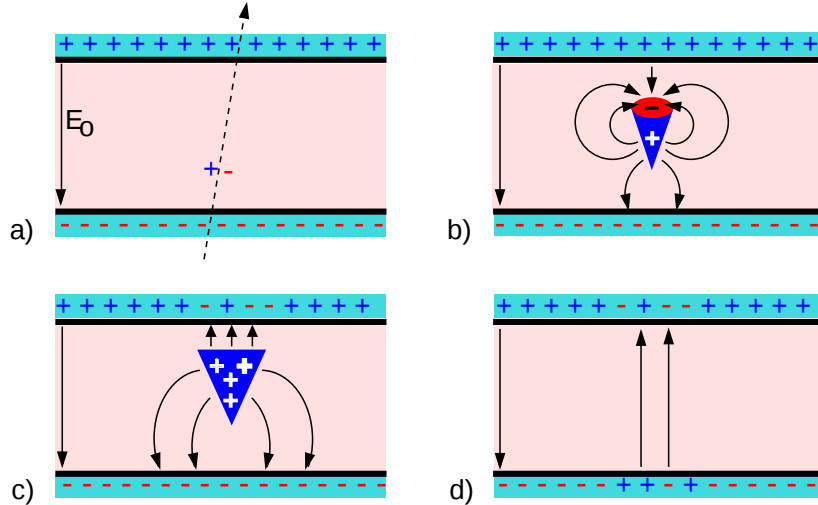
1220 Through its development history, different operating modes [27–29] and new detector designs [30–
1221 32] have been discovered, leading to further improvement of the rate capability of such a detector.
1222 Moreover, the addition of SF_6 into the gas mix improved the stability of operation of the RPC [33,
1223 34].

1224 The low developing costs and easily achievable large detection areas offered by RPCs, as well as
1225 the wide range of possible designs, made them a natural choice to as muon chambers and/or trigger
1226 detectors in multipurpose experiments such as CMS [21] or ATLAS [35], time-of-flight detectors in
1227 ALICE [36], calorimeter with CALICE [37] or even detectors for volcanic muography with ToMu-
1228 Vol [38].

1229 3.1 Principle

1230 RPCs are ionisation detectors composed of two parallel resistive plate electrodes in between which
1231 a constant electric field is set. The space in between the electrodes, referred as *gap*, is filled with a
1232 dense gas that is used to generate primary ionization into the gas volume. The free charge carriers
1233 (electrons and cations) created by the ionization of the gas molecules are then accelerated towards

1234 the electrodes by the electric field, as shown in Figure 3.1 [39].



1235 *Figure 3.1: Different phases of the avalanche development in the RPC gas volume subjected to a constant*
 1236 *electric field E_0 . a) An avalanche is initiated by the primary ionisation caused by the passage of a charged*
 1237 *particle through the gas volume. b) Due to its growing size, the avalanche starts to locally influence the electric*
 1238 *field. c) The electrons, lighter than the cations reach the anode first. d) The ions reach the cathode. While*
 1239 *the charges have not recombined, the electric field in the small region around the avalanche stays affected and*
 1240 *locally blind the detector.*

1241 RPCs being passive detectors, a current on pick-up copper read-out placed outside of the gas
 1242 volume is induced by the charge accumulation during the growth of the avalanche. As a result,
 1243 the time resolution of the detector is substantially increased as the output signal is generated while
 1244 the electrons are still in movement. The advantage of a constant electric field, over multi-wire
 1245 proportional chambers, is that the electrons are being fully accelerated from the moment charge
 1246 carriers are freed and feel the full strength of the electric field that doesn't depend on the distance to
 1247 the readout and that the output signal doesn't need for the electrons to be physically collected.

1242 The typical gas mixture RPCs are operated with is generally composed of 3 gas compounds.

- 1243 • Tetrafluoroethane ($C_2F_4H_2$), also referred to as *Freon*, is the principal compound of the RPC
 1244 gas mixtures, with a typical fraction above 90%. It is used for it's high effective Townsend
 1245 coefficient and the great average fast charge that allows to operate the detector with a high
 1246 threshold with respect to argon, for example, that has similar effective Townsend coefficient
 1247 but suffers from a lower fast charge. To operate with similar conditions, argon would require a
 1248 higher electric field leading to a higher fraction of streamers, thus limiting the rate capability
 1249 of the detector [40].
- 1250 • Isobutane (i- C_4H_{10}), only present in a few percent in the gas mixtures, is used for its UV
 1251 quenching properties [41] helping to prevent streamers due to UV photon emission during the
 1252 avalanche growth.
- 1253 • Sulfur hexafluoride, (SF_6), referred to simply as *SF6*, is used in very little quantities for its
 1254 high electronegativity. Excess of electrons are being absorbed by the compound and streamers

are suppressed [34]. Nevertheless, a fraction of SF_6 higher than 1% will not bring any extra benefit in terms of streamer cancelation power but will lead to higher operating voltage [33], as can be understood through Figure 3.2.

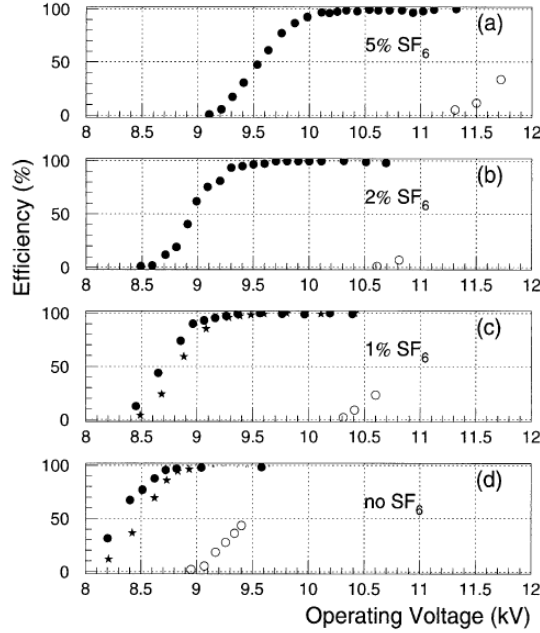


Figure 3.2: Effeciency (circles and stars with 30 mV and 100 mV thresholds respectively) and streamer probability (opened circles) as function of the operating voltatge of a 2 mm single gap HPL RPC flushed with a gas mixture containing (a) 5%, (b) 2%, (c) 1% and (d) no SF_6 [33].

After an avalanche developed in the gas, a time long compared to the development of a discharge is needed to recombine the charge carriers in the electrode material due to their resistivity. This property has the advantage of affecting the local electric field and avoiding sparks in the detector but, on the other hand, the rate capability is intrinsically limited by the time constant τ_{RPC} of the detector. Using a quasi-static approximation of Maxwell's equations for weakly conducting media, it can be shown that the time constant τ_{RPC} necessary to the charge recombination at the interface in between the electrode and the gas volume is given by the Formula 3.1 [42].

$$\tau_{RPC} = \frac{\epsilon_{electrode} + \epsilon_{gas}}{\sigma_{electrode} + \sigma_{gas}} \quad (3.1)$$

A gas can be assimilated to vacuum, leading to $\epsilon_{gas} = \epsilon_0$ and $\sigma_{gas} = 0$, and the electrodes permittivity and conductivity can be written as $\epsilon_{electrode} = \epsilon_r \epsilon_0$ and $\sigma_{electrode} = 1/\rho_{electrode}$, showing the strong dependence of the time constant to the electrodes resistivity in Formula 3.2.

$$\tau_{RPC} = (\epsilon_r + 1)\epsilon_0 \times \rho_{electrode} \quad (3.2)$$

Very few materials with a low enough resistivity exist in nature. The resistivity targeted to build RPCs ranges from 10^9 to $10^{12} \Omega \cdot \text{cm}$. The most common RPC electrode materials are displayed in Table 3.1. When the doped glass and ceramics can offer short time constants of the order of 1 ms,

1271 the developing cost of such materials is quite high due to the very low demand. Thus, High-pressure
 1272 laminate (HPL) is often the choice for high rate experiments using very large RPC detection areas.
 1273 Other experiments working at cosmic muon fluxes can safely operate with ordinary float glass.

Material	$\rho_{electrode}$ ($\Omega \cdot \text{cm}$)	ϵ_r	τ_{RPC} (ms)
Float glass	10^{12}	~ 7	~ 700
High-pressure laminate	10^{10} to 10^{12}	~ 6	~ 6 to 600
Doped glass (LR S)	10^9 to 10^{11}	~ 10	~ 1 to 100
Doped ceramics (SiN/SiC)	10^9	~ 8.5	~ 1
Doped ceramics (Ferrite)	10^8 to 10^{12}	~ 20	~ 0.2 to 2000

Table 3.1: Properties of the most used electrode materials for RPCs.

1274 3.1.1 Electron drift velocity

1275 Talk about the electron drift velocity and mention the time resolution of RPCs.

1276 3.2 Rate capability and time resolution of Resistive Plate Cham- 1277 bers

1278 As already previously discussed, the electrode material plays a key role in the max intrinsic rate
 1279 capability of RPCs. R&D is being done to develop at always cheaper costs material with lower
 1280 resistivity. Nevertheless, the amount of charge released, i.e. the size of the discharge, if reduced
 1281 leads to a smaller blind area in the detector, increasing the rate capability of the detector.

1282 3.2.1 Operation modes

1283 RPCs where developed early 1980s. At that time it was using an operating mode now referred to
 1284 as *streamer mode*. Streamers are large discharges that develop in between the 2 electrodes enough
 1285 to locally discharge the electrodes. If the electric field inside of the gas volume is strong enough,
 1286 with electrons being fast compared to ions, a large and dense cloud of positive ions will develop
 1287 nearby the anode and extend toward the cathode while the electrons are being collected, eventually
 1288 leading to a streamer discharge due to the increase of field seen at the cathode. the field is then strong
 1289 enough so that electrons are pulled out of the cathode. Electrodes, though they are a unique volume
 1290 of resistive material, can be assimilated to capacitors. At the moment an electric field is applied in
 1291 between their outer surfaces, the charge carriers inside of the volume will start moving leading to
 1292 a situation where there is no voltage across the electrodes and a higher density of negative charges,
 1293 i.e. electrons, on the inner surface of the cathode. Finally, when a streamer discharge occurs, these
 1294 electrons are partially released in the gas volume contributing to increase the discharge strength until
 1295 the formation of a conductive plasma, the streamer. This can be understood through Figure 3.3 [27].
 1296 Streamer signals are very convenient in terms of read-out as no amplification is required with output
 1297 pulses amplitudes of the order of a few tens to few hundreds of mV as can be seen on Figure 3.4.

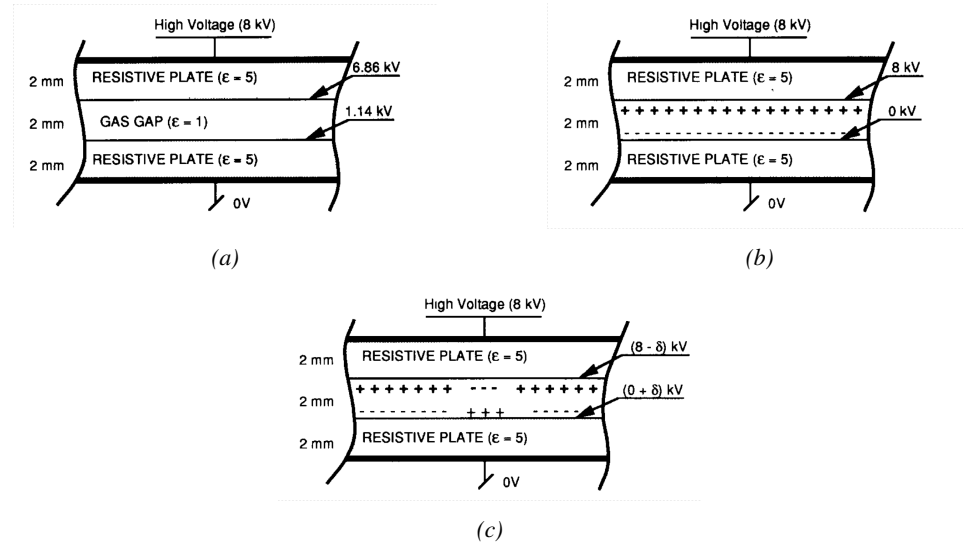


Figure 3.3: Movement of the charge carriers in an RPC. Figure 3.3a: Voltage across an RPC whose electrode have a relative permittivity of 5 at the moment the tension is applied. Figure 3.3b: After the charge carriers moved, the electrodes are charged and there is no voltage drop over the electrodes anymore. The full potential is applied on the gas gap only. Figure 3.3c: The streamer discharge initiated by a charged particle transports electrons and cations towards the anode and cathode respectively.

When the electric field is reduced though, the electronic gain is small until the electrons get close enough to the anode and the positive ion cloud is much smaller. The electric field cannot rise to the point a field emission of electrons on the cathode is possible. The resulting signal is weak, of the order of a few mv as shown on Figure 3.4, and requires amplification. This is the *avalanche mode* of RPC operation.

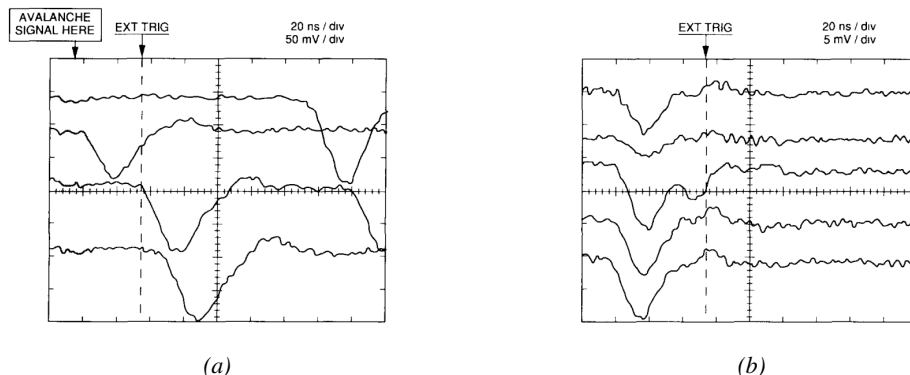


Figure 3.4: Typical oscilloscope pulses in streamer mode (Figure 3.4a) and avalanche mode (Figure 3.4b). In the case of streamer mode, the very small avalanche signal is visible.

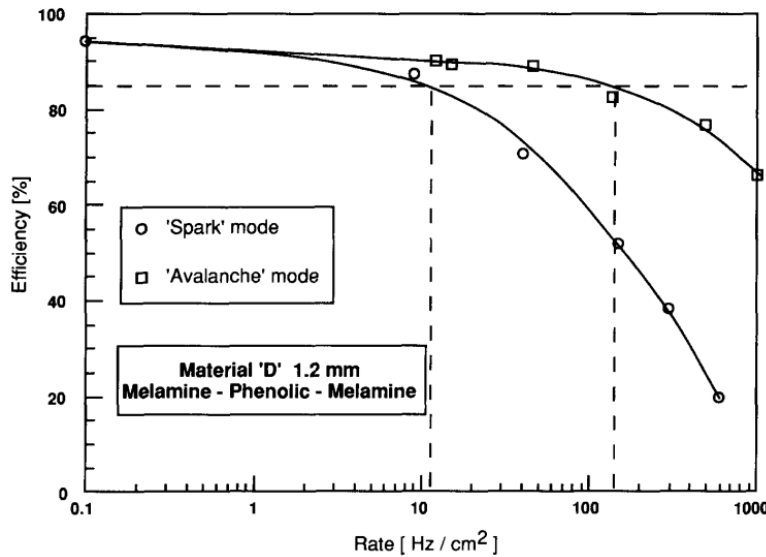


Figure 3.5: Rate capability comparison for the streamer and avalanche mode of operation. An order of magnitude in rate capability for a maximal efficiency drop of 10% is gained by using the avalanche mode over the streamer mode.

This mode offers a higher rate capability by providing smaller discharges that don't affect the electrodes charge and are more locally contained in the gas volume as was demonstrated by Crotty with Figure 3.5 [27]. The detector only stays locally blind the time the charge carriers are recombined and there is no need for electrode recharge which is a long process affecting a large portion of the detector. Another advantage of avalanche signals over streamer is the great time consistency. Figure 3.4 shows very clearly that avalanche signals have a very small time jitter. This is a natural choice for high rate experiments.

3.2.2 Detector designs and performance

Different RPC design have been used and each of them present its own advantages. Historically, the first type of RPC to have been developed is what is referred now to *narrow gap* RPC [24, 43]. After the avalanche mode has been discovered [27], it has been proven that increasing the width of the gas gap lead to higher rate capability, due to lower charge deposition per avalanche, and lower power dissipation [43]. Nevertheless, by increasing the gas gap width, the time resolution of the detector decreases. This is a natural result if the increase of active gas volume in the detector is taken into account. Indeed, for a given threshold, only the small fraction of gas closest to the cathode will provide enough gain to have a detectable signal. In the case of a wider gas volume, the active region is then larger and a larger time jitter is introduced with the variation of starting position of the avalanche, as discussed in [30]. To solve improve both the time resolution and the rate capability, different methods were used trying to get advantages of both narrow and wide gap RPCs.

1322 **3.2.2.1 Double-gap RPC**

1323 Double-gap RPCs are made out of 2 narrow RPC detectors. The 2 RPC gaps are stacked on top of
 1324 each other as shown in Figure 3.6. This detector layout, popularized by the two multipurpose experiments
 1325 CMS [21] and ATLAS [35] at LHC, can be used as an OR system in which each individual
 1326 chamber participates in the output signal. The gain of such a detector is greatly reduced with respect
 1327 to single-gap RPCs with an efficiency plateau reached at lower voltage, as visible on Figure 3.7.

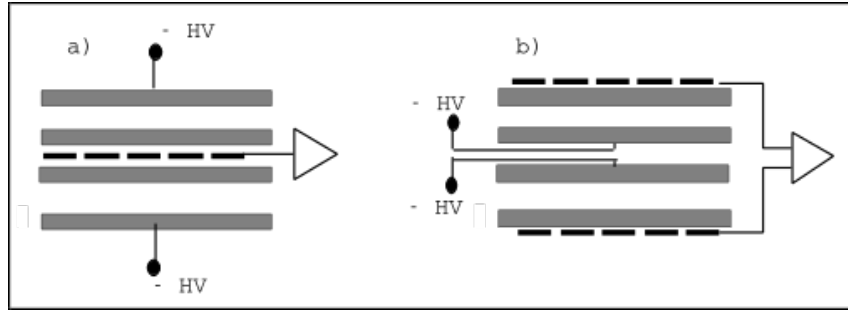


Figure 3.6: Possible double-gap RPC layouts: a) "standard" 1D double-gap RPC, as used in CMS experiment, where the anodes are facing each other and a 1D read-out plane is sandwiched in between them, b) double read-out double-gap RPC as used in ATLAS experiment, where the cathodes are facing each other and 2 read-out planes are used on the outer surfaces. This last layout can offer the possibility to use a 2D reconstruction by using orthogonal read-out planes.

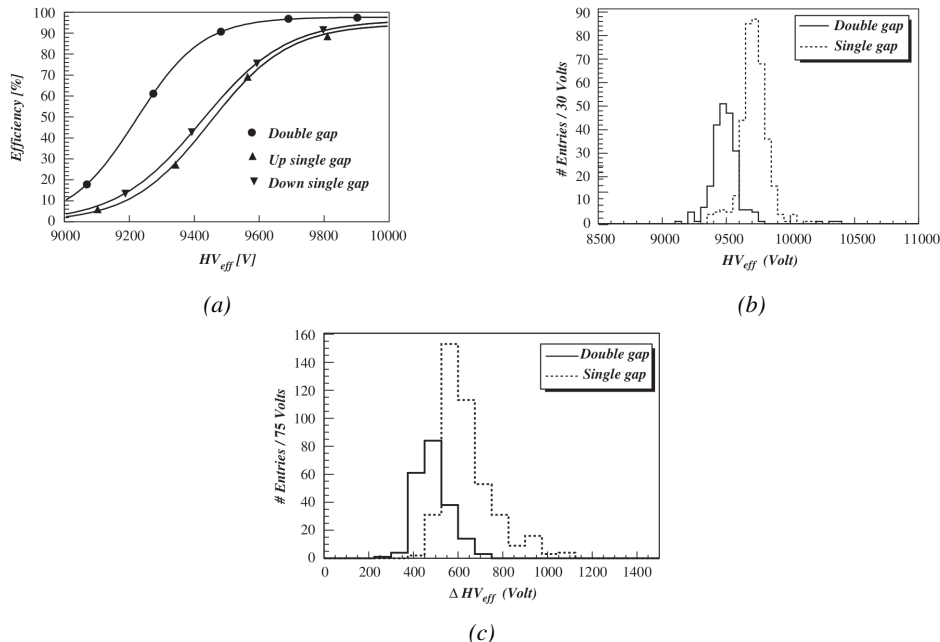


Figure 3.7: Comparison of performance of CMS double and single gap RPCs using cosmic muons [44]. Figure 3.7a: Comparison of efficiency sigmoids. Figure 3.7b: Voltage distribution at 95% of maximum efficiency. Figure 3.7c: $\Delta_{10\%}^{90\%}$ distribution.

3.2.2.2 Multigap RPC (MRPC)

MRPCs are layouts in which floating sub electrode plates are placed into a wide gap RPC to divide the gas volume and create a sum of narrow gaps [30, 31]. The time resolution of such a detector can reach of few tens of ps, with gas gaps of the order of a few hundred μm as shown in Figure 3.8 representing ALICE Time-of-flight (ToF) MRPCs.

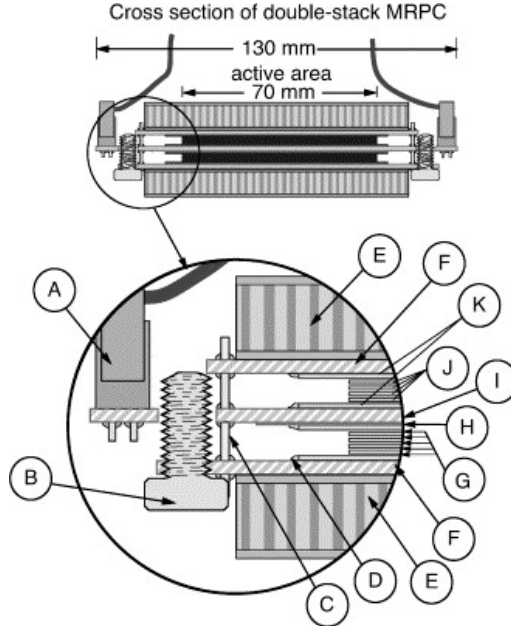


Figure 3.8: Presentation of ALICE MRPC using $250 \mu\text{m}$ gas gaps, $620 \mu\text{m}$ outer glass electrodes and $550 \mu\text{m}$ inner floating electrodes. More details on the labels are given in [45].

Sometimes used as a double multigap RPC, taking advantage of the OR of double gap RPCs, the MRPC is mainly used as ToF detector [45–49] due to its excellent timing properties that allow to perform particle identification as explained by Williams in [50]. The principle of particle identification using ToF is simply the measurement of the velocity of a particle. Indeed, particles are defined by their mass (for the parameter of interest here, their electric charge being measured using the bending angle of the particles traveling through a magnetic field) and this mass can be calculated by measuring the velocity β and momentum of the particle:

$$\beta = \frac{p}{\sqrt{p^2 + m^2}} \quad (3.3)$$

Intuitively, it is trivial to understand that 2 different particles having the same momentum will have a different velocity due to the mass difference and thus a different flight time T_1 and T_2 through the detector and this is used to separate and identify particles. The better the time resolution of the ToF system used, the stronger will the separation be:

$$T = \frac{L}{v} = \frac{L}{c \cdot \beta}, \quad \Delta T = T_1 - T_2 = \frac{L}{c} \left(\sqrt{1 + m_1^2/p^2} - \sqrt{1 + m_2^2/p^2} \right) \cong (m_1^2 - m_2^2) \frac{L}{2cp^2} \quad (3.4)$$

1344 An example of particle identification is given for the case of STAR experiment in Figure 3.9.

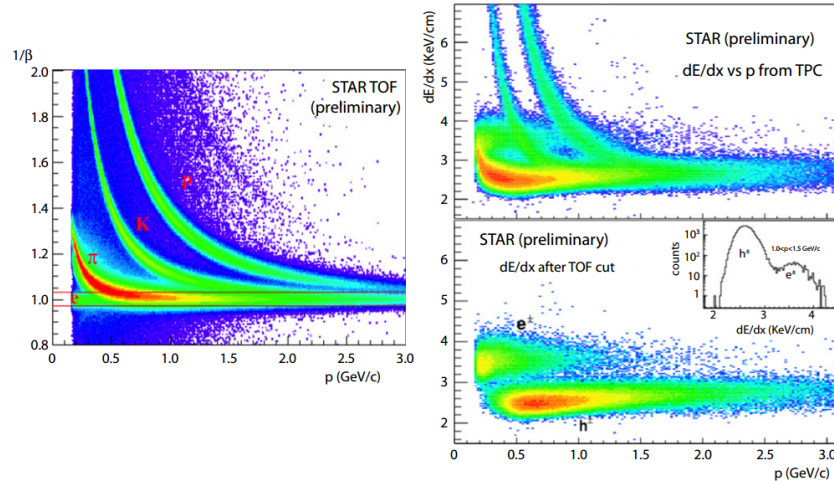


Figure 3.9: Particle identification applied to electrons in the STAR experiment. The identification is performed combining ToF and dE/dx measurements [50].

1345 Another benefice of using such small gas gaps is the strong reduction of the average avalanche
1346 volume and thus of the blind spot on MRPCs leading to an improved rate capability. Multigaps can
1347 sustain backgrounds of several kHz/cm² as demonstrated in Figure 3.10.

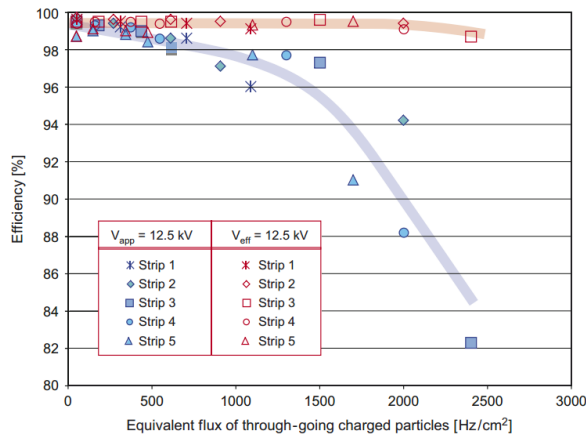


Figure 3.10: Comparison of the detector performance of ALICE ToF MRPC [51] at fixed applied voltage (in blue) and at fixed effective voltage (in red). The effective voltage is kept fixed by increasing the applied voltage accordingly to the current drawn by the detector.

1348 3.2.2.3 Charge distribution and performance limitations

1349 The direct consequence of the different RPC layouts is a variation of intrinsic time resolution of the
1350 RPC as the gap size decreases. An advantage is given to multigaps whose design use sub-millimeter
1351 gas volumes providing very consistent signals.

1352 On the charge spectrum point of view, each layout has its own advantages. When the double-gap
 1353 has the highest induced over drifting charge ratio, as seen in Figure 3.11, the multigap has a charge
 1354 spectrum strongly detached from the origin, as visible in Figure 3.12. A high induced over drifting
 1355 charge ratio means that the double gap can be safely operated at high threshold or that at similar
 1356 threshold it can be operated with a twice smaller drifting charge, meaning a higher rate capability.
 1357 On the other hand, the strong detachment of the charge spectrum from the origin in the MRPC case
 1358 allows to reach a higher efficiency with increasing threshold as most of the induced charge is not low
 1359 due to the convolution of several single gap spectra. The range of stable efficiency increases with
 1360 the number of gap, as presented in Figure 3.13.

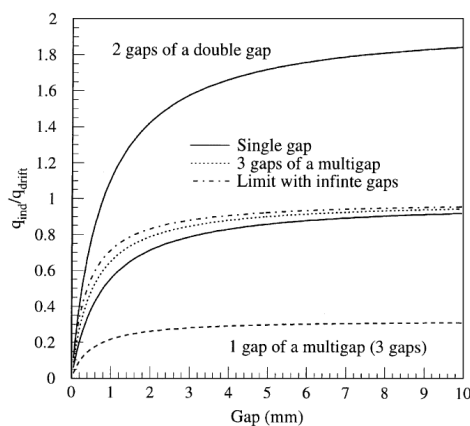


Figure 3.11: Ratio between total induced and drifting charge have been simulated for single gap, double-gap and multigap layouts [52]. The total induced charge for a double-gap RPC is a factor 2 higher than for a multigap.

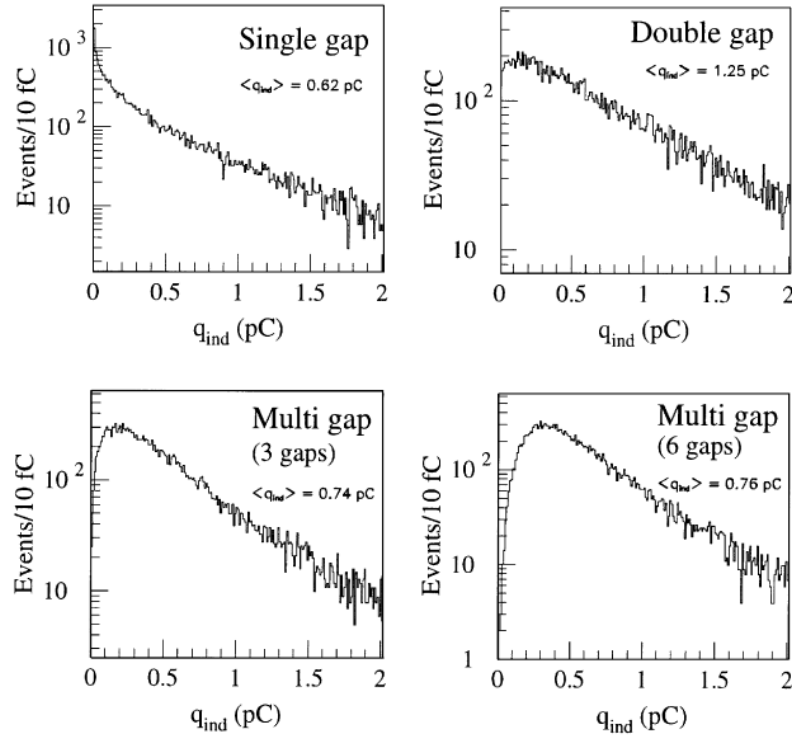


Figure 3.12: Charge spectra have been simulated for single gap, double-gap and multigap layouts [52]. It appears that when single gap shows a decreasing spectrum, double and multigap layouts exhibit a spectrum whose peak is detached from the origin. The detachment gets stronger as the number of gaps increases.

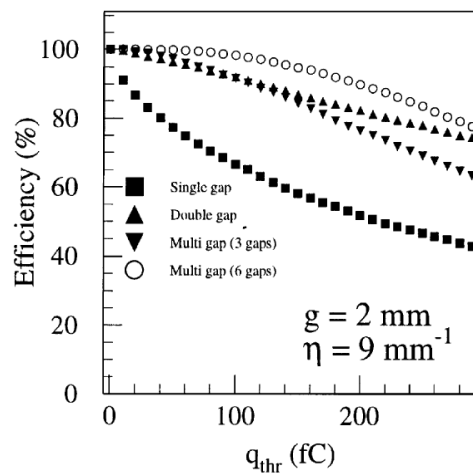


Figure 3.13: The maximal theoretical efficiency is simulated for single gap, double-gap and multigap layouts [52] at a constant gap thickness of 2 mm and using an effective Townsend coefficient of 9 mm^{-1} .

- ¹³⁶¹ **3.3 Signal formation**
- ¹³⁶² **3.4 Gas transport parameters**

4

1363

1364

1365

Longevity studies and Consolidation of the present CMS RPC subsystem

4.1 Resistive Plate Chambers at CMS

4.1.1 Overview

1368 The Resistive Plate Chambers (RPC) system, located in both barrel and endcap regions, provides a
1369 fast, independent muon trigger with a looser p_T threshold over a large portion of the pseudorapidity
1370 range ($|\eta| < 1.6$) [add reconstruction].

1371

1372 During High-Luminosity LHC (HL-LHC) operations the expected conditions in terms of back-
1373 ground and pile-up will make the identification and correct P_T assignment a challenge for the Muon
1374 system. The goal of RPC upgrade is to provide additional hits to the Muon system with precise tim-
1375 ing. All these informations will be elaborated by the trigger system in a global way enhancing the
1376 performance of the trigger in terms of efficiency and rate control. The RPC Upgrade is based on two
1377 projects: an improved Link Board System and the extension of the RPC coverage up to $|\eta| = 2.4$.
1378 [FIXME 2.4 or 2.5?]

1379 The Link Board system, that will be described in section xxx, is responsible to process, syn-
1380 chronize and zero-suppress the signals coming from the RPC front end boards. The Link Board
1381 components have been produced between 2006 and 2007 and will be subjected to aging and failure
1382 in the long term. The upgraded Link Board system will overcome the aging problems described in
1383 section xxx and will allow for a more precise timing information to the RPC hits from 25 to 1 ns [ref
1384 section xxx].

1385 The extension of the RPC system up to $|\eta| = 2.1$ was already planned in the CMS TDR [ref
1386 cmstdr] and staged because of budget limitations and expected background rates higher than the rate
1387 capability of the present CMS RPCs in that region. An extensive R&D program has been done in
1388 order to develop an improved RPC that fulfills the CMS requirements. Two new RPC layers in the
1389 innermost ring of stations 3 and 4 will be added with benefits to the neutron-induced background

1390 reduction and efficiency improvement for both trigger and offline reconstruction.

1391 4.1.2 The present RPC system

1392 The RPC system is organized in 4 stations called RB1 to RB4 in the barrel region, and RE1 to RE4
 1393 in the endcap region. The innermost barrel stations, RB1 and RB2, are instrumented with 2 layers
 1394 of RPCs facing the innermost (RB1in and RB2in) and outermost (RB1out and RB2out) sides of the
 1395 DT chambers. Every chamber is then divided from the read-out point of view into 2 or 3 η partitions
 1396 called “rolls”. The RPC system consist of 480 barrel chambers and 576 endcap chambers. Details
 1397 on the geometry are discussed in the paper [ref to geo paper].

1398 The CMS RPC chamber is a double-gap, operated in avalanche mode to ensure reliable operation
 1399 at high rates. Each RPC gap consists of two 2-mm-thick resistive High-Pressure Laminate (HPL)
 1400 plates separated by a 2-mm-thick gas gap. The outer surface of the HPL plates is coated with a thin
 1401 conductive graphite layer, and a voltage is applied. The RPCs are operated with a 3-component,
 1402 non-flammable gas mixture consisting of 95.2% freon ($C_2H_2F_4$, known as R134a), 4.5% isobutane
 1403 ($i-C_4H_{10}$), and 0.3% sulphur hexafluoride (SF_6) with a relative humidity of 40% - 50%. Readout
 1404 strips are aligned in η between the 2 gas gaps. [\[Add a sentence on FEBs.\]](#)

1405 The discriminated signals coming from the Front End boards feed via twisted cables (10 to 20 m
 1406 long) the Link Board System located in UXC on the balconies around the detector. The Link System
 1407 consist of the 1376 Link Boards (LBs) and the 216 Control Boards (CBs), placed in 108 Link Boxes.
 1408 The Link Box is a custom crate (6U high) with 20 slots (for two CBs and eighteen LBs). The Link
 1409 Box contains custom backplane to which the cables from the chambers are connected, as well as the
 1410 cables providing the LBs and CBs power supply and the cables for the RPC FEBs control with use
 1411 of the I2C protocol (trough the CB). The backplane itself contains only connectors (and no any other
 1412 electronic devices).

1413 The Link Board has 96 input channels (one channel corresponds to one RPC strip). The input
 1414 signals are the ~ 100 ns binary pulses which are synchronous to the RPC hits, but not to the LHC
 1415 clock (which drives the entire CMS electronics). Thus the first step of the FEB signals processing
 1416 is synchronization, i.e. assignment of the signals to the BXes (25 ns periods). Then the data are
 1417 compressed with a simple zero-suppressing algorithm (the input channels are grouped into 8 bit
 1418 partitions, only the partitions with at least one nonzero bit are selected for each BX). Next, the non-
 1419 empty partitions are time-multiplexed i.e. if there are more than one such partition in a given BX,
 1420 they are sent one-by-one in consecutive BXes. The data from 3 neighbouring LBs are concentrated
 1421 by the middle LB which contains the optical transmitter for sending them to the USC over a fiber at
 1422 1.6 Gbps.

1423 The Control Boards provide the communication of the control software with the LBs via the
 1424 FEC/CCU system. The CBs are connected into token rings, each ring consists of 12 CBs of one
 1425 detector tower and a FEC mezzanine board placed on the CCS board located in the VME crate in
 1426 the USC. In total, there are 18 rings in the entire Link System. The CBs also perform automatic
 1427 reloading of the LB's firmware which is needed in order to avoid accumulation of the radiation
 1428 induced SEUs in the LBs firmware.

1429 Both LBs and CB are based on the Xilinx Spartan III FPGAs, the CB additionally contains
 1430 radiation-tolerant (FLASH based) FPGA Actel ProAsicPlus.

1431 The High Voltage power system is located in USC, not exposed to radiation and easily accessible
 1432 for any reparation. A single HV channel powers 2 RPC chambers both in the barrel and endcap
 1433 regions. The Low Voltage boards are located in UXC on the balconies and provide the voltage to the

¹⁴³⁴ front end electronics.

¹⁴³⁵ 4.1.3 Pulse processing of CMS RPCs

¹⁴³⁶ Signals induced by cosmic particle in the RPC strips are shaped by standard CMS RPC Front-End
¹⁴³⁷ Electronics (FEE) following the scheme of Figure 4.1. On a first stage, analogic signals are amplified
¹⁴³⁸ and then sent to the Constant Fraction Discriminator (CFD) described in Figure 4.2. At the end of
¹⁴³⁹ the chain, 100 ns long pulses are sent in the LVDS output. These output signal are sent on one side to
¹⁴⁴⁰ a V1190A Time-to-Digital Converter (TDC) module from CAEN and on the other to an OR module
¹⁴⁴¹ to count the number of detected signals. Trigger and hit coïncidences are monitored using scalers.
¹⁴⁴² The TDC is used to store the data into ROOT files. These files are thus analysed to understand the
¹⁴⁴³ detectors performance.

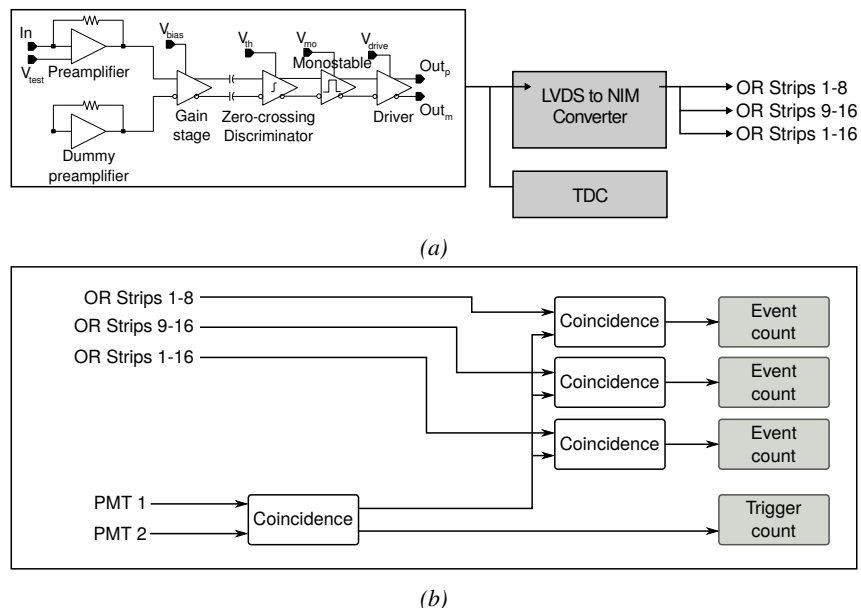


Figure 4.1: Signals from the RPC strips are shaped by the FEE described on Figure 4.1a. Output LVDS signals are then read-out by a TDC module connected to a computer or converted into NIM and sent to scalers. Figure 4.1b describes how these converted signals are put in coincidence with the trigger.

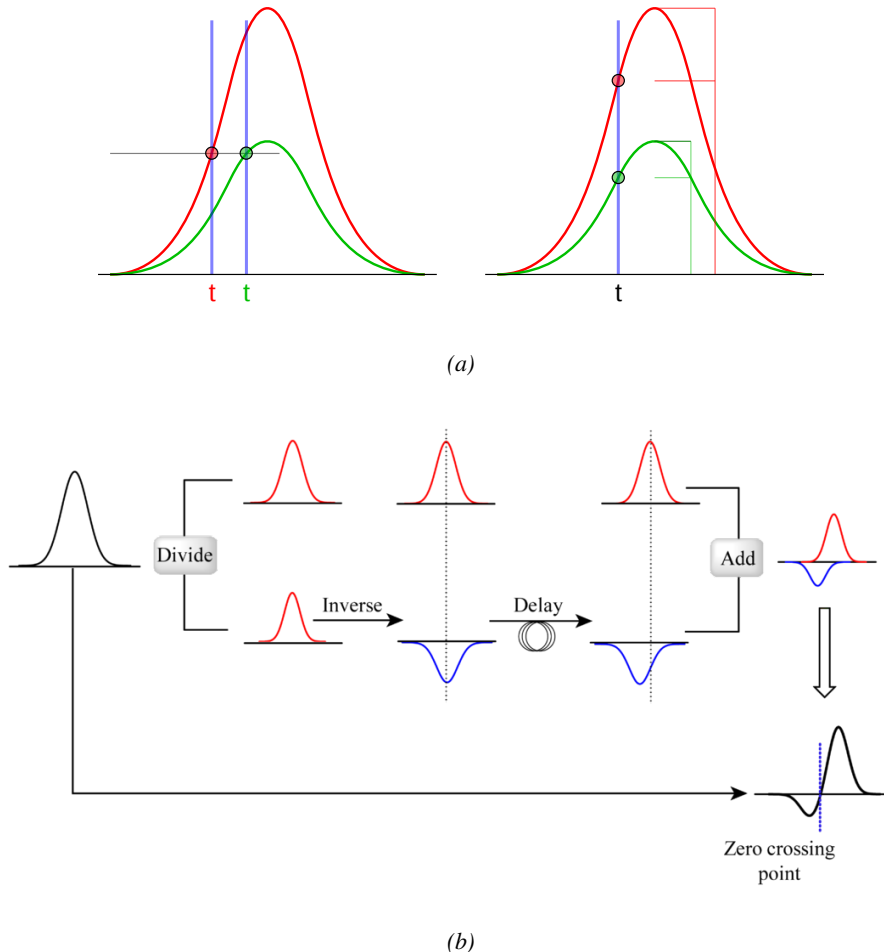


Figure 4.2: Description of the principle of a CFD. A comparison of threshold triggering (left) and constant fraction triggering (right) is shown in Figure 4.2a. Constant fraction triggering is obtained thanks to zero-crossing technique as explained in Figure 4.2b. The signal arriving at the input of the CFD is split into three components. A first one is delayed and connected to the inverting input of a first comparator. A second component is connected to the noninverting input of this first comparator. A third component is connected to the noninverting input of another comparator along with a threshold value connected to the inverting input. Finally, the output of both comparators is fed through an AND gate.

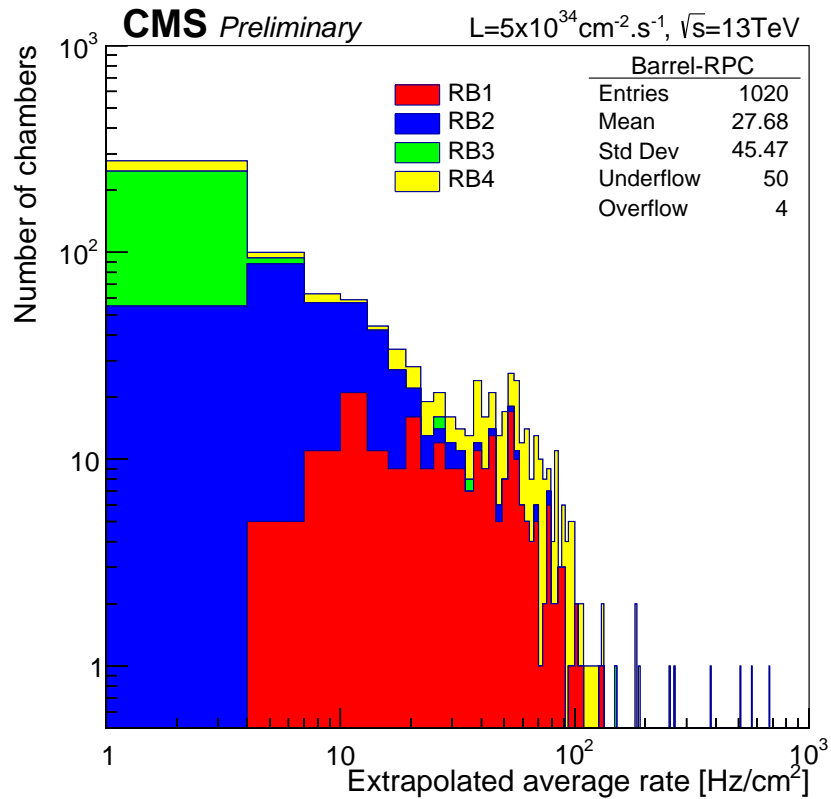
4.2 Testing detectors under extreme conditions

The upgrade from LHC to HL-LHC will increase the peak luminosity from $10^{34} \text{ cm}^{-2} \text{ s}^{-1}$ to reach $5 \times 10^{34} \text{ cm}^{-2} \text{ s}^{-1}$, increasing in the same way the total expected background to which the RPC system will be subjected to. Composed of low energy gammas and neutrons from $p\text{-}p$ collisions, low momentum primary and secondary muons, puch-through hadrons from calorimeters, and particles produced in the interaction of the beams with collimators, the background will mostly affect the regions of CMS that are the closest to the beam line, i.e. the RPC detectors located in the endcaps. [To update.]

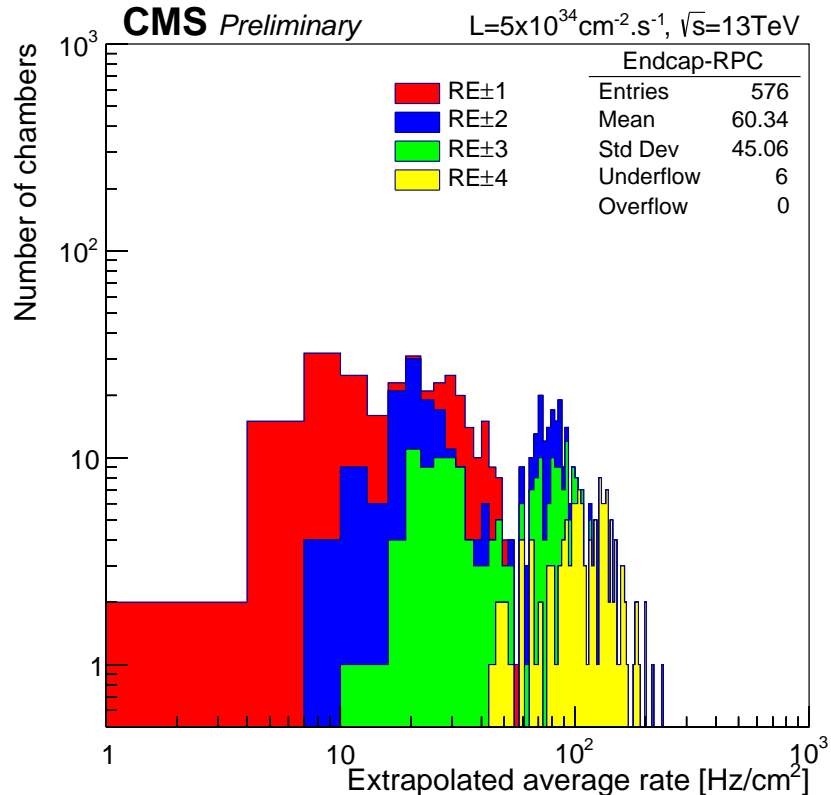
1452

1453 The 2016 data allowed to study the values of the background rate in all RPC system. In Fig-
1454 ure 4.3, the distribution of the chamber background hit rate per unit area is shown at a luminosity
1455 of $5 \times 10^{34} cm^{-2}.s^{-1}$ linearly extrapolating from data collected in 2016 [ref mentioning the linear
1456 dependency of rate vs lumi]. The maximum rate per unit area at HL-LHC conditions is expected to
1457 be of the order of $600 Hz/cm^2$ (including a safety factor 3). Nevertheless, Fluka simulations have
1458 conducted in order to understand the background at HL-LHC conditions. The comparison to the
1459 data has shown, in Figure 4.4, a discrepancy of a factor 2 even though the order of magnitude is
1460 consistent. [Understand mismatch.]

1461



(a)



(b)

Figure 4.3: (4.3a) Extrapolation from 2016 data of single hit rate per unit area in the barrel region. (4.3b) Extrapolation from 2016 data of single hit rate per unit area in the endcap region.

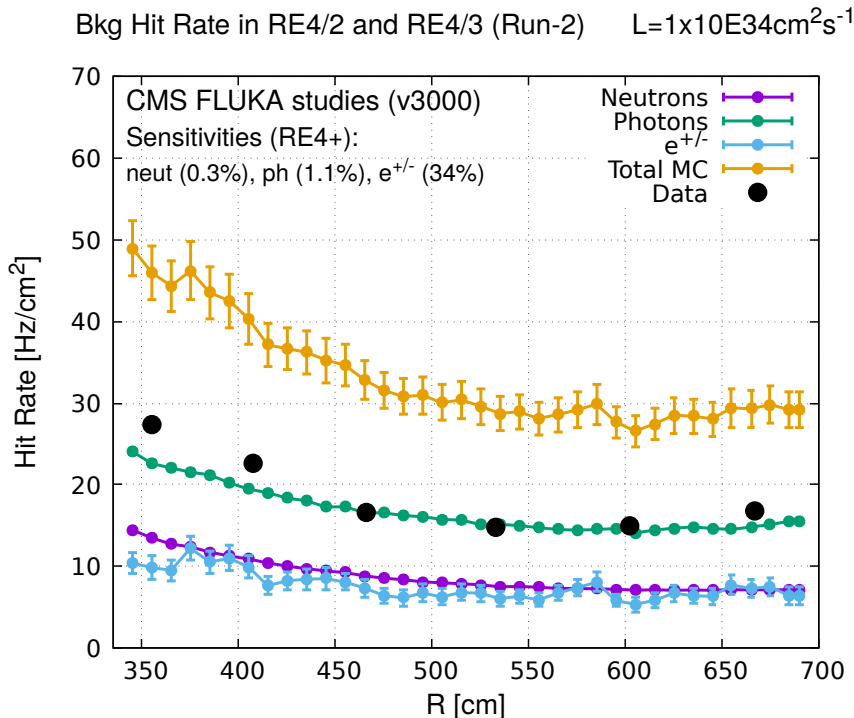


Figure 4.4: Background Fluka simulation compared to 2016 Data at $L = 10^{34} \text{ cm}^{-2} \cdot \text{s}^{-1}$ in the fourth endcap disk region. A mismatch in between simulation and data can be observed. [\[To be understood.\]](#)

In the past, extensive long-term tests were carried out at several gamma and neutron facilities certifying the detector performance. Both full size and small prototype RPCs have been irradiated with photons up to an integrated charge of $\sim 0.05 \text{ C}/\text{cm}^2$ and $\sim 0.4 \text{ C}/\text{cm}^2$, respectively [53, 54]. During Run-I, the RPC system provided stable operation and excellent performance and did not show any aging effects for integrated charge of the order of $0.01 \text{ C}/\text{cm}^2$. Projections on currents from 2016 Data, has allowed to determine that the total integrated charge, by the end of HL-LHC, would be of the order of $1 \text{ C}/\text{cm}^2$ (including a safety factor 3). [\[Corresponding figure needed.\]](#)

1469

1470 4.2.1 The Gamma Irradiation Facilities

1471 4.2.1.1 GIF

1472 Located in the SPS West Area at the downstream end of the X5 test beam, the Gamma Irradiation
 1473 Facility (GIF) was a test area in which particle detectors were exposed to a particle beam in presence
 1474 of an adjustable gamma background [55]. Its goal was to reproduce background conditions these
 1475 detectors would suffer in their operating environment at LHC. GIF layout is shown in Figure 4.5.
 1476 Gamma photons are produced by a strong ^{137}Cs source installed in the upstream part of the zone
 1477 inside a lead container. The source container includes a collimator, designed to irradiate a $6 \times 6 \text{ m}^2$
 1478 area at 5 m maximum to the source. A thin lens-shaped lead filter helps providing with a uniform
 1479 outcoming flux in a vertical plane, orthogonal to the beam direction. The principal collimator hole
 1480 provides a pyramidal aperture of $74^\circ \times 74^\circ$ solid angle and provides a photon flux in a pyramidal vol-

ume along the beam axis. The photon rate is controled by further lead filters allowing the maximum rate to be limited and to vary within a range of four orders of magnitude. Particle detectors under test are then placed within the pyramidal volume in front of the source, perpendicularly to the beam line in order to profit from the homogeneous photon flux. Adjusting the background flux of photons can then be done by using the filters and choosing the position of the detectors with respect to the source.

1486

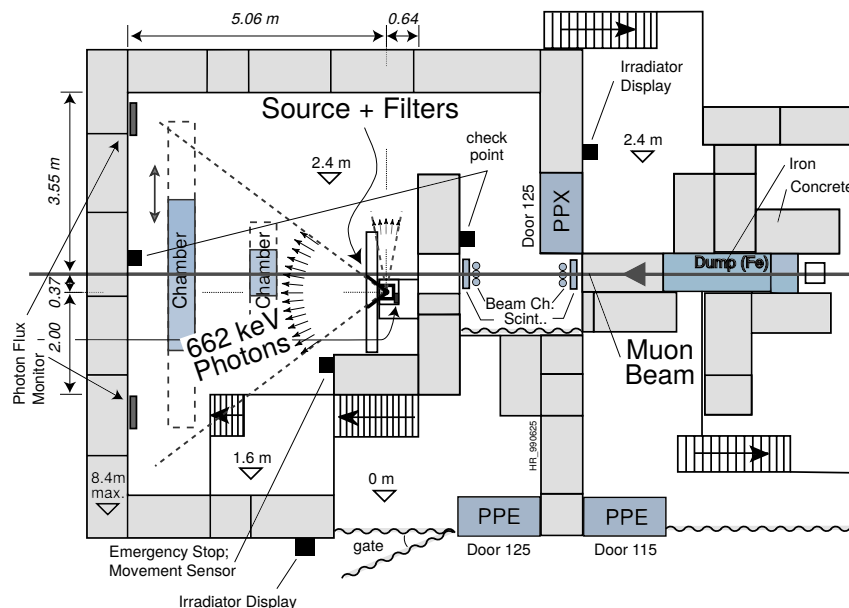


Figure 4.5: Layout of the test beam zone called X5c GIF at CERN. Photons from the radioactive source produce a sustained high rate of random hits over the whole area. The zone is surrounded by 8 m high and 80 cm thick concrete walls. Access is possible through three entry points. Two access doors for personnel and one large gate for material. A crane allows installation of heavy equipment in the area.

As described on Figure 4.6, the ^{137}Cs source emits a 662 keV photon in 85% of the decays. An activity of 740 GBq was measured on the 5th March 1997. To estimate the strength of the flux in 2014, it is necessary to consider the nuclear decay through time assiciated to the Cesium source whose half-life is well known ($t_{1/2} = (30.05 \pm 0.08)$ y). The GIF tests where done in between the 20th and the 31st of August 2014, i.e. at a time $t = (17.47 \pm 0.02)$ y resulting in an attenuation of the activity from 740 GBq in 1997 to 494 GBq in 2014.

1493

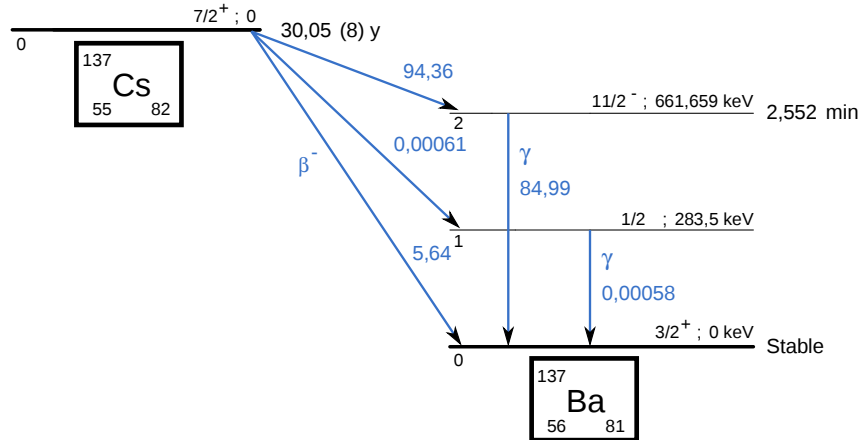


Figure 4.6: ^{137}Cs decays by β^- emission to the ground state of ^{137}Ba ($BR = 5.64\%$) and via the 662 keV isomeric level of ^{137}Ba ($BR = 94.36\%$) whose half-life is 2.55 min.

4.2.1.2 GIF++

The new Gamma Irradiation Facility (GIF++), located in the SPS North Area at the downstream end of the H4 test beam, has replaced its predecessor during LS1 and has been operational since spring 2015 [56]. Like GIF, GIF++ features a ^{137}Cs source of 662 keV gamma photons, their fluence being controlled with a set of filters of various attenuation factors. The source provides two separated large irradiation areas for testing several full-size muon detectors with continuous homogeneous irradiation, as presented in Figure 4.7.

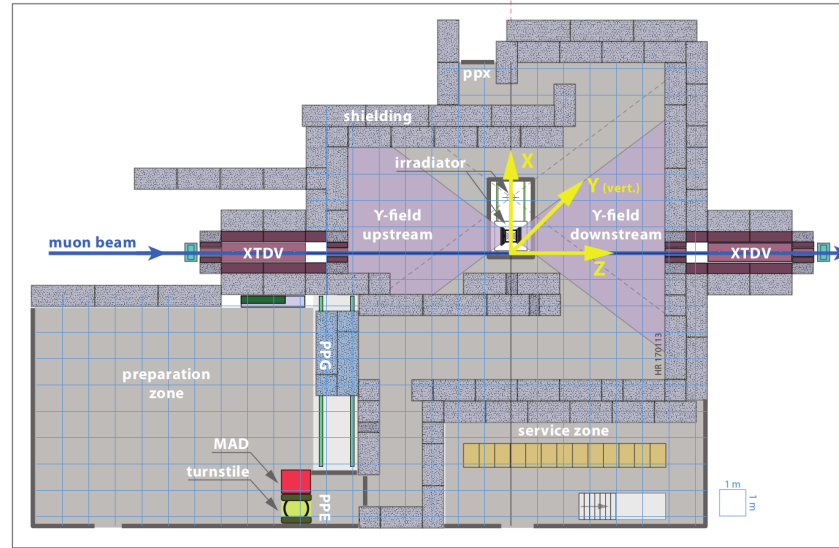


Figure 4.7: Floor plan of the GIF++ facility. When the facility downstream of the GIF++ takes electron beam, a beam pipe is installed along the beam line (z -axis). The irradiator can be displaced laterally (its center moves from $x = 0.65$ m to 2.15 m), to increase the distance to the beam pipe.

1502 The source activity was measured to be about 13.5 TBq in March 2016. The photon flux being
 1503 far greater than HL-LHC expectations, GIF++ provides an excellent facility for accelerated aging
 1504 tests of muon detectors.

1505

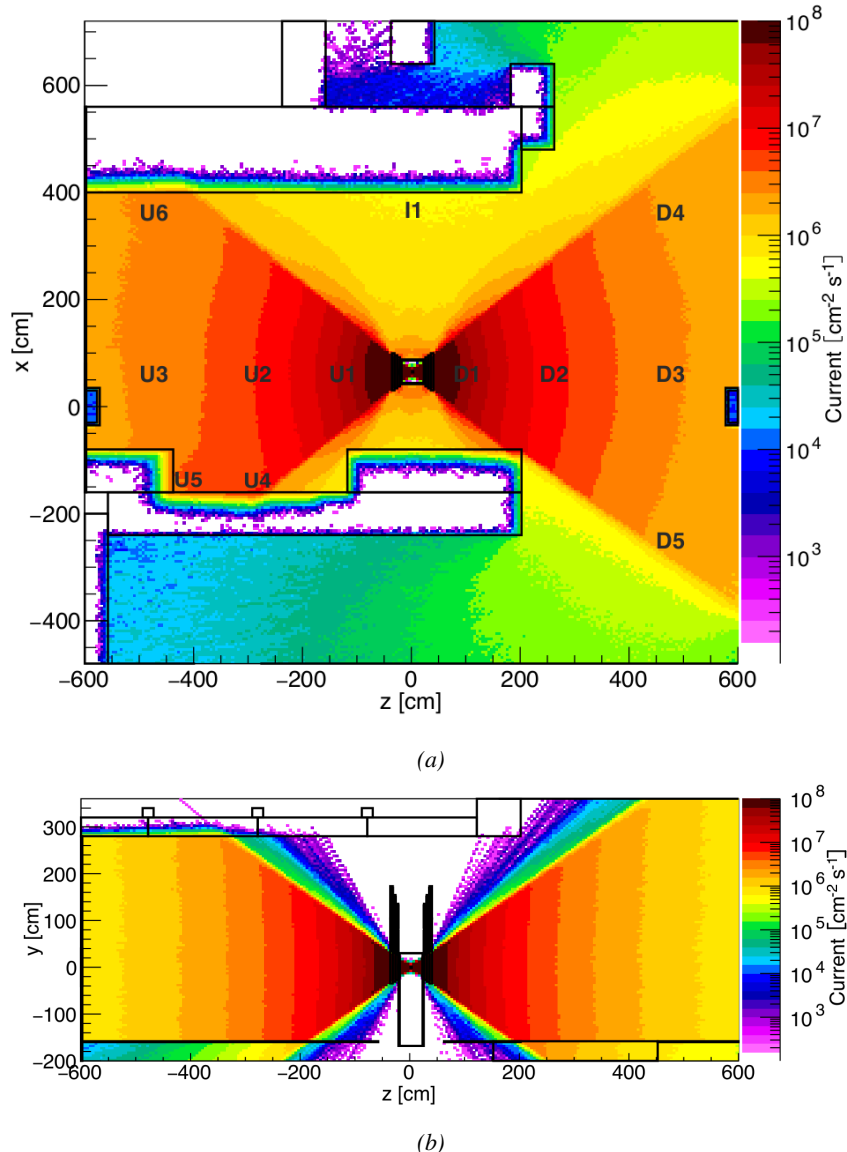


Figure 4.8: Simulated unattenuated current of photons in the xz plane (Figure 4.8a) and yz plane (Figure 4.8b) through the source at $x = 0.65$ m and $y = 0$ m. With angular correction filters, the current of 662 keV photons is made uniform in xy planes.

1506 The source is situated in the muon beam line with the muon beam being available a few times a
 1507 year. The H4 beam, composed of muons with a momentum of about 150 GeV/c, passes through the
 1508 GIF++ zone and is used to study the performance of the detectors. Its flux is of 104 particles/ cm^2

1509 focused in an area similar to $10 \times 10 \text{ cm}^2$. Therefore, with properly adjusted filters, one can imitate
 1510 the HL-LHC background and study the performance of muon detectors with their trigger/readout
 1511 electronics in HL-LHC environment.

1512

1513 4.3 Preliminary tests at GIF

1514 4.3.1 Resistive Plate Chamber test setup

1515 During summer 2014, preliminary tests have been conducted in the GIF area on a newly produced
 1516 RE4/2 chamber labelled RE-4-2-BARC-161. This chamber has been placed into a trolley covered
 1517 with a tent. The position of the RPC inside the tent and of the tent related to the source is described
 1518 in Figure 4.9. To test this CMS RPC, three different absorber settings were used. First of all,
 1519 measurements were done with fully opened source. Then, to complete this preliminary study, the
 1520 gamma flux has been attenuated from a factor 2 and a factor 5. The expected gamma flux at the level
 1521 of our detector will be discussed in subsection ??.

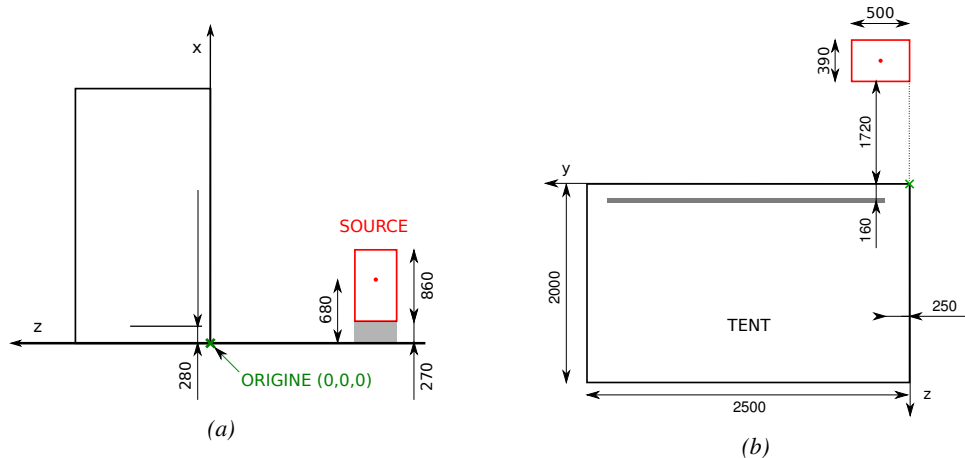


Figure 4.9: Description of the RPC setup. Dimensions are given in mm. A tent containing RPCs is placed at 1720 mm from the source container. The source is situated in the center of the container. RE-4-2-BARC-161 chamber is 160 mm inside the tent. This way, the distance between the source and the chambers plan is 2060 mm. Figure 4.9a provides a side view of the setup in the xz plane while Figure 4.9b shows a top view in the yz plane.



Figure 4.10: RE-4-2-BARC-I61 chamber is inside the tent as described in Figure 4.9. In the top right, the two scintillators used as trigger can be seen. This trigger system has an inclination of 10° relative to horizontal and is placed above half-partition B2 of the RPCs. PMT electronics are shielded thanks to lead blocks placed in order to protect them without stopping photons from going through the scintillators and the chamber.

1522 At the time of the tests, the beam not being operational anymore, a trigger composed of 2 plastic
 1523 scintillators has been placed in front of the setup with an inclination of 10 deg with respect to the
 1524 detector plane in order to look at cosmic muons. Using this particular trigger layout, shown on Fig-
 1525 ure 4.10, leads to a cosmic muon hit distribution into the chamber similar to the one in Figure 4.11.
 1526 Measured without gamma irradiation, two peaks can be seen on the profile of partition B, centered
 1527 on strips 52 and 59. Section ?? will help us understand that these two peaks are due respectively to
 1528 forward and backward coming cosmic particles where forward coming particles are first detected by
 1529 the scintillators and then the RPC while the backward coming muons are first detected in the RPC.

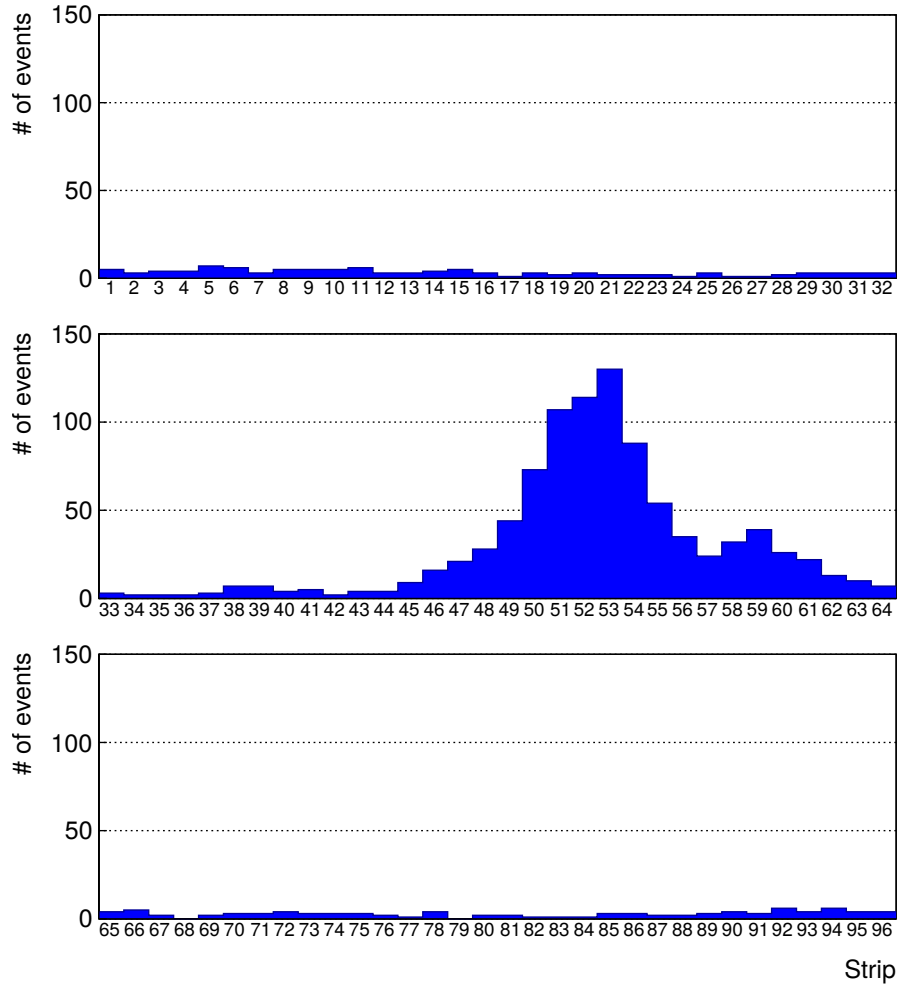


Figure 4.11: Hit distributions over all 3 partitions of RE-4-2-BARC-161 chamber is showed on these plots. Top, middle and bottom figures respectively correspond to partitions A, B, and C. These plots show that some events still occur in other half-partitions than B2, which corresponds to strips 49 to 64, in front of which the trigger is placed, contributing to the inefficiency of detection of cosmic muons. In the case of partitions A and C, the very low amount of data can be interpreted as noise. On the other hand, it is clear that a little portion of muons reach the half-partition B1, corresponding to strips 33 to 48.

1530 4.3.2 Data Acquisition

1531 4.3.3 Geometrical acceptance of the setup layout to cosmic muons

1532 In order to profit from a constant gamma irradiation, the detectors inside of the GIF bunker need
 1533 to be placed in a plane orthogonal to the beam line. The muon beam that used to be available was
 1534 meant to test the performance of detectors under test. This beam not being active anymore, another
 1535 solution to test detector performance had to be used. Thus, it has been decided to use cosmic muons
 1536 detected through a telescope composed of two scintillators. Lead blocks were used as shielding to

protect the photomultipliers from gammas as can be seen from Figure 4.10.

An inclination has been given to the cosmic telescope to maximize the muon flux. A good compromise had to be found between good enough muon flux and narrow enough hit distribution to be sure to contain all the events into only one half partitions as required from the limited available readout hardware. Nevertheless, a consequence of the misplaced trigger, that can be seen as a loss of events in half-partition B1 in Figure 4.11, is an inefficiency. Nevertheless, the inefficiency of approximately 20 % highlighted in Figure 4.12 by comparing the performance of chamber BARC-161 in 904 and at GIF without irradiation seems too important to be explained only by the geometrical acceptance of the setup itself. Simulations have been conducted to show how the setup brings inefficiency.

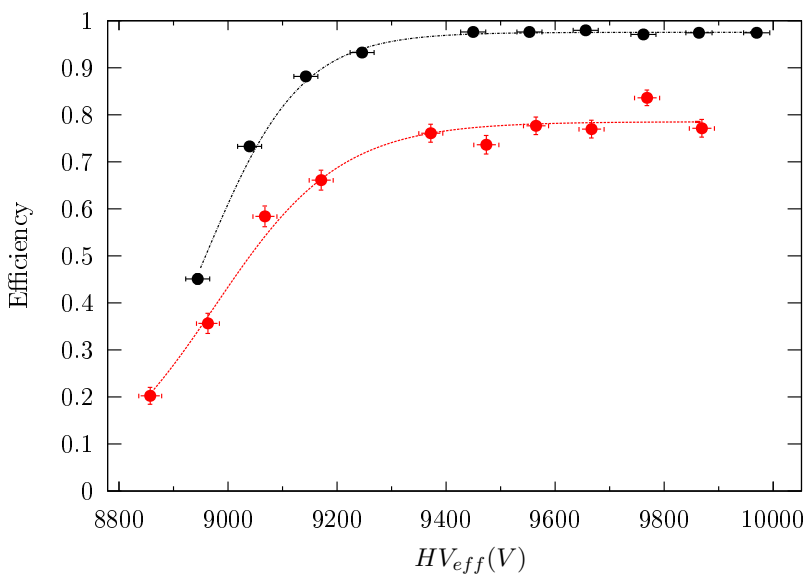


Figure 4.12: Results are derived from data taken on half-partition B2 only. On the 18th of June 2014, data has been taken on chamber RE-2-BARC-161 at building 904 (Prevessin Site) with cosmic muons providing us a reference efficiency plateau of $(97.54 \pm 0.15)\%$ represented by a black curve. A similar measurement has been done at GIF on the 21st of July with the same chamber giving a plateau of $(78.52 \pm 0.94)\%$ represented by a red curve.

4.3.3.1 Description of the simulation layout

The layout of GIF setup has been reproduced and incorporated into a Monte Carlo (MC) simulation to study the influence of the disposition of the telescope on the final distribution measured by the RPC. A 3D view of the simulated layout is given into Figure 4.13. Muons are generated randomly in a horizontal plane located at a height corresponding to the lowest point of the PMTs. This way, the needed size of the plane in order to simulate events happening at very big azimuthal angles (i.e. $\theta \approx \pi$) can be kept relatively small. The muon flux is designed to follow the usual $\cos^2\theta$ distribution for cosmic particle. The goal of the simulation is to look at muons that pass through the muon telescope composed of the two scintillators and define their distribution onto the RPC plane. During the reconstruction, the RPC plane is then divided into its strips and each muon track is assigned to a strip.

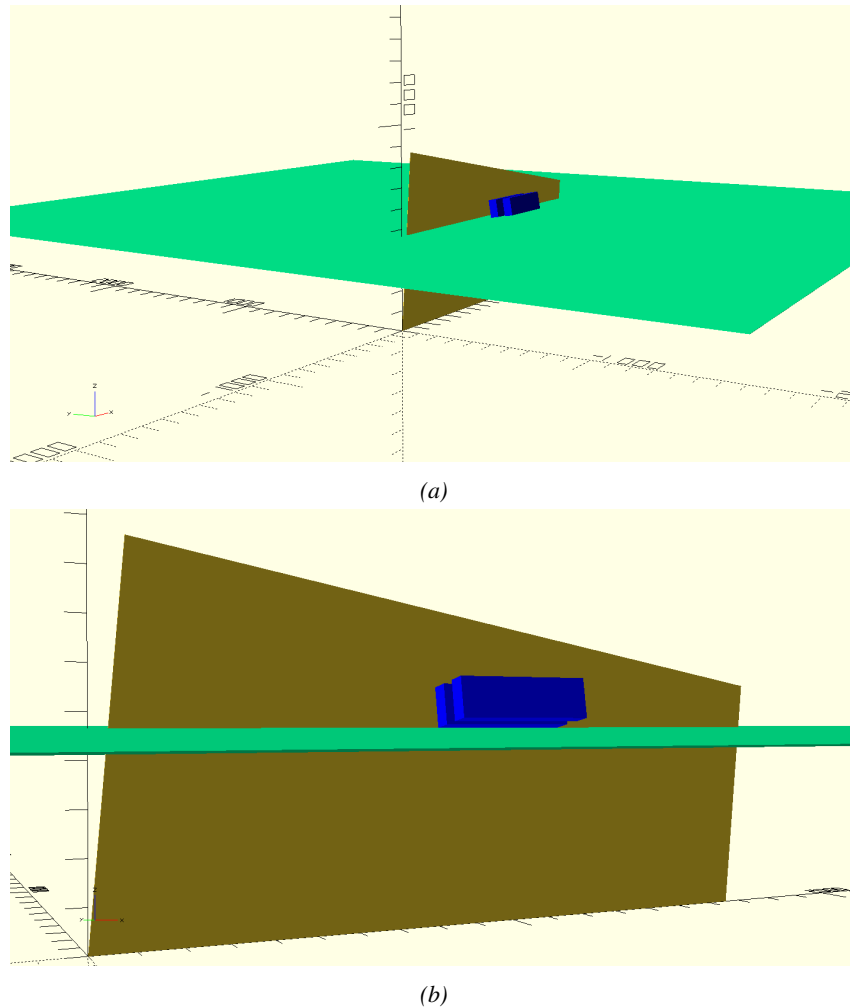


Figure 4.13: Representation of the layout used for the simulations of the test setup. The RPC is represented as a yellow trapezoid while the two scintillators as blue cuboids looking at the sky. A green plane corresponds to the muon generation plane within the simulation. Figure 4.9a shows a global view of the simulated setup. Figure 4.9b shows a zoomed view that allows to see the 2 scintillators as well as the full RPC plane.

1558 In order to further refine the quality of the simulation and understand deeper the results the
 1559 dependance of the distribution has been studied for a range of telescope inclinations. Moreover,
 1560 the threshold applied on the PMT signals has been included into the simulation in the form of a
 1561 cut. In the approximation of uniform scintillators, it has been considered that the threshold can be
 1562 understood as the minimum distance particles need to travel through the scintillating material to give
 1563 a strong enough signal. Particles that travel a distance smaller than the set "threshold" are thus not
 1564 detected by the telescope and cannot trigger the data taking. Finally, the FEE threshold also has
 1565 been considered in a similar way. The mean momentum of horizontal cosmic rays is higher than
 1566 those of vertical ones but the stopping power of matter for momenta ranging from 1 GeV to 1 TeV
 1567 stays comparable. It is then possible to assume that the mean number of primary e^-/ion pairs per
 1568 unit length will stay similar and thus, depending on the applied discriminator threshold, muons with

1569 the shortest path through the gas volume will deposit less charge and induce a smaller signal on the
 1570 pick-up strips that could eventually not be detected. These two thresholds also restrain the overall
 1571 geometrical acceptance of the system.

1572 4.3.3.2 Simulation procedure

1573 The simulation software has been designed using C++ and the output data is saved into ROOT
 1574 histograms. Simulations start for a threshold T_{scint} varying in a range from 0 to 45 mm in steps
 1575 of 5 mm, where $T_{scint} = 0$ mm corresponds to the case where there isn't any threshold apply on
 1576 the input signal while $T_{scint} = 45$ mm, which is the scintillator thickness, is the case where muons
 1577 cannot arrive orthogonally onto the scintillator surface. For a given T_{scint} , a set of RPC thresholds
 1578 are considered. The RPC threshold, T_{RPC} varies from 2 mm, the thickness of the gas volume, to
 1579 3 mm in steps of 0.25 mm. For each $(T_{scint}; T_{RPC})$ pair, $N_\mu = 10^8$ muons are randomly generated
 1580 inside the muon plane described in the previous paragraph with an azimuthal angle θ chosen to follow
 1581 a $\cos^2\theta$ distribution.

1582 Planes are associated to each surface of the scintillators. Knowing muon position into the muon
 1583 plane and its direction allows us, by assuming that muons travel in a straight line, to compute the
 1584 intersection of the muon track with these planes. Applying conditions to the limits of the surfaces
 1585 of the scintillator faces then gives us an answer to whether or not the muon passed through the
 1586 scintillators. In the case the muon has indeed passed through the telescope, the path through each
 1587 scintillator is computed and muons whose path was shorter than T_{scint} are rejected and are thus
 1588 considered as having not interacted with the setup.

1589 On the contrary, if the muon is labeled as good, its position within the RPC plane is computed
 1590 and the corresponding strip, determined by geometrical tests in the case the distance through the
 1591 gas volume was enough not to be rejected because of T_{RPC} , gets a hit and several histograms
 1592 are filled in order to keep track of the generation point on the muon plane, the intersection points
 1593 of the reconstructed muons within the telescope, or on the RPC plane, the path traveled through
 1594 each individual scintillator or the gas volume, as well as other histograms. Moreover, muons fill
 1595 different histograms whether they are forward or backward coming muons. They are discriminated
 1596 according to their direction components. When a muon is generated, an (x, y, z) position is assigned
 1597 into the muon plane as well as a $(\theta; \phi)$ pair that gives us the direction it's coming from. This way,
 1598 muons satisfying the condition $0 \leq \phi < \pi$ are designated as backward coming muons while muons
 1599 satisfying $\pi \leq \phi < 2\pi$ as forward coming muons.

1600 This simulation is then repeated for different telescope inclinations ranging in between 4 and 20°
 1601 and varying in steps of 2°. Due to this inclination and to the vertical position of the detector under
 1602 test, the muon distribution reconstructed in the detector plane is asymmetrical. The choice as been
 1603 made to chose a skew distribution formula to fit the data built as the multiplication of gaussian and
 1604 sigmoidal curves together. A typical gaussian formula is given as 4.1 and has three free parameters
 1605 as A_g , its amplitude, \bar{x} , its mean value and σ , its root mean square. Sigmoidal curves as given by
 1606 formula 4.2 are functions converging to 0 and A_s as x diverges. The inflection point is given as x_i
 1607 and λ is proportional to the slope at $x = x_i$. In the limit where $\lambda \rightarrow \infty$, the sigmoid becomes a
 1608 step function.

$$g(x) = A_g e^{-\frac{(x-\bar{x})^2}{2\sigma^2}} \quad (4.1)$$

$$s(x) = \frac{A_s}{1 + e^{-\lambda(x-x_i)}} \quad (4.2)$$

¹⁶⁰⁹ Finally, a possible representation of a skew distribution is given by formula 4.3 and is the product
¹⁶¹⁰ of 4.1 and 4.2. Naturally, here $A_{sk} = A_g \times A_s$ and represents the theoretical maximum in the limit
¹⁶¹¹ where the skew tends to a gaussian function.

$$sk(x) = g(x) \times s(x) = A_{sk} \frac{e^{\frac{-(x-\bar{x})^2}{2\sigma^2}}}{1 + e^{-\lambda(x-x_i)}} \quad (4.3)$$

¹⁶¹² 4.3.3.3 Results

¹⁶¹³ Influence of T_{scint} on the muon distribution

¹⁶¹⁴ Influence of T_{RPC} on the muon distribution

¹⁶¹⁵ Influence of the telescope inclination on the muon distribution

¹⁶¹⁶ Comparison to data taken at GIF without irradiation

¹⁶¹⁷ 4.3.4 Photon flux at GIF

¹⁶¹⁸ 4.3.4.1 Expectations from simulations

¹⁶¹⁹ In order to understand and evaluate the γ flux in the GIF area, simulations had been conducted in
¹⁶²⁰ 1999 and published by S. Agosteo et al [55]. Table 4.1 presented in this article gives us the γ flux
¹⁶²¹ for different distances D to the source. This simulation was done using GEANT and a Monte Carlo
¹⁶²² N-Particle (MCNP) transport code, and the flux F is given in number of γ per unit area and unit time
¹⁶²³ along with the estimated error from these packages expressed in %.

Nominal ABS	Photon flux F [$s^{-1}cm^{-2}$]			
	at $D = 50$ cm	at $D = 155$ cm	at $D = 300$ cm	at $D = 400$ cm
1	$0.12 \cdot 10^8 \pm 0.2\%$	$0.14 \cdot 10^7 \pm 0.5\%$	$0.45 \cdot 10^6 \pm 0.5\%$	$0.28 \cdot 10^6 \pm 0.5\%$
2	$0.68 \cdot 10^7 \pm 0.3\%$	$0.80 \cdot 10^6 \pm 0.8\%$	$0.25 \cdot 10^6 \pm 0.8\%$	$0.16 \cdot 10^6 \pm 0.6\%$
5	$0.31 \cdot 10^7 \pm 0.4\%$	$0.36 \cdot 10^6 \pm 1.2\%$	$0.11 \cdot 10^6 \pm 1.2\%$	$0.70 \cdot 10^5 \pm 0.9\%$

Table 4.1: Total photon flux ($E\gamma \leq 662$ keV) with statistical error predicted considering a ^{137}Cs activity of 740 GBq at different values of the distance D to the source along the x -axis of irradiation field [55].

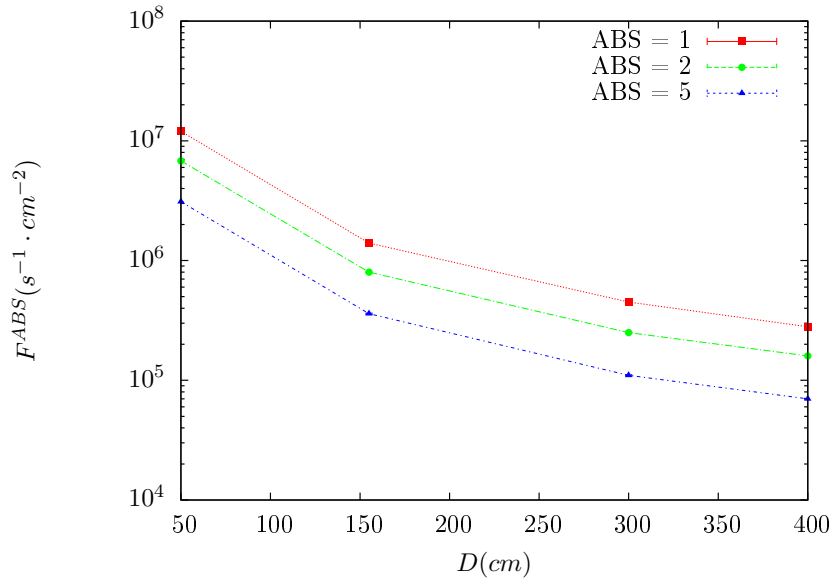


Figure 4.14: γ flux $F(D)$ is plot using values from table 4.1. As expected, the plot shows similar attenuation behaviours with increasing distance for each absorption factors.

The simulation doesn't directly provides us with an estimated flux at the level of our RPC. First of all, it is needed to extract the value of the flux from the available data contained in the original paper and then to estimate the flux in 2014 at the time the experimentation took place. Figure 4.14 that contains the data from Table 4.1. In the case of a pointlike source emitting isotropic and homogeneous gamma radiations, the gamma flux F at a distance D to the source with respect to a reference point situated at D_0 where a known flux F_0 is measured will be expressed like in Equation 4.4, assuming that the flux decreases as $1/D^2$, where c is a fitting factor.

$$F^{ABS} = F_0^{ABS} \times \left(\frac{cD_0}{D} \right)^2 \quad (4.4)$$

By rewriting Equation 4.4, it comes that :

$$c = \frac{D}{D_0} \sqrt{\frac{F^{ABS}}{F_0^{ABS}}} \quad (4.5)$$

$$\Delta c = \frac{c}{2} \left(\frac{\Delta F^{ABS}}{F^{ABS}} + \frac{\Delta F_0^{ABS}}{F_0^{ABS}} \right) \quad (4.6)$$

Finally, using Equation 4.5 and the data in Table 4.1 with $D_0 = 50$ cm as reference point, we can build Table 4.2. It is interesting to note that c for each value of D doesn't depend on the absorption factor.

Nominal ABS	Correction factor c		
	at $D = 155$ cm	at $D = 300$ cm	at $D = 400$ cm
1	$1.059 \pm 0.70\%$	$1.162 \pm 0.70\%$	$1.222 \pm 0.70\%$
2	$1.063 \pm 1.10\%$	$1.150 \pm 1.10\%$	$1.227 \pm 0.90\%$
5	$1.056 \pm 1.60\%$	$1.130 \pm 1.60\%$	$1.202 \pm 1.30\%$

Table 4.2: Correction factor c is computed thanks to formulae 4.5 taking as reference $D_0 = 50$ cm and the associated flux F_0^{ABS} for each absorption factor available in table 4.1.

¹⁶³⁵ For the range of D/D_0 values available, it is possible to use a simple linear fit to get the evolution
¹⁶³⁶ of c . The linear fit will then use only 2 free parameters, a and b , as written in Equation 4.7. This gives
¹⁶³⁷ us the results showed in Figure 4.15. Figure 4.15b confirms that using only a linear fit to extract c is
¹⁶³⁸ enough as the evolution of the rate that can be obtained superimposes well on the simulation points.

$$c \left(\frac{D}{D_0} \right) = a \frac{D}{D_0} + b \quad (4.7)$$

$$F^{ABS} = F_0^{ABS} \left(a + \frac{b D_0}{D} \right)^2 \quad (4.8)$$

$$\Delta F^{ABS} = F^{ABS} \left[\frac{\Delta F_0^{ABS}}{F_0^{ABS}} + 2 \frac{\Delta a + \Delta b \frac{D_0}{D}}{a + \frac{b D_0}{D}} \right] \quad (4.9)$$

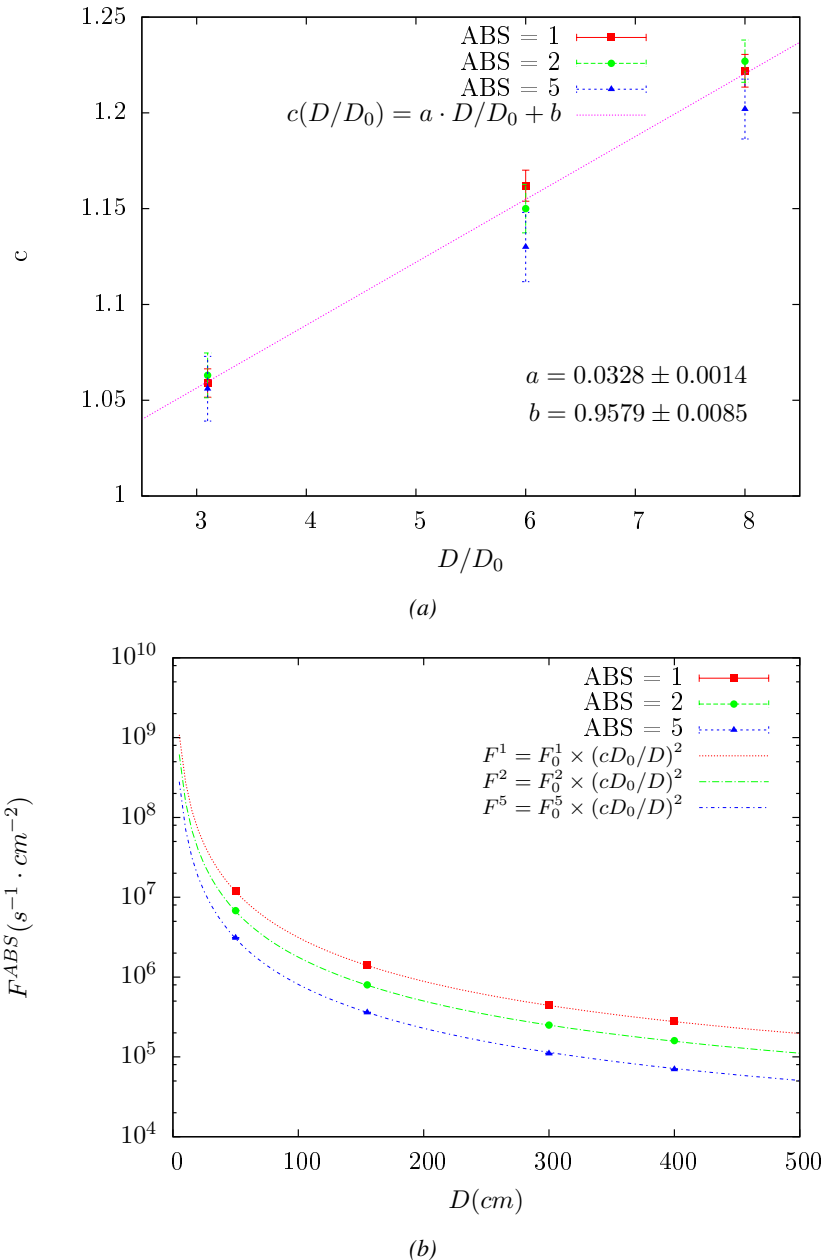


Figure 4.15: Figure 4.15a shows the linear approximation fit done via formulae 4.7 on data from table 4.2. Figure 4.15b shows a comparison of this model with the simulated flux using a and b given in figure 4.15a in formulae 4.4 and the reference value $D_0 = 50\text{cm}$ and the associated flux for each absorption factor F_0^{ABS} from table 4.1

In the case of the 2014 GIF tests, the RPC plane is located at a distance $D = 206\text{ cm}$ to the source. Moreover, to estimate the strength of the flux in 2014, it is necessary to consider the nuclear decay through time associated to the Cesium source whose half-life is well known ($t_{1/2} = (30.05 \pm 0.08)\text{ y}$). The very first source activity measurement has been done on the 5th of March 1997 while the GIF

1643 tests where done in between the 20th and the 31st of August 2014, i.e. at a time $t = (17.47 \pm 0.02)$ y
 1644 resulting in an attenuation of the activity from 740 GBq in 1997 to 494 GBq in 2014. All the needed
 1645 information to extrapolate the flux through our detector in 2014 has now been assembled, leading
 1646 to the Table 4.3. It is interesting to note that for a common RPC sensitivity to γ of $2 \cdot 10^{-3}$, the
 1647 order of magnitude of the estimated hit rate per unit area is of the order of the kHz for the fully
 1648 opened source. Moreover, taking profit of the two working absorbers, it will be possible to scan
 1649 background rates at 0 Hz, ~ 300 Hz as well as ~ 600 Hz. Without source, a good estimate of the
 1650 intrinsic performance will be available. Then at 300 Hz, the goal will be to show that the detectors
 1651 fulfill the performance certification of CMS RPCs. Then a first idea of the performance of the
 1652 detectors at higher background will be provided with absorption factors 2 (~ 600 Hz) and 1 (no
 1653 absorption). *[Here I will also put a reference to the plot showing the estimated background rate at
 1654 the level of RE3/1 in the case of HL-LHC but this one being in another chapter, I will do it later.]*

Nominal ABS	Photon flux F [$s^{-1}cm^{-2}$]			Hit rate/unit area [$Hz cm^{-2}$] at $D^{2014} = 206$ cm
	at $D_0^{1997} = 50$ cm	at $D^{1997} = 206$ cm	at $D^{2014} = 206$ cm	
1	$0.12 \cdot 10^8 \pm 0.2\%$	$0.84 \cdot 10^6 \pm 0.3\%$	$0.56 \cdot 10^6 \pm 0.3\%$	1129 ± 32
2	$0.68 \cdot 10^7 \pm 0.3\%$	$0.48 \cdot 10^6 \pm 0.3\%$	$0.32 \cdot 10^6 \pm 0.3\%$	640 ± 19
5	$0.31 \cdot 10^7 \pm 0.4\%$	$0.22 \cdot 10^6 \pm 0.3\%$	$0.15 \cdot 10^6 \pm 0.3\%$	292 ± 9

Table 4.3: The data at D_0 in 1997 is taken from [55]. In a second step, using Equations 4.8 and 4.9, the flux at D can be estimated in 1997. Then, taking into account the attenuation of the source activity, the flux at D can be estimated at the time of the tests in GIF in 2014. Finally, assuming a sensitivity of the RPC to γ $s = 2 \cdot 10^{-3}$, an estimation of the hit rate per unit area is obtained.

1655 **4.3.4.2 Dose measurements**

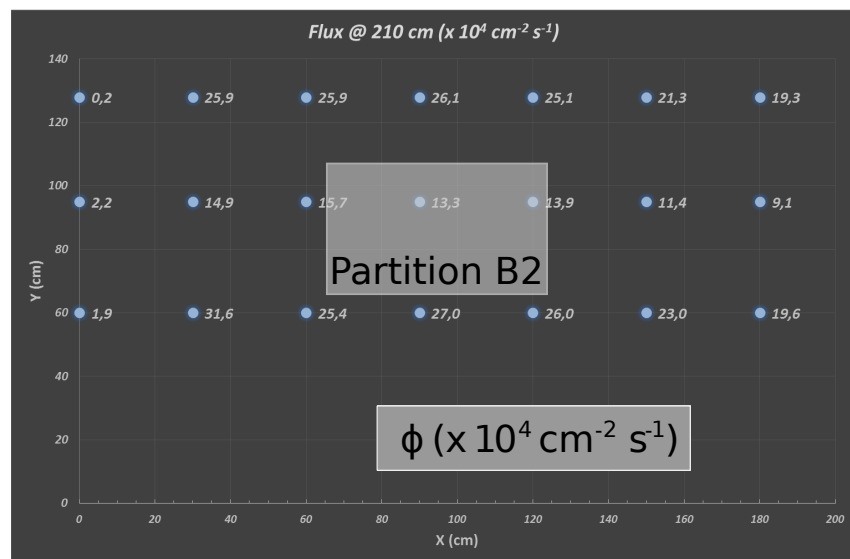


Figure 4.16: Dose measurements has been done in a plane corresponding to the tents front side. This plan is 1900 mm away from the source. As explained in the first chapter, a lens-shaped lead filter provides a uniform photon flux in the vertical plan orthogonal to the beam direction. If the second line of measured fluxes is not taken into account because of lower values due to experimental equipments in the way between the source and the tent, the uniformity of the flux is well showed by the results.

₁₆₅₆ **4.3.5 Results and discussions**

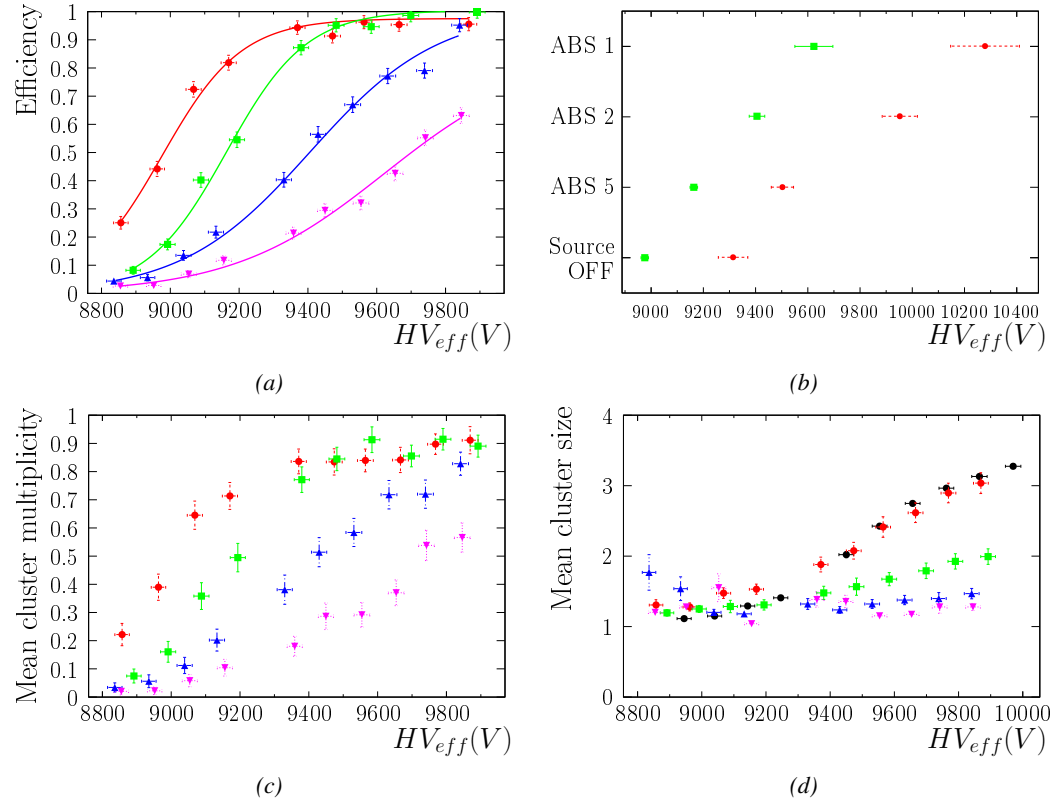


Figure 4.17

1657 4.4 Longevity tests at GIF++

1658 Longevity studies imply a monitoring of the performance of the detectors probed using a high inten-
1659 sity muon beam in a irradiated environment by periodically measuring their rate capability, the dark
1660 current running through them and the bulk resistivity of the Bakelite composing their electrodes.
1661 GIF++, with its very intense ^{137}Cs source, provides the perfect environment to perform such kind
1662 of tests. Assuming a maximum acceleration factor of 3, it is expected to accumulate the equivalent
1663 charge in 1.7 years.

1664 As the maximum background is found in the endcap, the choice naturally was made to focus the
1665 GIF++ longevity studies on endcap chambers. Most of the RPC system was installed in 2007. Nev-
1666 ertheless, the large chambers in the fourth endcap (RE4/2 and RE4/3) have been installed during
1667 LS1 in 2014. The Bakelite of these two different productions having different properties, four spare
1668 chambers of the present system were selected, two RE2,3/2 spares and two RE4/2 spares. Having
1669 two chambers of each type allows to always keep one of them non irradiated as reference, the per-
1670 formance evolution of the irradiated chamber being then compared through time to the performance
1671 of the non irradiated one.

1672 The performance of the detectors under different level of irradiation is measured periodically dur-
1673 ing dedicated test beam periods using the H4 muon beam. In between these test beam periods, the
1674 two RE2,3/2 and RE4/2 chambers selected for this study are irradiated by the ^{137}Cs source in order
1675 to accumulate charge and the gamma background is monitored, as well as the currents. The two
1676 remaining chambers are kept non-irradiated as reference detectors. Due to the limited gas flow in
1677 GIF++, the RE4 chamber remained non-irradiated until end of November 2016 where a new mass
1678 flow controller has been installed allowing for bigger volumes of gas to flow in the system.

1679 Figures 4.18 and 4.19 give us for different test beam periods, and thus for increasing integrated
1680 charge through time, a comparison of the maximum efficiency, obtained using a sigmoid-like func-
1681 tion, and of the working point of both irradiated and non irradiated chambers [**SIGMOID2005**]. No
1682 aging is yet to see from this data, the shifts in γ rate per unit area in between irradiated and non
1683 irradiated detectors and RE2 and RE4 types being easily explained by a difference of sensitivity due
1684 to the various Bakelite resistivities of the HPL electrodes used for the electrode production.

1685 Collecting performance data at each test beam period allows us to extrapolate the maximum effi-
1686 ciency for a background hit rate of $300\text{ Hz}/\text{cm}^2$ corresponding to the expected HL-LHC conditions.
1687 Aging effects could emerge from a loss of efficiency with increasing integrated charge over time,
1688 thus Figure 4.20 helps us understand such degradation of the performance of irradiated detectors in
1689 comparison with non irradiated ones. The final answer for an eventual loss of efficiency is given in
1690 Figure 4.21 by comparing for both irradiated and non irradiated detectors the efficiency sigmoids
1691 before and after the longevity study. Moreover, to complete the performance information, the Bake-
1692 lite resistivity is regularly measured thanks to Ag scans (Figure 4.22) and the noise rate is monitored
1693 weekly during irradiation periods (Figure 4.23). At the end of 2016, no signs of aging were observed
1694 and further investigation is needed to get closer to the final integrated charge requirements proposed
1695 for the longevity study of the present CMS RPC sub-system.

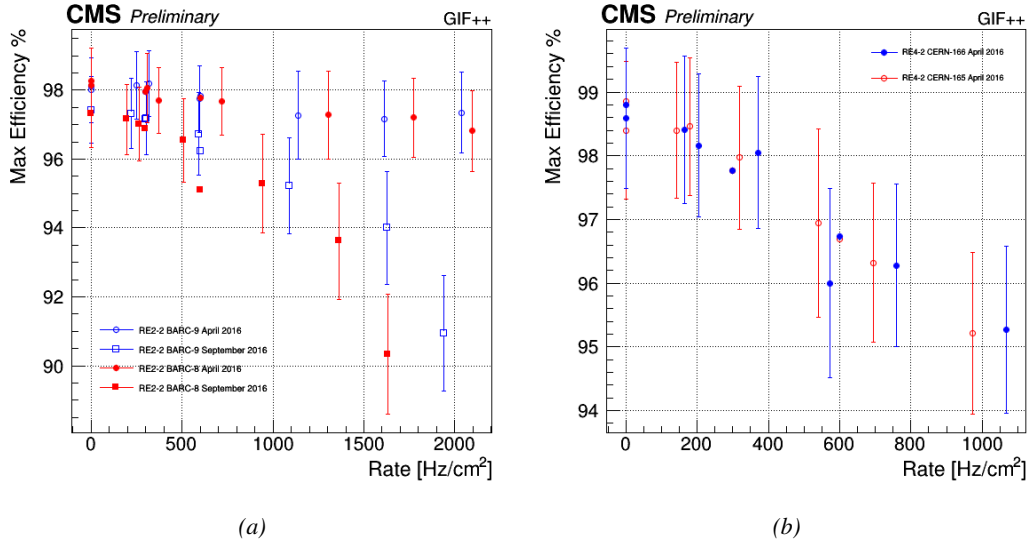


Figure 4.18: Evolution of the maximum efficiency for RE2 (4.18a) and RE4 (4.18b) chambers with increasing extrapolated γ rate per unit area at working point. Both irradiated (blue) and non irradiated (red) chambers are shown.

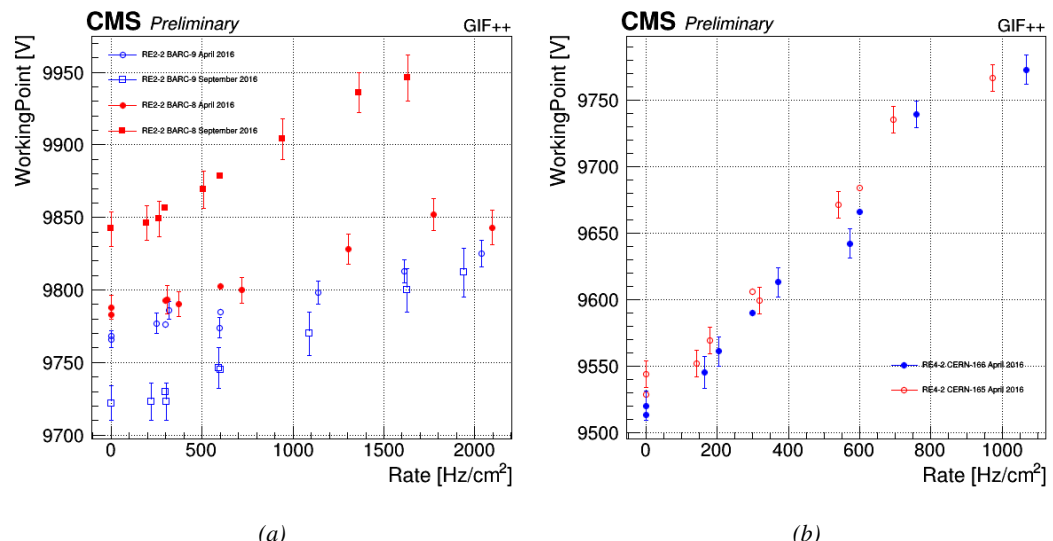


Figure 4.19: Evolution of the working point for RE2 (4.19a) and RE4 (4.19b) with increasing extrapolated γ rate per unit area at working point. Both irradiated (blue) and non irradiated (red) chambers are shown.

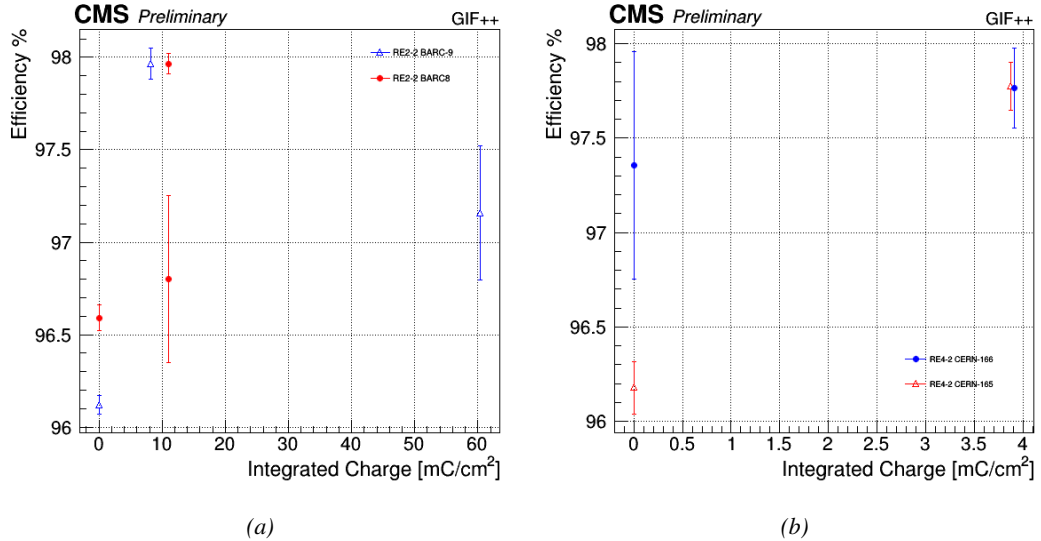


Figure 4.20: Evolution of the maximum efficiency at HL-LHC conditions, i.e. a background hit rate per unit area of 300 Hz/cm², with increasing integrated charge for RE2 (4.20a) and RE4 (4.20b) detectors. Both irradiated (blue) and non irradiated (red) chambers are shown. The integrated charge for non irradiated detectors is recorded during test beam periods and stays small with respect to the charge accumulated in irradiated chambers.

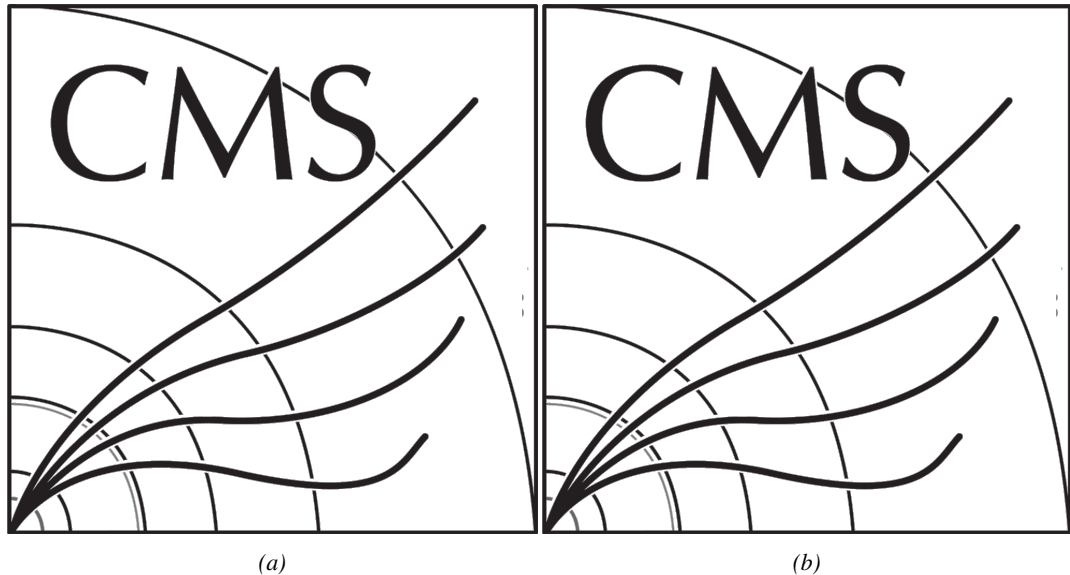


Figure 4.21: Comparison of the efficiency sigmoid before (triangles) and after (circles) irradiation for RE2 (4.21a) and RE4 (4.21b) detectors. Both irradiated (blue) and non irradiated (red) chambers are shown.

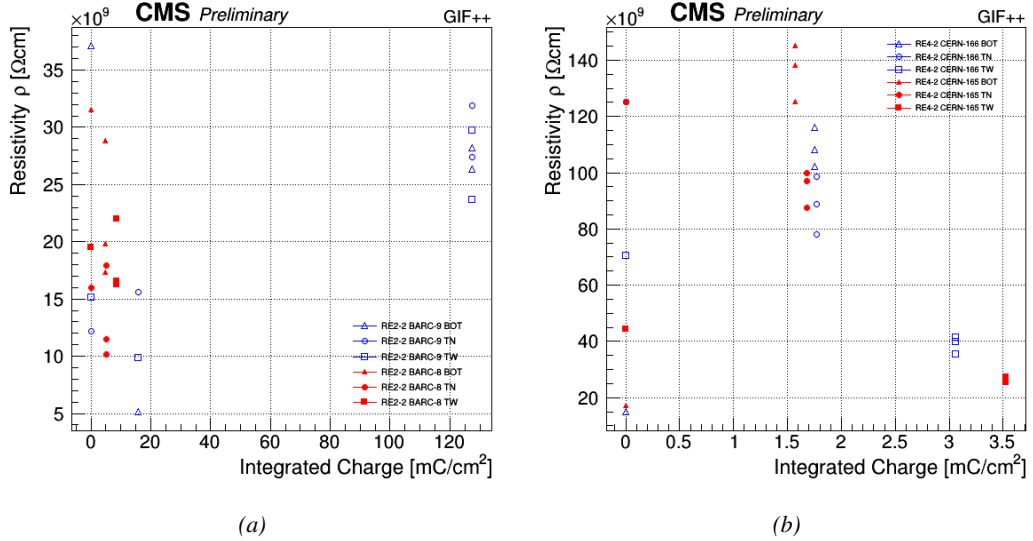


Figure 4.22: Evolution of the Bakelite resistivity for RE2 (4.22a) and RE4 (4.22b) detectors. Both irradiated (blue) and non-irradiated (red) chambers are shown.

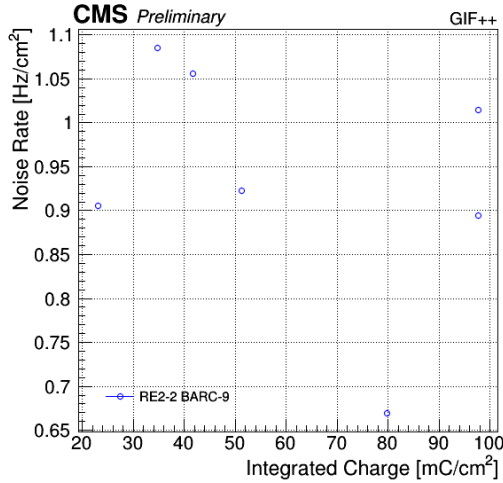


Figure 4.23: Evolution of the noise rate per unit area for the irradiated chamber RE2-2-BARC-9 only.

4.4.1 Description of the Data Acquisition

For the longevity studies, four spare chambers of the present system are used. Two spare RPCs of the RE2,3 stations as well as two spare RPCs from the new RE4 stations have been mounted in a Trolley. Six RE4 gaps are also placed in the trolley. The trolley is placed inside the GIFT++ in the upstream region of the bunker, taking the cesium source as a reference. The trolley is oriented for the detection surface of the chambers to be orthogonal to the beam line. The system can be moved along the orthogonal plane in order to have the beam in all η -partitions. For the aging the trolley is

1704 moved outside the beam line and is placed in a distance of 5.2 m to the source, which irradiates the
 1705 bunker using an attenuation filter of 2.2 which corresponds to a fluence of 10^7 gamma/cm^2 .

1706 During GIF++ operation, the data collected can be divided into different categories as several
 1707 parameters are monitored in addition to the usual RPC performance data. On one hand, to know
 1708 the performance of a chamber, it is need to measure its efficiency and to know the background
 1709 conditions in which it is operated. To do this, the hit signals from the chamber are recorded and
 1710 stored in a ROOT file via a Data Acquisition (DAQ) software. On the other hand, it is also very
 1711 important to monitor parameters such as environmental pressure and temperature, gas temperature
 1712 and humidity, RPC HV, LV, and currents, or even source and beam status. This is done through the
 1713 GIF++ web Detector Control Software (DCS) that stores this information in a database.

1714 Two different types of tests are conducted on RPCs via the DAQ. Indeed, the performance of the
 1715 detectors is measured periodically during dedicated test beam periods using the H4 muon beam. In
 1716 between these test beam periods, when the beam is not available, the chambers are irradiated by the
 1717 ^{137}Cs in order to accumulate deposited charge and the gamma background is measured.

1718 RPCs under test are connected through LVDS cables to V1190A Time-to-Digital Converter
 1719 (TDC) modules manufactured by CAEN. These modules, located in the rack area outside of the
 1720 bunker, get the logic signals sent by the chambers and save them into their buffers. Due to the
 1721 limited size of the buffers, the collected data is regularly erased and replaced. A trigger signal is
 1722 needed for the TDC modules to send the useful data to the DAQ computer via a V1718 CAEN USB
 1723 communication module.

1724 In the case of performance test, the trigger signal used for data acquisition is generated by the
 1725 coincidence of three scintillators. A first one is placed upstream outside of the bunker, a second one
 1726 is placed downstream outside of the bunker, while a third one is placed in front of the trolley, close by
 1727 the chambers. Every time a trigger is sent to the TDCs, i.e. every time a muon is detected, knowing
 1728 the time delay in between the trigger and the RPC signals, signals located in the right time window
 1729 are extracted from the buffers and saved for later analysis. Signals are taken in a time window of
 1730 400 ns centered on the muon peak (here we could show a time spectrum). On the other hand, in the
 1731 case of background rate measurement, the trigger signal needs to be "random" not to measure muons
 1732 but to look at gamma background. A trigger pulse is continuously generated at a rate of 300 Hz using
 1733 a dual timer. To integrate an as great as possible time, all signals contained within a time window of
 1734 10us prior to the random trigger signal are extracted form the buffers and saved for further analysis
 1735 (here another time spectrum to illustrate could be useful, maybe even place both spectrum together
 1736 as a single Figure).

1737 The signals sent to the TDCs correspond to hit collections in the RPCs. When a particle hits
 1738 a RPC, it induce a signal in the pickup strips of the RPC readout. If this signal is higher than the
 1739 detection threshold, a LVDS signal is sent to the TDCs. The data is then organised into 4 branches
 1740 keeping track of the event number, the hit multiplicity for the whole setup, and the time and channel
 1741 profile of the hits in the TDCs.

1742 **4.4.2 RPC current, environmental and operation parameter monitoring**

1743 In order to take into account the variation of pressure and temperature between different data taking
 1744 periods the applied voltage is corrected following the relationship :

$$1745 \quad HV_{eff} = HV_{app} \times \left(0.2 + 0.8 \cdot \frac{P_0}{P} \times \frac{T}{T_0} \right) \quad (4.10)$$

¹⁷⁴⁵ where T_0 (=293 K) and P_0 (=990 mbar) are the reference values.

¹⁷⁴⁶ **4.4.3 Measurement procedure**

¹⁷⁴⁷ Insert a short description of the online tools (DAQ, DCS, DQM).

¹⁷⁴⁸ Insert a short description of the offline tools : tracking and efficiency algorithm.

¹⁷⁴⁹ Identify long term aging effects we are monitoring the rates per strip.

¹⁷⁵⁰ **4.4.4 Longevity studies results**

5

1751

1752

Investigation on high rate RPCs

1753 **5.1 Rate limitations and ageing of RPCs**

1754 **5.1.1 Low resistivity electrodes**

1755 **5.1.2 Low noise front-end electronics**

1756 **5.2 Construction of prototypes**

1757 **5.3 Results and discussions**

6

1758

1759

Conclusions and outlooks

1760 **6.1 Conclusions**

1761 **6.2 Outlooks**

A

1762

1763

A data acquisition software for CAEN VME TDCs

1764

1765 Certifying detectors in the perspective of HL-LHC required to develop tools for the GIF++ expe-
1766 riment. Among them was the C++ Data Acquisition (DAQ) software that allows to make the com-
1767 munications in between a computer and TDC modules in order to retrieve the RPC data [57]. In this
1768 appendix, details about this software, as of how the software was written, how it functions and how
1769 it can be exported to another similar setup, will be given.

1770 A.1 GIF++ DAQ file tree

1771 GIF++ DAQ source code is fully available on github at [https://github.com/afagot/GIF_](https://github.com/afagot/GIF_DAQ)
1772 DAQ. The software requires 3 non-optional dependencies:

- 1773 • CAEN USB Driver, to mount the VME hardware,
1774 • CAEN VME Library, to communicate with the VME hardware, and
1775 • ROOT, to organize the collected data into a TTree.

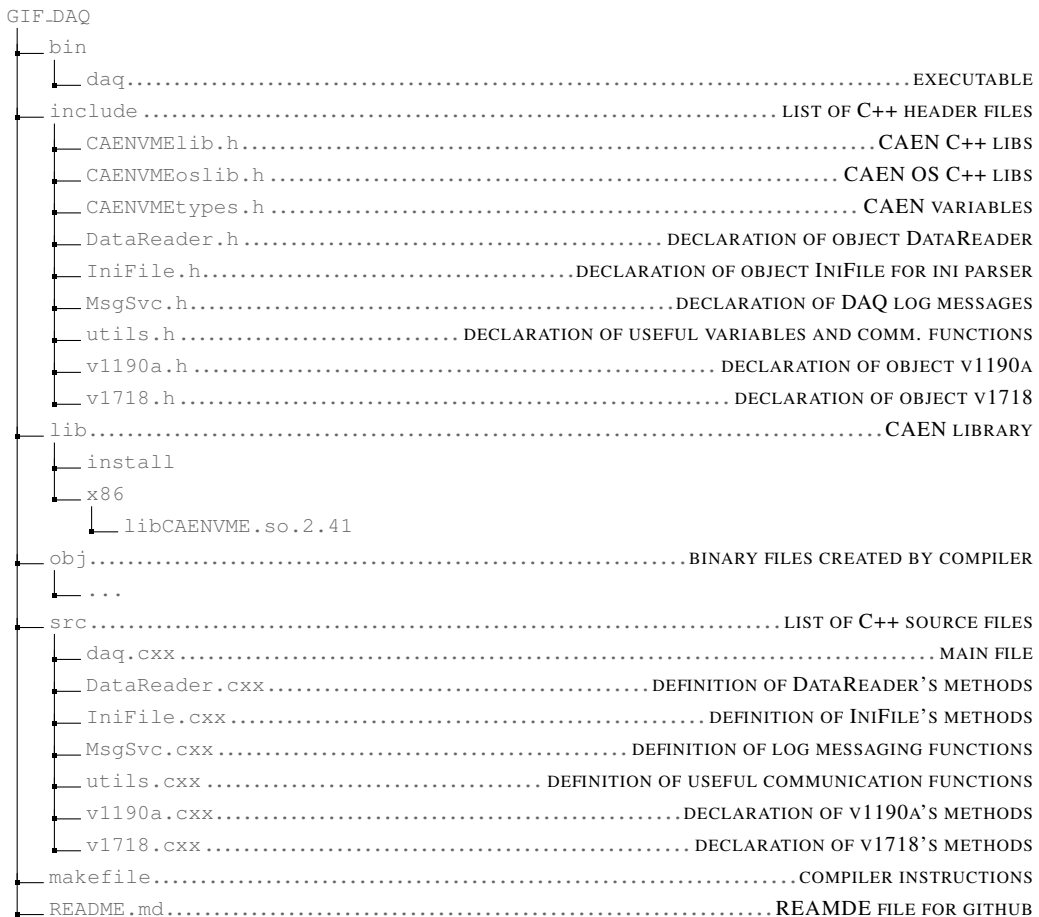
1776 The CAEN VME library will not be packaged by distributions and will need to be installed man-
1777 ually. To compile the GIF++ DAQ project via a terminal, from the DAQ folder use the command:

1778

1779 `make`

1780 The source code tree is provided below along with comments to give an overview of the files' con-
1781 tent. The different objects created for this project (`v1718`, `v1190a`, `IniFile` & `DataReader`) will be
1782 described in details in the following sections.

1783



1784 A.2 Usage of the DAQ

1785 GIF++ DAQ, as used in GIF++, is not a standalone software. Indeed, the system being more complexe,
 1786 the DAQ only is a sub-layer of the software architecture developped to control and monitor
 1787 the RPCs that are placed into the bunker for performance study in an irradiated environment. The top
 1788 layer of GIF++ is a Web Detector Control System (webDCS) application. The DAQ is only called
 1789 by the webDCS when data needs to be acquired. The webDCS operates the DAQ through command
 1790 line. To start the DAQ, the webDCS calls:

1791

1792 bin/daq /path/to/the/log/file/in/the/output/data/folder

1793 where /path/to/the/log/file/in/the/output/data/folder is the only argument required. This
 1794 log file is important for the webDCS as this file contains all the content of the communication of the
 1795 webDCS and the different systems monitored by the webDCS. Its content is constantly displayed
 1796 during data taking for the users to be able to follow the operations. The communication messages
 1797 are normally sent to the webDCS log file via the functions declared in file MsgSvc.h, typically
 1798 MSG_INFO(string message).

1799

1800 A.3 Description of the readout setup

1801 The CMS RPC setup at GIF++ counts 5 V1190A Time-to-Digital Converter (TDC) manufactured
 1802 by CAEN [58]. V1190A are VME units accepting 128 independent Multi-Hit/Multi-Event TDC
 1803 channels whose signals are treated by 4 100 ps high performance TDC chips developed by CERN
 1804 / ECP-MIC Division. The communication between the computer and the TDCs to transfer data is
 1805 done via a V1718 VME master module also manufactured by CAEN and operated from a USB
 1806 port [59]. These VME modules are all hosted into a 6U VME 6021 powered crate manufactured by
 1807 W-Ie-Ne-R than can accommodate up to 21 VME bus cards [60]. These 3 components of the DAQ
 1808 setup are shown in Figure A.1.

1809

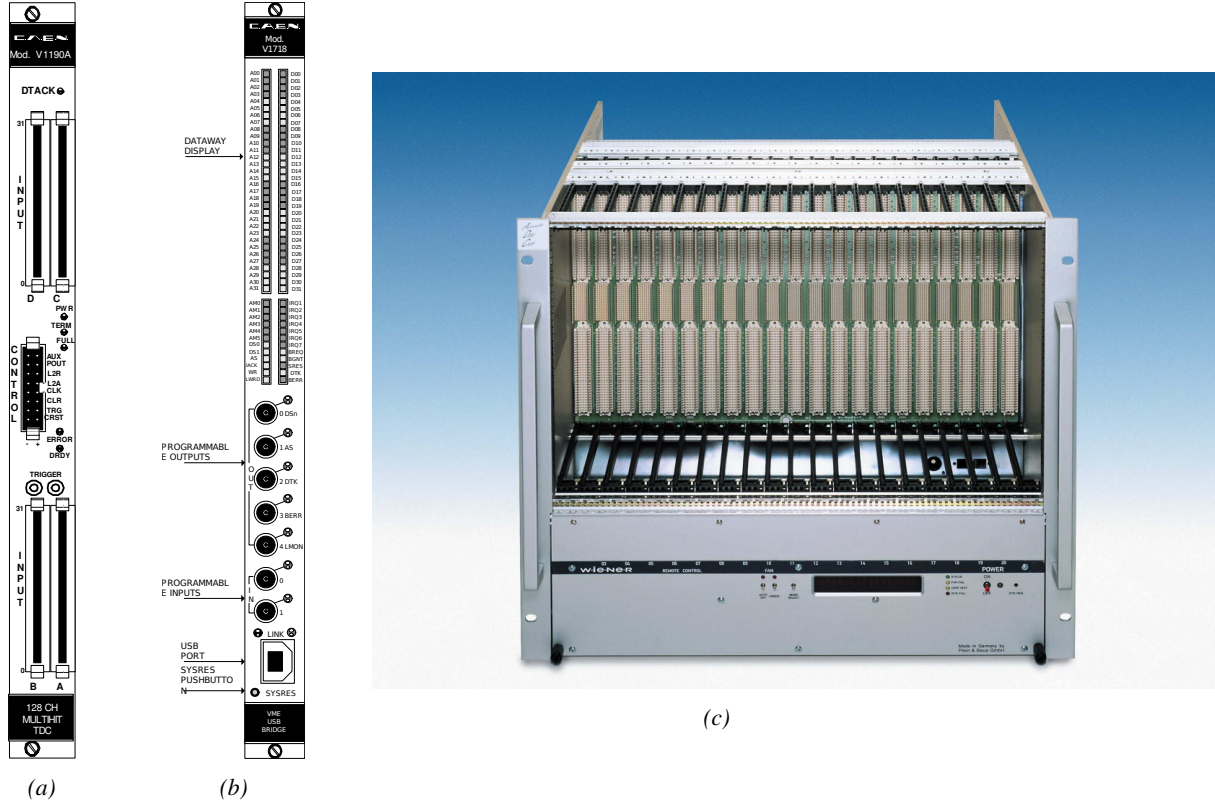


Figure A.1: (A.1a) View of the front panel of a V1190A TDC module [58]. (A.1b) View of the front panel of a V1718 Bridge module [59]. (A.1c) View of the front panel of a 6U 6021 VME crate [60].

1810 A.4 Data read-out

1811 To efficiently perform a data readout algorithm, C++ objects to handle the VME modules (TDCs
 1812 and VME bridge) have been created along with objects to store data and read the configuration file

1813 that comes as an input of the DAQ software.

1814

1815 A.4.1 V1190A TDCs

1816 The DAQ used at GIF takes profit of the *Trigger Matching Mode* offered by V1190A modules.
 1817 This setting is enabled through the method `v1190a::SetTrigMatching (int ntdcs)` where `ntdcs`
 1818 is the total number of TDCs in the setup this setting needs to be enabled for (Source Code A.1). A
 1819 trigger matching is performed in between a trigger time tag, a trigger signal sent into the TRIGGER
 1820 input of the TDC visible on Figure A.1a, and the channel time measurements, signals recorded from
 1821 the detectors under test in our case. Control over this data acquisition mode, explained through
 1822 Figure A.2, is offered via 4 programmable parameters:

- 1823 • **match window:** the matching between a trigger and a hit is done within a programmable time
 1824 window. This is set via the method

1825 `void v1190a::SetTrigWindowWidth(Uint windowHeight, int ntdcs)`

- 1826 • **window offset:** temporal distance between the trigger tag and the start of the trigger matching
 1827 window. This is set via the method

1828 `void v1190a::SetTrigWindowWidth(Uint windowHeight, int ntdcs)`

- 1829 • **extra search margin:** an extended time window is used to ensure that all matching hits are
 1830 found. This is set via the method

1831 `void v1190a::SetTrigSearchMargin(Uint searchMargin, int ntdcs)`

- 1832 • **reject margin:** older hits are automatically rejected to prevent buffer overflows and to speed
 1833 up the search time. This is set via the method

1834 `void v1190a::SetTrigRejectionMargin(Uint rejectMargin, int ntdcs)`

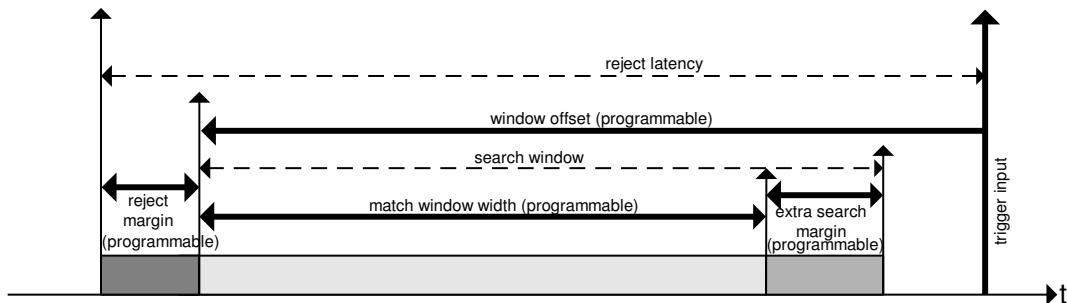


Figure A.2: Module V1190A Trigger Matching Mode timing diagram [58].

1835 Each of these 4 parameters are given in number of clocks, 1 clock being 25 ns long. It is easy to
 1836 understand at this level that there are 3 possible functioning settings:

- 1837 • **1:** the match window is entirely contained after the trigger signal,

- 1838 • **2:** the match window overlaps the trigger signal, or

- 1839 • **3:** the match window is entirely contained before the trigger signal as displayed on Figure A.2.

1840 In both the first and second cases, the sum of the window width and of the offset can be set to
1841 a maximum of 40 clocks, which corresponds to 1 μ s. Evidently, the offset can be negative, allowing
1842 for a longer match window, with the constraint of having the window ending at most 1 μ s after the
1843 trigger signal. In the third case, the maximum negative offset allowed is of 2048 clocks (12 bit) cor-
1844 responding to 51.2 μ s, the match window being strictly smaller than the offset. In the case of GIF++,
1845 the choice has been made to use this last setting by delaying the trigger signal. During the studies
1846 performed in GIF++, both the efficiency of the RPCs, probed using a muon beam, and the noise or
1847 gamma background rate are monitored. The extra search and reject margins are left unused.
1848 To probe the efficiency of RPC detectors, the trigger time tag is provided by the coïncidence of
1849 scintillators when a bunch of muons passes through GIF++ area is used to trigger the data acquisi-
1850 tion. For this measurement, it is useful to reduce the match window width only to contain the muon
1851 information. Indeed, the delay in between a trigger signal and the detection of the corresponding
1852 muon in the RPC being very contant (typically a few tens of ns due to jitter and cable length), the
1853 muon signals are very localised in time. Thus, due to a delay of approximalety 325 ns in between
1854 the muons and the trigger, the settings where chosen to have a window width of 24 clocks (600 ns)
1855 centered on the muon peak thanks to a negative offset of 29 clocks (725 ns).
1856 On the otherhand, monitoring the rates don't require for the DAQ to look at a specific time window.
1857 It is important to integrate enough time to have a robust measurement of the rate as the number of
1858 hits per time unit. The triggerring signal is provided by a pulse generator at a frequency of 300 Hz
1859 to ensure that the data taking occurs in a random way, with respect to beam physics, to probe only
1860 the irradiation spectrum on the detectors. The match window is set to 400 clocks (10 μ s) and the
1861 negative offset to 401 clocks as it needs to exceed the value of the match window.

```

1862
class v1190a
{
    private :
        long             Handle;
        vector<Data32>   Address;
        CVDataWidth      DataWidth;
        CVAddressModifier AddressModifier;

    public:

        v1190a(long handle, IniFile *inifile, int ntdcs);
        ~v1190a();
        Data16 write_op_reg(Data32 address, int code, string error);
        Data16 read_op_reg(Data32 address, string error);
        void Reset(int ntdcs);
        void Clear(int ntdcs);
        void TestWR(Data16 value,int ntdcs);
        void CheckTDCStatus(int ntdcs);
        void CheckCommunication(int ntdcs);
        void SetTDCTestMode(Data16 mode,int ntdcs);
        void SetTrigMatching(int ntdcs);
        void SetTrigTimeSubtraction(Data16 mode,int ntdcs);
        void SetTrigWindowWidth(Uint windowHeight,int ntdcs);
        void SetTrigWindowOffset(Uint windowOffset,int ntdcs);
        void SetTrigSearchMargin(Uint searchMargin,int ntdcs);
        void SetTrigRejectionMargin(Uint rejectMargin,int ntdcs);
        void GetTrigConfiguration(int ntdcs);
        void SetTrigConfiguration(IniFile *inifile,int ntdcs);
        void SetTDCDetectionMode(Data16 mode,int ntdcs);
        void SetTDCResolution(Data16 lsb,int ntdcs);
        void SetTDCDeadTime(Data16 time,int ntdcs);
        void SetTDCHeadTrailer(Data16 mode,int ntdcs);
        void SetTDCEventSize(Data16 size,int ntdcs);
        void SwitchChannels(IniFile *inifile,int ntdcs);
        void SetIRQ(Data32 level, Data32 count,int ntdcs);
        void SetBlockTransferMode(Data16 mode,int ntdcs);
        void Set(IniFile *inifile,int ntdcs);
        void CheckStatus(CVErrorCodes status) const;
        int ReadBlockD32(Uint tdc, const Data16 address,
                         Data32 *data, const Uint words, bool ignore_berr);
        Uint Read(RAWData *DataList,int ntdcs);
};

1863

```

1864 *Source Code A.1: Description of C++ object v1190a.*

1865 The v1190a object, defined in the DAQ software as in Source Code A.1, offers the possibility to
 1866 concatenate all TDCs in the readout setup into a single object containing a list of hardware addresses
 1867 (addresses to access the TDCs' buffer through the VME crate) and each constructor and method acts
 1868 on the list of TDCs.

1869

1870 A.4.2 DataReader

1871 Enabled thanks to v1190a::SetBlockTransferMode(Data16 mode, int ntdcs), the data transfer
 1872 is done via Block Transfer (BLT). Using BLT allows to tranfer a fixed number of events called a
 1873 *block*. This is used together with an Almost Full Level (AFL) of the TDCs' output buffers, defined

1874 through `v1190a::SetIRQ(Data32 level, Data32 count, int ntdcs)`. This AFL gives the maximum amount of 32735 words (16 bits, corresponding to the depth of a TDC output buffer) that can
 1875 written in a buffer before an Interrupt Request (IRQ) is generated and seen by the VME Bridge,
 1876 stopping the data acquisition to transfer the content of each TDC buffers before resuming. For each
 1877 trigger, 6 words or more are written into the TDC buffer:

- 1879 • a **global header** providing information of the event number since the beginning of the data
 acquisition,
- 1881 • a **TDC header**,
- 1882 • the **TDC data** (*if any*), 1 for each hit recorded during the event, providing the channel and the
 time stamp associated to the hit,
- 1884 • a **TDC error** providing error flags,
- 1885 • a **TDC trailer**,
- 1886 • a **global trigger time tag** that provides the absolute trigger time relatively to the last reset,
 and
- 1888 • a **global trailer** providing the total word count in the event.

1889 As previously described in Section ??, CMS RPC FEEs provide us with 100 ns long LVDS out-
 1890 put signals that are injected into the TDCs' input. Any avalanche signal that gives a signal above the
 1891 FEEs threshold is thus recorded by the TDCs as a hit within the match window. Each hit is assigned
 1892 to a specific TDC channel with a time stamp, with a precision of 100 ps. The reference time, $t_0 = 0$,
 1893 is provided by the beginning of the match window. Thus for each trigger, coming from a scintillator
 1894 coincidence or the pulse generator, a list of hits is stored into the TDCs' buffers and will then be
 1895 transferred into a ROOT Tree.

1896 When the BLT is used, it is easy to understand that the maximum number of words that have
 1897 been set as ALF will not be a finite number of events or, at least, the number of events that would
 1898 be recorded into the TDC buffers will not be a multiple of the block size. In the last BLT cycle to
 1899 transfer data, the number of events to transfer will most probably be lower than the block size. In that
 1900 case, the TDC can add fillers at the end of the block but this option requires to send more data to the
 1901 computer and is thus a little slower. Another solution is to finish the transfer after the last event by
 1902 sending a bus error that states that the BLT reached the last event in the pile. This method has been
 1903 chosen in GIF++.

1905 Due to irradiation, an event in GIF++ can count up to 300 words per TDC. A limit of 4096 words
 1906 (12 bits) has been set to generate IRQ which represent from 14 to almost 700 events depending on
 1907 the average of hits collected per event. Then the block size has been set to 100 events with enabled
 1908 bus errors. When an AFL is reached for one of the TDCs, the VME bridge stops the acquisition by
 1909 sending a BUSY signal.

1911

1912 The data is then transferred one TDC at a time into a structure called `RAWData` (Source Code A.2).

```
1913
struct RAWData{
    vector<int>           *EventList;
    vector<int>           *NHitsList;
    vector<int>           *QFlagList;
    vector<vector<int> >   *Channellist;
    vector<vector<float> > *TimeStampList;
};

1915
```

Source Code A.2: Description of data holding C++ structure `RAWData`.

1916 In order to organize the data transfer and the data storage, an object called `DataReader` was
 1917 created (Source Code A.3). On one hand, it has `v1718` and `v1190a` objects as private members for
 1918 communication purposes, such as VME modules settings via the configuration file `*iniFile` or data
 1919 read-out through `v1190a::Read()` and on the other hand, it contains the structure `RAWData` that allows
 1920 to organise the data in vectors reproducing the tree structure of a ROOT file.

```
1921
class DataReader
{
    private:
        bool      StopFlag;
        IniFile  *iniFile;
        Data32   MaxTriggers;
        v1718   *VME;
        int       nTDCs;
        v1190a  *TDCs;
        RAWData  TDCData;

    public:
        DataReader();
        virtual ~DataReader();
        void     SetIniFile(string inifilename);
        void     SetMaxTriggers();
        Data32   GetMaxTriggers();
        void     SetVME();
        void     SetTDC();
        int      GetQFlag(Uint it);
        void     Init(string inifilename);
        void     FlushBuffer();
        void     Update();
        string   GetFileName();
        void     WriteRunRegistry(string filename);
        void     Run();
};

1923
```

Source Code A.3: Description of C++ object `DataReader`.

1924 Each event is transferred from `TDCData` and saved into branches of a ROOT `TTree` as 3 integers
 1925 that represent the event ID (`EventCount`), the number of hits read from the TDCs (`nHits`), and the
 1926 quality flag that provides information for any problem in the data transfer (`qflag`), and 2 lists of
 1927 `nHits` elements containing the fired TDC channels (`TDCCh`) and their respective time stamps (`TDCTS`),
 1928 as presented in Source Code A.4. The ROOT file file is named using information contained into
 1929 the configuration file, presented in section A.5.2. The needed information is extracted using method
 1930 `DataReader::GetFileName()` and allow to build the output filename format `ScanXXXXXX_HVX_DAQ.root`

1931 where ScanXXXXXX is a 6 digit number representing the scan number into GIFT++ database and HVX
 1932 the HV step within the scan that can be more than a single digit. An example of ROOT data file is
 1933 provided with Figure A.3.

```
1934
1935     RAWData TDCData;
TFile *outputFile = new TFile(outputFileName.c_str(),"recreate");
TTree *RAWDataTree = new TTree("RAWData","RAWData");

int          EventCount = -9;
int          nHits = -8;
int          qflag = -7;
vector<int>   TDCCh;
vector<float> TDCTS;

RAWDataTree->Branch("EventNumber",&EventCount, "EventNumber/I");
RAWDataTree->Branch("number_of_hits",&nHits,"number_of_hits/I");
RAWDataTree->Branch("Quality_flag",&qflag,"Quality_flag/I");
RAWDataTree->Branch("TDC_channel",&TDCCh);
RAWDataTree->Branch("TDC_TimeStamp",&TDCTS);

//...
//Here read the TDC data using v1190a::Read() and place it into
//TDCData for as long as you didn't collect the requested amount
//of data.
//...

for(Uint i=0; i<TDCData.EventList->size(); i++){
    EventCount = TDCData.EventList->at(i);
    nHits      = TDCData.NHitsList->at(i);
    qflag      = TDCData.QFlagList->at(i);
    TDCCh     = TDCData.ChannelList->at(i);
    TDCTS     = TDCData.TimeStampList->at(i);
    RAWDataTree->Fill();
}
```

1936 *Source Code A.4: Highlight of the data transfer and organisation within DataReader::Run() after the data has been collected into TDCData.*

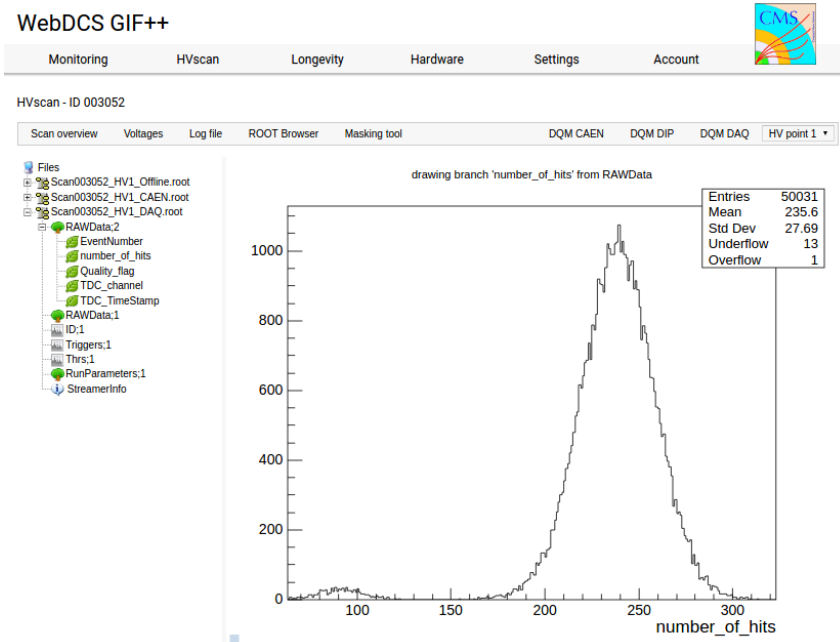


Figure A.3: Structure of the ROOT output file generated by the DAQ. The 5 branches (EventNumber, number_of_hits, Quality_flag, TDC_channel and TDC_TimeStamp) are visible on the left panel of the ROOT browser. On the right panel is visible the histogram corresponding to the variable nHits. In this specific example, there were approximately 50k events recorded to measure the gamma irradiation rate on the detectors. Each event is stored as a single entry in the TTree.

A.4.3 Data quality flag

1938 Among the parameters that are recorded for each event, the quality flag, defined in Source Code A.5,
 1939 is determined on the fly by checking the data recorded by every single TDC. From method `v1190a::Read()`,
 1940 it can be understood that the content of each TDC buffer is readout one TDC at a time. Entries are
 1941 created in the data list for the first TDC and then, when the second buffer is readout, events corre-
 1942 sponding to entries that have already been created to store data for the previous TDC are added to
 1943 the existing list element. On the contrary, when an event entry has not been yet created in the data
 1944 list, a new entry is created.

```
1945
typedef enum _QualityFlag {
 1946   GOOD      = 1,
   CORRUPTED = 0
} QualityFlag;
```

1947 *Source Code A.5: Definition of the quality flag `enum`.*

1948 It is possible that each TDC buffer contains a different number of events. In cases where the first
 1949 element in the buffer list is an event for corresponds to a new entry, the difference in between the
 1950 entry from the buffer and the last entry in the data list is recorded and checked. If it is greater than 1,
 1951 what should never be the case, the quality flag is set to CORRUPTED for this TDC and an empty entry
 1952 is created in the place of the missing ones. Missing entries are believe to be the result of a bad hold

1953 on the TDC buffers at the moment of the readout. Indeed, the software hold is effective only on 1
 1954 TDC at a time and no solution as been found yet to completely block the writting in the buffers when
 1955 an IRQ is received.

1956 At the end of each BLT cycle, the ID of the last entry stored for each TDC buffer is not recorded.
 1957 When starting the next cycle, if the first entry in the pile corresponds to an event already existing
 1958 in the list, the readout will start from this list element and will not be able to check the difference
 1959 in between this entry's ID and the one of the last entry that was recorded for this TDC buffer in
 1960 the previous cycle. In the case events were missing, the flag stays at its initial value of 0, which is
 1961 similar to CORRUPTED and it is assumed that then this TDC will not contribute to `number_of_hits`,
 1962 `TDC_channel` or `TDC_TimeStamp`.

1963 Finally, since there will be 1 `RAWData` entry per TDC for each event (meaning `nTDCs` entries,
 1964 referring to `DataReader` private attribute), the individual flags of each TDC will be added together.
 1965 The final format is an integer composed `nTDCs` digits where each digit is the flag of a specific TDC.
 1966 This is constructed using powers of 10 like follows:

```
1967 TDC 0: QFlag = 100 × _QualityFlag
1968 TDC 1: QFlag = 101 × _QualityFlag
1969 ...
1970 TDC N: QFlag = 10N × _QualityFlag
```

1971 and the final flag to be with N digits:

1972 `QFlag = n....3210`

1973 each digit being 1 or 0. Below is given an example with a 4 TDCs setup.

1974 If all TDCs were good : `QFlag = 1111`,

1975 but if TDC 2 was corrupted : `QFlag = 1011`.

1976 When data taking is over and the data contained in the dynamical `RAWData` structure is transferred
 1977 to the ROOT file, all the 0s are changed into 2s by calling the method `DataReader::GetQFlag()`.
 1978 This will help translating the flag without knowing the number of TDCs beforehand. Indeed, a flag
 1979 111 could be due to a 3 TDC setup with 3 good individual TDC flags or to a more than 3 TDC setup
 1980 with TDCs those ID is greater than 2 being CORRUPTED, thus giving a 0.

1981 The quality flag has been introduced quite late, in October 2017 only, to the list of GIFT++ DAQ
 1982 parameters to be recorded into the output ROOT file. Before this addition, the missing data, corrupting
 1983 the quality for the offline analysis, was contributing to artificially fill data with lower multiplicity.
 1984 Looking at `TBranch number_of_hits` provides an information about the data of the full GIFT++
 1985 setup. When a TDC is not able to transfer data for a specific event, the effect is a reduction of the
 1986 total number of hits recorded in the full setup, this is what can be seen from Figure A.4. After offline
 1987 reconstruction detector by detector, the effect of missing events can be seen in the artificially filled
 1988 bin at multiplicity 0 shown in Figure A.5. Nonetheless, for data with high irradiation levels, as it is
 1989 the case for Figure A.5a, discarding the fake multiplicity 0 data can be done easily during the offline
 1990 analysis. At lower radiation, the missing events contribution becomes more problematic as the multi-
 1991 tiplicity distribution overlaps the multiplicity 0 and that in the same time the proportion of missing

events decreases. Attempts to fit the distribution with a Poisson or skew distribution function were not conclusive and this very problem has been at the origin of the quality flag that allows to give a non ambiguous information about each event quality.

1995

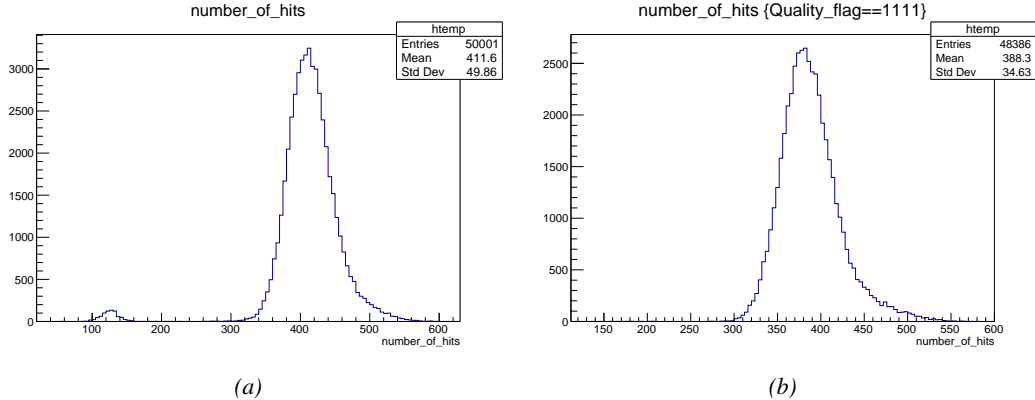


Figure A.4: The effect of the quality flag is explained by presenting the content of TBranch `number_of_hits` of a data file without `Quality_flag` in Figure A.4a and the content of the same TBranch for data corresponding to a `Quality_flag` where all TDCs were labelled as `GOOD` in Figure A.4b taken with similar conditions. It can be noted that the number of entries in Figure A.4b is slightly lower than in Figure A.4a due to the excluded events.

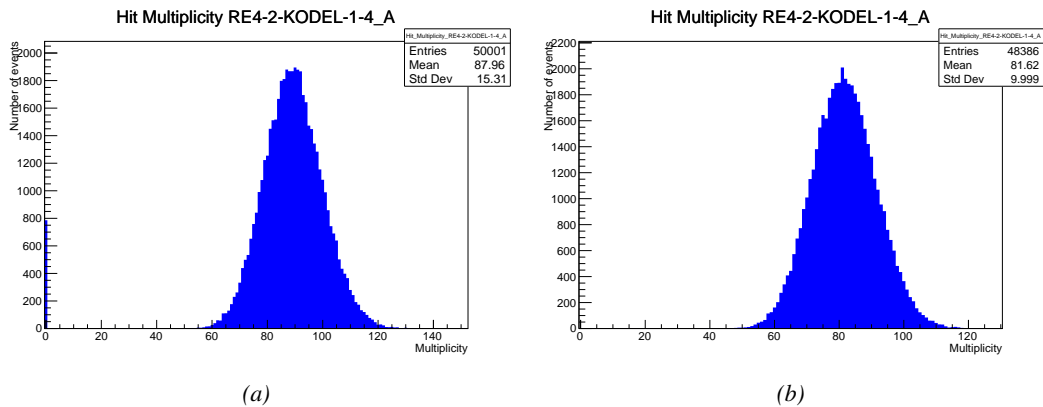


Figure A.5: Using the same data as previously showed in Figure A.4, the effect of the quality flag is explained by presenting the reconstructed hit multiplicity of a data file without `Quality_flag` in Figure A.5a and the reconstructed content of the same RPC partition for data corresponding to a `Quality_flag` where all TDCs were labelled as `GOOD` in Figure A.5b taken with similar conditions. The artificial high content of bin 0 is completely suppressed.

A.5 Communications

To ensure data readout and dialog in between the machine and the TDCs or in between the webDCS and the DAQ, different communication solutions were used. First of all, it is important to have a

1997
1998

1999 module to allow the communication in between the TDCs and the computer from which the DAQ
 2000 operates. When this communication is effective, shifters using the webDCS to control data taking
 2001 can thus send instructions to the DAQ.

2002

2003 A.5.1 V1718 USB Bridge

2004 In the previous section, the data transfer has been discussed. The importance of the `v1718` object
 2005 (Source Code A.6), used as private member of `DataReader`, was not explicated. VME master
 2006 modules are used for communication purposes as they host the USB port that connects the pow-
 2007 ered crate buffer to the computer where the DAQ is installed. From the source code point of view,
 2008 this object is used to control the communication status, by reading the returned error codes with
 2009 `v1718::CheckStatus()`, or to check for IRQs coming from the TDCs through `v1718::CheckIRQ()`.
 2010 Finally, to ensure that triggers are blocked at the hardware level, a NIM pulse is sent out of one of the
 2011 5 programmable outputs (`v1718::SendBUSY()`) to the VETO of the coincidence module where the
 2012 trigger signals originate from. As long as this signal is ON, no trigger can reach the TDCs anymore.
 2013

```
2014 class v1718{
    private:
        int Handle;
        Data32 Data;           // Data
        CVIRQLevels Level;    // Interrupt level
        CVAddressModifier AM;  // Addressing Mode
        CVDataWidth dataSize; // Data Format
        Data32 BaseAddress;   // Base Address

    public:
        v1718(IniFile *inifile);
        ~v1718();
        long GetHandle(void) const;
        int SetData(Data16 data);
        Data16 GetData(void);
        int SetLevel(CVIRQLevels level);
        CVIRQLevels GetLevel(void);
        int SetAM(CVAddressModifier am);
        CVAddressModifier GetAM(void);
        int SetDatasize(CVDataWidth datasize);
        CVDataWidth GetDataSize(void);
        int SetBaseAddress(Data16 baseaddress);
        Data16 GetBaseAddress(void);
        void CheckStatus(CVErrorCodes status) const;
        void CheckIRQ();
        void SetPulsers();
        void SendBUSY(BusyLevel level);
};
```

2015 *Source Code A.6: Description of C++ object v1718.*

2016 A.5.2 Configuration file

2017 The DAQ software takes as input a configuration file written using INI standard [61]. This file is
 2018 partly filled with the information provided by the shifters when starting data acquisition using the
 2019 webDCS, as shown by Figure A.6. This information is written in section [`General`] and will later

2020 be stored in the ROOT file that contains the DAQ data as can be seen from Figure A.3. Indeed,
 2021 another `TTree` called `RunParameters` as well as the 2 histograms `ID`, containing the scan number,
 2022 start and stop time stamps, and `Triggers`, containing the number of triggers requested by the shifter,
 2023 are available in the data files. Moreover, `ScanID` and `HV` are then used to construct the file name
 2024 thanks to the method `DataReader::GetFileName()`.

WebDCS GIF++

Chamber	RE2-2-NPD-BARC-8	RE4-2-CERN-106	RE2-3-NPD-BARC-9	RE4-2-CERN-105	RE4-2-KODEL-1-4	Max triggers
HV _{eff} 1	8600	8500	8600	8500	6500	
HV _{eff} 2	8700	8600	8700	8600	6600	
HV _{eff} 3	8800	8700	8800	8700	6700	
HV _{eff} 4	8900	8800	8900	8800	6800	
HV _{eff} 5	9000	8900	9000	8900	6900	
HV _{eff} 6	9100	9000	9100	9000	7000	
HV _{eff} 7	9200	9100	9200	9100	7100	
HV _{eff} 8	9300	9200	9300	9200	7200	
HV _{eff} 9	9400	9300	9400	9300	7300	
HV _{eff} 10	9500	9400	9500	9400	7400	

Start HV scan

Figure A.6: WebDCS DAQ scan page. On this page, shifters need to choose the type of scan (Rate, Efficiency or Noise Reference scan), the gamma source configuration at the moment of data taking, the beam configuration, and the trigger mode. These information will be stored in the DAQ ROOT output. Are also given the minimal measurement time and waiting time after ramping up of the detectors is over before starting the data acquisition. Then, the list of HV points to scan and the number of triggers for each run of the scan are given in the table underneath.

2025 The rest of the information is written beforehand in the configuration file template, as explicated
 2026 in Source Code A.7, and contains the hardware addresses to the different VME modules in the
 2027 setup as well as settings for the TDCs. As the TDC settings available in the configuration file are not
 2028 supposed to be modified, an improvement would be to remove them from the configuration file and
 2029 to hardcode them inside of the DAQ code itself or to place them into a different INI file that would
 2030 host only the TDC settings to lower the probability for a bad manipulation of the configuration file
 2031 that can be modified from one of webDCS' menus.

2032

```
[General]
TdcS=4
ScanID=$scanid
HV=$HV
RunType=$runtype
MaxTriggers=$maxtriggers
Beam=$beam
[VMEInterface]
Type=V1718
BaseAddress=0xFF0000
Name=VmeInterface
[TDC0]
Type=V1190A
BaseAddress=0x00000000
Name=Tdc0
StatusA00-15=1
StatusA16-31=1
StatusB00-15=1
StatusB16-31=1
StatusC00-15=1
StatusC16-31=1
StatusD00-15=1
StatusD16-31=1
[TDC1]
Type=V1190A
BaseAddress=0x11110000
Name=Tdc1
StatusA00-15=1
StatusA16-31=1
StatusB00-15=1
StatusB16-31=1
StatusC00-15=1
StatusC16-31=1
StatusD00-15=1
StatusD16-31=1
[TDC2]
Type=V1190A
BaseAddress=0x22220000
Name=Tdc2
StatusA00-15=1
StatusA16-31=1
StatusB00-15=1
StatusB16-31=1
StatusC00-15=1
StatusC16-31=1
StatusD00-15=1
StatusD16-31=1
[TDC3]
Type=V1190A
BaseAddress=0x44440000
Name=Tdc3
StatusA00-15=1
StatusA16-31=1
StatusB00-15=1
StatusB16-31=1
StatusC00-15=1
StatusC16-31=1
StatusD00-15=1
StatusD16-31=1
[TDCSettings]
TriggerExtraSearchMargin=0
TriggerRejectMargin=0
TriggerTimeSubtraction=0b1
TdcDetectionMode=0b01
TdcResolution=0b10
TdcDeadTime=0b00
TdcHeadTrailer=0b1
TdcEventSize=0b1001
TdcTestMode=0b0
BLTMode=1
```

2033

Source Code A.7: INI configuration file template for 4 TDCs. In section [General], the number of TDCs is explicitated and information about the ongoing run is given. Then, there are sections for each and every VME modules. There buffer addresses are given and for the TDCs, the list of channels to enable is given. Finally, in section [TDCSettings], a part of the TDC settings are given.

2035 In order to retrieve the information of the configuration file, the object `IniFile` has been developed
 2036 to provide an INI parser, presented in Source Code A.8. It contains private methods returning a
 2037 boolean to check the type of line written in the file, whether a comment, a group header or a key line
 2038 (`IniFile::CheckIfComment()`, `IniFile::CheckIfGroup()` and `IniFile::CheckIfToken()`). The
 2039 key may sometimes be referred to as *token* in the source code. Moreover, the private element
 2040 `FileData` is a map of `const string` to `string` that allows to store the data contained inside the
 2041 configuration file via the public method `IniFile::GetFileData()` following the formatting (see
 2042 method `IniFile::Read()`):

```
2043
2044     string group, token, value;
      // Get the field values for the 3 strings.
      // Then concatenate group and token together as a single string
      // with a dot separation.
      token = group + "." + token;
      FileData[token] = value;
```

2045 More methods have been written to translate the different keys into the right variable format
 2046 when used by the DAQ. For example, to get a `float` value out of the configuration file data, knowing
 2047 the group and the key needed, the method `IniFile::floatType()` can be used. It takes 3 arguments
 2048 being the group name and key name (both `string`), and a default `float` value used as exception in
 2049 the case the expected combination of group and key cannot be found in the configuration file. This
 2050 default value is then used and the DAQ continues on working after sending an alert in the log file for
 2051 further debugging.

```

2052 typedef map< const string, string > IniFileData;
2053
class IniFile{
    private:
        bool          CheckIfComment (string line);
        bool          CheckIfGroup(string line, string& group);
        bool          CheckIfToken(string line, string& key, string& value);
        string         FileName;
        IniFileData   FileData;
        int           Error;

    public:
        IniFile();
        IniFile(string filename);
        virtual      ~IniFile();

        // Basic file operations
        void          SetFileName(string filename);
        int           Read();
        int           Write();
        IniFileData GetFileData();

        // Data readout methods
        Data32         addressType (string groupname, string keyname, Data32
→     defaultvalue);
        long          intType     (string groupname, string keyname, long
→     defaultvalue);
        long long    longType    (string groupname, string keyname, long long
→     defaultvalue );
        string         stringType  (string groupname, string keyname, string
→     defaultvalue );
        float         floatType   (string groupname, string keyname, float
→     defaultvalue );

        // Error methods
        string         GetErrorMsg();
    };

```

2054 *Source Code A.8: Description of C++ object `IniFile` used as a parser for INI file format.*

2055 A.5.3 WebDCS/DAQ intercommunication

2056 When shifters send instructions to the DAQ via the configuration file, it is the webDCS itself that
 2057 gives the start command to the DAQ and then the 2 softwares use inter-process communication
 2058 through file to synchronise themselves. This communication file is represented by the variable **const**
 2059 **string** __runstatuspath.

2060 On one side, the webDCS sends commands or status that are readout by the DAQ:

- 2061 ● INIT, status sent when launching a scan and read via function `CtrlRunStatus(...)`,
- 2062 ● START, command to start data taking and read via function `CheckSTART()`,
- 2063 ● STOP, command to stop data taking at the end of the scan and read via function `CheckSTOP()`,
 2064 and
- 2065 ● KILL, command to kill data taking sent by user and read via function `CheckKILL()`

2066 and on the other, the DAQ sends status that are controled by the webDCS:

- 2067 ● `DAQ_RDY`, sent with `SendDAQReady()` to signify that the DAQ is ready to receive commands
2068 from the webDCS,
- 2069 ● `RUNNING`, sent with `SendDAQRunning()` to signify that the DAQ is taking data,
- 2070 ● `DAQ_ERR`, sent with `SendDAQError()` to signify that the DAQ didn't receive the expected com-
2071 mand from the webDCS or that the launch command didn't have the right number of argu-
2072 ments,
- 2073 ● `RD_ERR`, sent when the DAQ wasn't able to read the communication file, and
- 2074 ● `WR_ERR`, sent when the DAQ wasn't able to write into the communication file.

2075 **A.5.4 Example of inter-process communication cycle**

2076 Under normal conditions, the webDCS and the DAQ processes exchange commands and status via
2077 the file hosted at the address `__runstatuspath`, as explained in subsection A.5.3. An example of
2078 cycle is given in Table A.1. In this example, the steps 3 to 5 are repeated as long as the webDCS tells
2079 the DAQ to take data. A data taking cycle is the equivalent as what is called a *Scan* in GIFT++ jargon,
2080 referring to a set a runs with several HV steps. Each repetition of steps 3 to 5 is then equivalent to a
2081 single *Run*.

2082

2083 At any moment during the data taking, for any reason, the shifter can decide that the data taking
2084 needs to be stopped before it reached the end of the scheduled cycle. Thus at any moment on the
2085 cycle, the content of the inter-process communication file will be changed to `KILL` and the DAQ will
2086 shut down right away. The DAQ checks for `KILL` signals every 5s after the TDCs configuration is
2087 over. So far, the function `CheckKILL()` has been used only inside of the data taking loop of method
2088 `DataReader::Run()` and thus, if the shifter decides to KILL the data taking during the TDC con-
2089 figuration phase or the HV ramping in between 2 HV steps, the DAQ will not be stopped smoothly
2090 and a *force kill* command will be sent to stop the DAQ process that is still awake on the computer.
2091 Improvements can be brought on this part of the software to make sure that the DAQ can safely
2092 shutdown at any moment.

2093

2094 **A.6 Software export**

2095 In section A.2 was discussed the fact that the DAQ as written in its last version is not a standalone
2096 software. It is possible to make it a standalone program that could be adapted to any VME setup
2097 using V1190A and V1718 modules by creating a GUI for the software or by printing the log mes-
2098 sages that are normally printed in the webDCS through the log file, directly into the terminal. This
2099 method was used by the DAQ up to version 3.0 moment where the webDCS was completed. Also, it
2100 is possible to check branches of DAQ v2.X to have example of communication through a terminal.

2101

2102 DAQ v2.X is nonetheless limited in it's possibilities and requires a lot of offline manual interven-
2103 tions from the users. Indeed, there is no communication of the software with the detectors' power
2104 supply system that would allow for a user a predefine a list of voltages to operate the detectors at

step	actions of webDCS	status of DAQ	<code>__runstatuspath</code>
1	launch DAQ ramp voltages ramping over wait for currents stabilization	readout of IniFile configuration of TDCs	INIT
2		configuration done send DAQ ready wait for START signal	DAQ_RDY
3	waiting time over send START		START
4	wait for run to end monitor DAQ run status	data taking ongoing check for KILL signal	RUNNING
5		run over send DAQ_RDY wait for next DCS signal	DAQ_RDY
6	ramp voltages ramping over wait for currents stabilization		DAQ_RDY
3	waiting time over send START		START
4	wait for run to end monitor DAQ run status	update IniFile information data taking ongoing check for KILL signal	RUNNING
5		run over send DAQ_RDY wait for next DCS signal	DAQ_RDY
7	send command STOP	DAQ shuts down	STOP

Table A.1: Inter-process communication cycles in between the webDCS and the DAQ through file string signals.

2105 and loop over to take data without any further manual intervention. In v2.X, the data is taken for a
2106 single detector setting and at the end of each run, the softwares asks the user if he intends on taking
2107 more runs. If so, the software invites the user to set the operating voltages accordingly to what is
2108 necessary and to manual update the configuration file in consequence. This working mode can be a
2109 very first approach before an evolution and has been successfully used by colleagues from different
2110 collaborations.

2111

2112 For a more robust operation, it is recommended to develop a GUI or a web application to inter-
2113 face the DAQ. Moreover, to limit the amount of manual interventions, and thus the probability to
2114 make mistakes, it is also recommended to add an extra feature into the DAQ by installing the HV
2115 Wrapper library provided by CAEN of which an example of use in a similar DAQ software devel-
2116 opped by a master student of UGent, and called TinyDAQ, is provided on UGent's github. Then, this
2117 HV Wrapper will help you communicating with and give instructions to a CAEN HV powered crate
2118 and can be added into the DAQ at the same level where the communication with the user was made
2119 in DAQ v2.X. In case you are using another kind of power system for your detectors, it is stringly
2120 adviced to use HV modules or crates that can be remotely controled via a using C++ libraries.

2121

B

2122

2123

Details on the offline analysis package

2124 The data collected in GIF++ thanks to the DAQ described in Appendix A is difficult to interpret by
2125 a human user that doesn't have a clear idea of the raw data architecture of the ROOT data files. In
2126 order to render the data human readable, a C++ offline analysis tool was designed to provide users
2127 with detector by detector histograms that give a clear overview of the parameters monitored during
2128 the data acquisition [62]. In this appendix, details about this software in the context of GIF++, as of
2129 how the software was written and how it functions will be given.

2130 **B.1 GIF++ Offline Analysis file tree**

2131 GIF++ Offline Analysis source code is fully available on github at https://github.com/aafagot/GIF_OfflineAnalysis. The software requires ROOT as non-optionnal dependency
2132 as it takes ROOT files in input and write an output ROOT file containing histograms. To compile the
2133 GIF++ Offline Analysis project is compiled with cmake. To compile, first a build/ directory must
2134 be created to compile from there:

```
2136     mkdir build  
2137     cd build  
2138     cmake ..  
2139     make  
2140     make install
```

2138 To clean the directory and create a new build directory, the bash script cleandir.sh can be used:

```
2139  
2140     ./cleandir.sh
```

2141 The source code tree is provided below along with comments to give an overview of the files' con-
2142 tent. The different objects created for this project (`Infrastructure`, `Trolley`, `RPC`, `Mapping`, `RPCHit`,
2143 `RPCCluster` and `Inifile`) will be described in details in the following sections.

2144

```

GIF_OfflineAnalysis
├── bin
│   └── offlineanalysis ..... EXECUTABLE
├── build..... CMAKE COMPILATION DIRECTORY
└── ...
    ├── include..... LIST OF C++ HEADER FILES
    │   ├── Cluster.h..... DECLARATION OF OBJECT RPCCLUSTER
    │   ├── Current.h..... DECLARATION OF GETCURRENT ANALYSIS MACRO
    │   ├── GIFTrolley.h..... DECLARATION OF OBJECT TROLLEY
    │   ├── Infrastructure.h..... DECLARATION OF OBJECT INFRASTRUCTURE
    │   ├── IniFile.h..... DECLARATION OF OBJECT INI FILE FORINI PARSER
    │   ├── Mapping.h..... DECLARATION OF OBJECT MAPPING
    │   ├── MsgSvc.h..... DECLARATION OF OFFLINE LOG MESSAGES
    │   ├── OfflineAnalysis.h..... DECLARATION OF DATA ANALYSIS MACRO
    │   ├── RPCTracker.h..... DECLARATION OF OBJECT RPC
    │   ├── RPCHit.h..... DECLARATION OF OBJECT RPCHIT
    │   ├── types.h..... DEFINITION OF USEFUL VARIABLE TYPES
    │   └── utils.h..... DECLARATION OF USEFUL FUNCTIONS
    ├── obj..... BINARY FILES CREATED BY COMPILER
    └── ...
        ├── src..... LIST OF C++ SOURCE FILES
        │   ├── Cluster.cc..... DEFINITION OF OBJECT RPCCLUSTER
        │   ├── Current.cc..... DEFINITION OF GETCURRENT ANALYSIS MACRO
        │   ├── GIFTrolley.cc..... DEFINITION OF OBJECT TROLLEY
        │   ├── Infrastructure.cc..... DEFINITION OF OBJECT INFRASTRUCTURE
        │   ├── IniFile.cc..... DEFINITION OF OBJECT INI FILE FORINI PARSER
        │   ├── main.cc..... MAIN FILE
        │   ├── Mapping.cc..... DEFINITION OF OBJECT MAPPING
        │   ├── MsgSvc.cc..... DECLARATION OF OFFLINE LOG MESSAGES
        │   ├── OfflineAnalysis.cc..... DECLARATION OF DATA ANALYSIS MACRO
        │   ├── RPCTracker.cc..... DECLARATION OF OBJECT RPC
        │   ├── RPCHit.cc..... DECLARATION OF OBJECT RPCHIT
        │   └── utils.cc..... DEFINITION OF USEFUL FUNCTIONS
        ├── cleandir.sh..... BASH SCRIPT TO CLEAN BUILD DIRECTORY
        ├── CMakeLists.txt..... SET OF INSTRUCTIONS FOR CMAKE
        ├── config.h.in..... DEFINITION OF VERSION NUMBER
        └── README.md..... README FILE FOR GITHUB

```

2145

B.2 Usage of the Offline Analysis

2146

In order to use the Offline Analysis tool, it is necessary to know the Scan number and the HV Step of the run that needs to be analysed. This information needs to be written in the following format:

2148

2149

```
Scan00XXXX_HVY
```

2150

where XXXX is the scan ID and Y is the high voltage step (in case of a high voltage scan, data will be taken for several HV steps). This format corresponds to the base name of data files in the database

2151

2152 of the GIF++ webDCS. Usually, the offline analysis tool is automatically called by the webDCS at
 2153 the end of data taking or by a user from the webDCS panel if an update of the tool was brought.
 2154 Nonetheless, an expert can locally launch the analysis for tests on the GIF++ computer, or a user can
 2155 get the code on its local machine from github and download data from the webDCS for its own anal-
 2156 ysis. To launch the code, the following command can be used from the `GIF_OfflineAnalysis` folder:

2157

```
2158 bin/offlineanalysis /path/to/Scan00XXXX_HVY
```

2159 where, `/path/to/Scan00XXXX_HVY` refers to the local data files. Then, the offline tool will by itself
 2160 take care of finding all available ROOT data files present in the folder, as listed below:

2161

- `Scan00XXXX_HVY_DAQ.root` containing the TDC data as described in Appendix ?? (events, hit
 2162 and timestamp lists), and
- `Scan00XXXX_HVY_CAEN.root` containing the CAEN mainframe data recorded by the monitor-
 2164 ing tool webDCS during data taking (HVs and currents of every HV channels). This file is
 2165 created independently of the DAQ.

2166

B.2.1 Output of the offline tool

2167

B.2.1.1 ROOT file

2168

The analysis gives in output ROOT datafiles that are saved into the data folder and called using the
 2169 naming convention `Scan00XXXX_HVY_Offline.root`. Inside those, a list of `TH1` histograms can be
 2170 found. Its size will vary as a function of the number of detectors in the setup as each set of histograms
 2171 is produced detector by detector. For each partition of each chamber, can be found:

2172

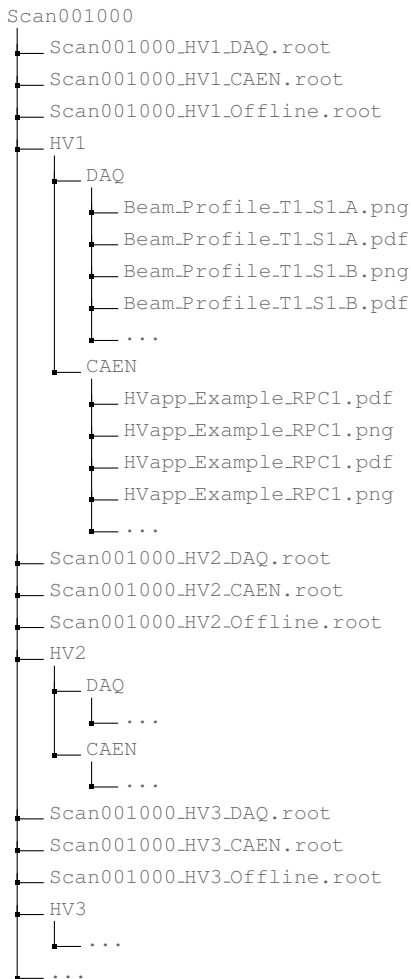
- `Time_Profile_Tt_Sc_p` shows the time profile of all recorded events (number of events per
 2173 time bin),
- `Hit_Profile_Tt_Sc_p` shows the hit profile of all recorded events (number of events per chan-
 2175 nel),
- `Hit_Multiplicity_Tt_Sc_p` shows the hit multiplicity (number of hits per event) of all recorded
 2177 events (number of occurrences per multiplicity bin),
- `Strip_Mean_Noise_Tt_Sc_p` shows noise/gamma rate per unit area for each strip in a se-
 2179 lected time range. After filters are applied on `Time_Profile_Tt_Sc_p`, the filtered version
 2180 of `Hit_Profile_Tt_Sc_p` is normalised to the total integrated time and active detection area
 2181 of a single channel,
- `Strip_Activity_Tt_Sc_p` shows noise/gamma activity for each strip (normalised version of
 2183 previous histogram - strip activity = strip rate / average partition rate),
- `Strip_Homogeneity_Tt_Sc_p` shows the *homogeneity* of a given partition ($\text{homogeneity} = \exp(-\text{strip rates standard deviation(strip rates in partition/average partition rate)})$),
- `mask_Strip_Mean_Noise_Tt_Sc_p` shows noise/gamma rate per unit area for each masked
 2187 strip in a selected time range. Offline, the user can control the noise/gamma rate and decide to
 2188 mask the strips that are judged to be noisy or dead. This is done via the *Masking Tool* provided
 2189 by the webDCS,

- 2190 ● `mask_Strip_Activity_Tt_Sc_p` shows noise/gamma activity per unit area for each masked
2191 strip with respect to the average rate of active strips,
- 2192 ● `NoiseCSize_H_Tt_Sc_p` shows noise/gamma cluster size, a cluster being constructed out of
2193 adjacent strips giving a signal at the *same time* (hits within a time window of 25 ns),
- 2194 ● `NoiseCMult_H_Tt_Sc_p` shows noise/gamma cluster multiplicity (number of reconstructed
2195 clusters per event),
- 2196 ● `Chip_Mean_Noise_Tt_Sc_p` shows the same information than `Strip_Mean_Noise_Tt_Scp` us-
2197 ing a different binning (1 chip corresponds to 8 strips),
- 2198 ● `Chip_Activity_Tt_Sc_p` shows the same information than `Strip_Activity_Tt_Scp` using
2199 chip binning,
- 2200 ● `Chip_Homogeneity_Tt_Sc_p` shows the homogeneity of a given partition using chip binning,
- 2201 ● `Beam_Profile_Tt_Sc_p` shows the estimated beam profile when taking efficiency scan. This
2202 is obtained by filtering `Time_Profile_Tt_Sc_p` to only consider the muon peak where the
2203 noise/gamma background has been subtracted. The resulting hit profile corresponds to the
2204 beam profile on the detector channels,
- 2205 ● `L0_Efficiency_Tt_Sc_p` shows the level 0 efficiency that was estimated **without** muon track-
2206 ing,
- 2207 ● `MuonCSize_H_Tt_Sc_p` shows the level 0 muon cluster size that was estimated **without** muon
2208 tracking, and
- 2209 ● `MuonCMult_H_Tt_Sc_p` shows the level 0 muon cluster multiplicity that was estimated **without**
2210 muon tracking.

2211 In the histogram labels, t stands for the trolley number (1 or 3), c for the chamber slot label in
2212 trolley t and p for the partition label (A, B, C or D depending on the chamber layout) as explained
2213 in Chapter ??.

2214 In the context of GIF++, an extra script called by the webDCS is called to extract the histograms
2215 from the ROOT files. The histograms are then stored in PNG and PDF formats into the correspond-
2216 ing folder (a single folder per HV step, so per ROOT file). the goal is to then display the histograms
2217 on the Data Quality Monitoring (DQM) page of the webDCS in order for the users to control the
2218 quality of the data taking at the end of data taking. An example of histogram organisation is given
2219 below:

2221



2222 *Here can put some screens from the webDCS to show the DQM and the plots available to users.*

2223

2224 B.2.1.2 CSV files

2225 Moreover, up to 3 CSV files can be created depending on which ones of the 3 input files were in the

2226 data folder:

- 2227 • Offline-Corrupted.csv , is used to keep track of the amount of data that was corrupted and**
- 2228 removed from old data format files that don't contain any data quality flag.**
- 2229 • Offline-Current.csv , contains the summary of the currents and voltages applied on each**
- 2230 RPC HV channel.**
- 2231 • Offline-L0-EffC1.csv , is used to write the efficiencies, cluster size and cluster multiplicity**
- 2232 of efficiency runs. Note that L0 refers here to *Level 0* and means that the results of efficiency and**
- 2233 clusterization are a first approximation calculated without performing any muon tracking in**

2234 between the different detectors. This offline tool provides the user with a preliminar calculation
 2235 of the efficiency and of the muon event parameters. Another analysis software especially
 2236 dedicated to muon tracking is called on selected data to retrieve the results of efficiency and
 2237 muon clusterization using a tracking algorithm to discriminate noise or gamma from muons
 2238 as muons are the only particles that pass through the full setup, leaving hits than can be used
 2239 to reconstruct their tracks.

- 2240 • `Offline-Rate.csv`, is used to write the noise or gamma rates measured in the detector readout
 2241 partitions.

2242 Note that these 4 CSV files are created along with their *headers* (`Offline-[...]-Header.csv`
 2243 containing the names of each data columns) and are automatically merged together when the offline
 2244 analysis tool is called from the webDCS, contrary to the case where the tool is runned locally from
 2245 the terminal as the merging bash script is then not called. Thus, the resulting files, used to make
 2246 official plots, are:

- 2247 • `Corrupted.csv`,
 2248 • `Current.csv`,
 2249 • `L0-EffCl.csv`.
 2250 • `Rate.csv`.

2251 B.3 Analysis inputs and information handling

2252 The usage of the Offline Analysis tool as well as its output have been presented in the previous section.
 2253 It is now important to dig further and start looking at the source code and the inputs necessary
 2254 for the tool to work. Indeed, other than the raw ROOT data files that are analysed, more information
 2255 needs to be imported inside of the program to perform the analysis such as the description of the
 2256 setup inside of GIFT++ at the time of data taking (number of trolleys, of RPCs, dimensions of the
 2257 detectors, etc...) or the mapping that links the TDC channels to the coresponding RPC channels in
 2258 order to translate the TDC information into human readable data. 2 files are used to transmit all this
 2259 information:
 2260

- 2261 • `Dimensions.ini`, that provides the necessary setup and RPC information, and
 2262 • `ChannelsMapping.csv`, that gives the link between the TDC and RPC channels as well as the
 2263 *mask* for each channel (masked or not?).

2264 B.3.1 Dimensions file and InFile parser

2265 This input file, present in every data folder, allows the analysis tool to know of the number of active
 2266 trolleys, the number of active RPCs in those trolleys, and the details about each RPCs such as
 2267 the number of RPC gaps, the number of pseudo-rapidity partitions (for CMS-like prototypes), the
 2268 number of strips per partion or the dimensions. To do so, there are 3 types of groups in the INI file
 2269 architecture. A first general group, appearing only once at the head of the document, gives information
 2270 about the number of active trolleys as well as their IDs, as presented in Source Code B.1. For

2271 each active trolley, a group similar to Source Code B.2 can be found containing information about
 2272 the number of active detectors in the trolley and their IDs. Each trolley group as a `Tt` name format,
 2273 where `t` is the trolley ID. Finally, for each detector stored in slots of an active trolley, there is a group
 2274 providing information about their names and dimensions, as shown in Source Code B.3. Each slot
 2275 group as a `TtSs` name format, where `s` is the slot ID of trolley `t` where the active RPC is hosted.

```
2276 [General]
2277 nTrolleys=2
  TrolleysID=13
```

2278 *Source Code B.1: Example of `[General]` group as might be found in `Dimensions.ini`. In Gif++, only 2 trolleys are available to hold RPCs and place them inside of the bunker for irradiation. The IDs of the trolleys are written in a single string as "13" and then read character by character by the program.*

```
2279 [T1]
  nSlots=4
  SlotsID=1234
```

2280 *Source Code B.2: Example of trolley group as might be found in `Dimensions.ini`. In this example, the file tells that there are 4 detectors placed in the holding slots of the trolley `T1` and that their IDs, written as a single string variable, are 1, 2, 3 and 4.*

```
2281 [T1S1]
  Name=RE2-2-NPD-BARC-8
  Partitions=3
  Gaps=3
  Gap1=BOT
  Gap2=TN
  Gap3=TW
  AreaGap1=11694.25
  AreaGap2=6432
  AreaGap3=4582.82
  Strips=32
  ActiveArea-A=157.8
  ActiveArea-B=121.69
  ActiveArea-C=93.03
```

2282 *Source Code B.3: Example of slot group as might be found in `Dimensions.ini`. In this example, the file provides information about a detector named `RE2-2-NPD-BARC-8`, having 3 pseudo-rapidity readout partitions and stored in slot `S1` of trolley `T1`. This is a CMS RE2-2 type of detector. This information will then be used for example to compute the rate per unit area calculation.*

2283 This information is readout and stored in a C++ object called `IniFile`, that parses the information
 2284 in the INI input file and stores it into a local buffer for later use. This INI parser is the exact same
 2285 one that was previously developed for the Gif++ DAQ and described in Appendix A.5.2.

2286 B.3.2 TDC to RPC link file and Mapping

2287 The same way the INI dimension file information is stored using `map`, the channel mapping and mask
 2288 information is stored and accessed through `map`. First of all, the mapping CSV file is organised into
 2289 3 columns separated by tabulations (and not by commas, as expected for CSV files as it is easier using
 2290 streams to read tab or space separated data using C++):

2291

2292 RPC_channel TDC_channel mask

2293 using as formatting for each field:

2294
2295 TSCCC TCCC M

2296 TSCCC is a 5-digit integer where τ is the trolley ID, s the slot ID in which the RPC is held insite
2297 the trolley τ and ccc is the RPC channel number, or *strip* number, that can take values up to
2298 3-digits depending on the detector,

2299 TCCC is a 4 digit integer where τ is the TDC ID, ccc is the TDC channel number that can take values
2300 in between 0 and 127, and

2301 M is a 1-digit integer indicating if the channel should be considered ($M = 1$) or discarded ($M = 0$)
2302 during analysis.

2303 This mapping and masking information is readout and stored thanks to the object `Mapping`, pre-
2304 sented in Source Code B.4. Similarly to `IniFile` objects, this class has private methods. The first
2305 one, `Mapping::CheckIfNewLine()` is used to find the newline character '`\n`' or return character
2306 '`\r`' (depending on which kind of operating system interacted with the file). This is used for the
2307 simple reason that the masking information has been introduced only during the year 2017 but the
2308 channel mapping files exist since 2015 and the very beginning of data taking at GIF++. This means
2309 that in the older data folders, before the upgrade, the channel mapping file only had 2 columns, the
2310 RPC channel and the TDC channel. For compatibility reasons, this method helps controling the
2311 character following the readout of the 2 first fields of a line. In case any end of line character is
2312 found, no mask information is present in the file and the default $M = 1$ is used. On the contrary, if
2313 the next character was a tabulation or a space, the mask information is present.

2314 Once the 3 fields have been readout, the second private method `Mapping::CheckIfTDCCh()` is
2315 used to control that the TDC channel is an existing TDC channel. Finally, the information is stored
2316 into 3 different maps (`Link`, `ReverseLink` and `Mask`) thanks to the public method `Mapping::Read()`.
2317 `Link` allows to get the RPC channel by knowing the TDC channel while `ReverseLink` does the op-
2318 posite by returning the TDC channel by knowing the RPC channel. Finally, `Mask` returns the mask
2319 associated to a given RPC channel.

```

2320 typedef map<Uint,Uint> MappingData;

2321 class Mapping {
2322     private:
2323         bool          CheckIfNewLine(char next);
2324         bool          CheckIfTDCCh(Uint channel);
2325         string        FileName;
2326         MappingData  Link;
2327         MappingData  ReverseLink;
2328         MappingData  Mask;
2329         int           Error;
2330
2331     public:
2332         Mapping();
2333         Mapping(string baseName);
2334         ~Mapping();
2335
2336         void SetFileName(const string filename);
2337         int  Read();
2338         Uint GetLink(Uint tdcchannel);
2339         Uint GetReverse(Uint rpcchannel);
2340         Uint GetMask(Uint rpcchannel);
2341     };

```

2322 *Source Code B.4: Description of C++ object Mapping used as a parser for the channel mapping and mask file.*

2323 B.4 Description of GIF++ setup within the Offline Analysis tool

2324 In the previous section, the tool input files have been discussed. The dimension file information is
 2325 stored in a map hosted by the `IniFile` object. But this information is then used to create a series of
 2326 new objects that helps defining the GIF++ infrastructure directly into the Offline Analysis. Indeed,
 2327 from the `RPC`, to the more general `Infrastructure`, every element of the GIF++ infrastrucutre is
 2328 recreated for each data analysis based on the information provided in input. All this information
 2329 about the infrastructure will be used to assign each hit signal to a specific strip channel of a specific
 2330 detector, and having a specific active area. This way, rate per unit area calculation is possible.
 2331

2332 B.4.1 RPC objects

2333 `RPC` objects have been developped to represent physical active detectors in GIF++ at the moment
 2334 of data taking. Thus, there are as many `RPC` objects created during the analysis than there were
 2335 active `RPCs` tested during a run. Each `RPC` hosts the information present in the corresponding INI
 2336 slot group, as shown in B.3, and organises it using a similar architecture. This can be seen from
 2337 *Source Code B.5*.

2338 To make the object more compact, the lists of gap labels, of gap active areas and strip active
 2339 areas are stored into `vector` dynamical containers. `RPC` objects are always contructed thanks to the
 2340 dimension file information stored into the `IniFILE` and their ID, using the format `TtSs`. Using the
 2341 `RPC` ID, the constructor calls the methods of `IniFILE` to initialise the `RPC`. The other constructors
 2342 are not used but exist in case of need. Finally, some getters have been written to access the different
 2343 private parameters storing the detector information.

```

2344 class RPC{
2345     private:
2346         string name;           //RPC name as in webDCS database
2347         Uint nGaps;          //Number of gaps in the RPC
2348         Uint nPartitions;    //Number of partitions in the RPC
2349         Uint nStrips;        //Number of strips per partition
2350         vector<string> gaps; //List of gap labels (BOT, TOP, etc...)
2351         vector<float> gapGeo;   //List of gap active areas
2352         vector<float> stripGeo; //List of strip active areas
2353
2354     public:
2355         RPC();
2356         RPC(string ID, IniFile* geofile);
2357         RPC(const RPC& other);
2358         ~RPC();
2359         RPC& operator=(const RPC& other);
2360
2361         string GetName();
2362         Uint GetNGaps();
2363         Uint GetNPartitions();
2364         Uint GetNStrips();
2365         string GetGap(Uint g);
2366         float GetGapGeo(Uint g);
2367         float GetStripGeo(Uint p);
2368     };

```

2346 *Source Code B.5: Description of C++ objects RPC that describe each active detectors used during data taking.*

2347 B.4.2 Trolley objects

2348 Trolley objects have been developped to represent physical active trolleys in GIFT++ at the moment
 2349 of data taking. Thus, there are as many trolley objects created during the analysis than there were
 2350 active trolleys hosting tested RPCs during a run. Each Trolley hosts the information present in the
 2351 corresponding INI trolley group, as shown in B.2, and organises it using a similar architecture. In
 2352 addition to the information hosted in the INI file, these object have a dynamical container of RPC
 2353 objects, representing the active detectors the active trolley was hosting at the time of data taking.
 2354 This can been seen from Source Code B.6.

2355 Trolley objects are always contructed thanks to the dimension file information stored into the
 2356 IniFILE and their ID, using the format Tt. Using the Trolley ID, the constructor calls the methods
 2357 of IniFILE to initialise the Trolley. Retrieving the information of the RPC IDs via SlotsID, a new
 2358 RPC is constructed and added to the container RPCs for each character in the ID string. The other
 2359 constructors are not used but exist in case of need. Finally, some getters have been written to access
 2360 the different private parameters storing the trolley and detectors information.

```

2361
class Trolley{
    private:
        Uint          nSlots; //Number of active RPCs in the considered trolley
        string        SlotsID; //Active RPC IDs written into a string
        vector<RPC*> RPCs;   //List of active RPCs

    public:
        //Constructors, destructor and operator =
        Trolley();
        Trolley(string ID, IniFile* geofile);
        Trolley(const Trolley& other);
        ~Trolley();
        Trolley& operator=(const Trolley& other);

        //Get GIFTrolley members
        Uint  GetNSlots();
        string GetSlotsID();
        Uint   GetSlotID(Uint s);

        //Manage RPC list
        RPC*  GetRPC(Uint r);
        void  DeleteRPC(Uint r);

        //Methods to get members of RPC objects stored in RPCs
        string GetName(Uint r);
        Uint   GetNGaps(Uint r);
        Uint   GetNPartitions(Uint r);
        Uint   GetNStrips(Uint r);
        string GetGap(Uint r, Uint g);
        float  GetGapGeo(Uint r, Uint g);
        float  GetStripGeo(Uint r, Uint p);
    };

```

Source Code B.6: Description of C++ objects `Trolley` that describe each active trolley used during data taking.

2364 B.4.3 Infrastructure object

2365 The `Infrastructure` object has been developped to represent the GIFT++ bunker area dedicated to
 2366 CMS RPC experiments. With this very specific object, all the information about the CMS RPC
 2367 setup within GIFT++ at the moment of data taking is stored. It hosts the information present in the
 2368 corresponding INI general group, as shown in B.1, and organises it using a similar architecture. In
 2369 addition to the information hosted in the INI file, this object have a dynamical container of `Trolley`
 2370 objects, representing the active tolleys in GIFT++ area. This can be seen from Source Code B.7.

2371 The `Infrastructure` object is always contructed thanks to the dimension file information stored
 2372 into the `IniFILE`. Retrieving the information of the trolley IDs via `TrolleysID`, a new `Trolley` is
 2373 constructed and added to the container `Trolleys` for each character in the ID `string`. By extension,
 2374 it is easy to understand that the process described in Section B.4.2 for the construction of RPCs
 2375 takes place when a trolley is constructed. The other constructors are not used but exist in case of
 2376 need. Finally, some getters have been written to access the different private parameters storing the
 2377 infrastructure, tolleys and detectors information.

```

2378 class Infrastructure {
2379     private:
2380         Uint             nTrolleys;    //Number of active Trolleys in the run
2381         string          TrolleysID;   //Active trolley IDs written into a string
2382         vector<Trolley*> Trolleys;   //List of active Trolleys (struct)
2383
2384     public:
2385         //Constructors and destructor
2386         Infrastructure();
2387         Infrastructure(IniFile* geofile);
2388         Infrastructure(const Infrastructure& other);
2389         ~Infrastructure();
2390         Infrastructure& operator=(const Infrastructure& other);
2391
2392         //Get Infrastructure members
2393         Uint  GetNTrolleys();
2394         string GetTrolleysID();
2395         Uint   GetTrolleyID(Uint t);
2396
2397         //Manage Trolleys
2398         Trolley* GetTrolley(Uint t);
2399         void    DeleteTrolley(Uint t);
2400
2401         //Methods to get members of GIFTrolley objects stored in Trolleys
2402         Uint  GetNSlots(Uint t);
2403         string GetSlotsID(Uint t);
2404         Uint   GetSlotID(Uint t, Uint s);
2405         RPC*  GetRPC(Uint t, Uint r);
2406
2407         //Methods to get members of RPC objects stored in RPCs
2408         string GetName(Uint t, Uint r);
2409         Uint   GetNGaps(Uint t, Uint r);
2410         Uint   GetNPartitions(Uint t, Uint r);
2411         Uint   GetNStrips(Uint t, Uint r);
2412         string GetGap(Uint t, Uint r, Uint g);
2413         float  GetGapGeo(Uint t, Uint r, Uint g);
2414         float  GetStripGeo(Uint t, Uint r, Uint p);
2415     };

```

Source Code B.7: Description of C++ object *Infrastructure* that contains the full information about CMS RPC experiment in GIF++.

2381 B.5 Handeling of data

2382 As discussed in Appendix A.4.2, the raw data as a `TTree` architecture where every entry is related to
2383 a trigger signal provided by a muon or a random pulse, whether the goal of the data taking was to
2384 measure the performance of the detector or the noise/gamma background respectively. Each of these
2385 entries, referred also as events, contain a more or less full list of hits in the TDC channels to which
2386 the detectors are connected. To this list of hits corresponds a list of time stamps, marking the arrival
2387 of the hits within the TDC channel.

2388 The infrastructure of the CMS RPC experiment within GIF++ being defined, combining the
2389 information about the raw data with the information provided by both the mapping/mask file and the
2390 dimension file allows to build new physical objects that will help in computing efficiency or rates.

2391 B.5.1 RPC hits

2392 The raw data stored in the ROOT file as output of the GIFT++ DAQ, is readout by the analysis tool
 2393 using the structure `RAWData` presented in Source Code B.9 that differs from the structure presented
 2394 in Appendix A.4.2 as it is not meant to hold all of the data contained in the ROOT file. In this sense,
 2395 this structure is in the case of the offline analysis tool not a dynamical object and will only be storing
 2396 a single event contained in a single entry of the `TTree`.

```
2397
  class RPCHit {
    private:
      Uint Channel;      //RPC channel according to mapping (5 digits)
      Uint Trolley;     //0, 1 or 3 (1st digit of the RPC channel)
      Uint Station;     //Slot where is held the RPC in Trolley (2nd digit)
      Uint Strip;       //Physical RPC strip where the hit occurred (last 3
→   digits)
      Uint Partition;   //Readout partition along eta segmentation
      float TimeStamp; //Time stamp of the arrival in TDC

    public:
      //Constructors, destructor & operator =
      RPCHit();
      RPCHit(Uint channel, float time, Infrastructure* Infra);
      RPCHit(const RPCHit& other);
      ~RPCHit();
      RPCHit& operator=(const RPCHit& other);

      //Get RPCHit members
      Uint GetChannel();
      Uint GetTrolley();
      Uint GetStation();
      Uint GetStrip();
      Uint GetPartition();
      float GetTime();
    };

    typedef vector<RPCHit> HitList;
    typedef struct GIFHitList { HitList rpc[NTROLLEYS][NSLOTS][NPARTITIONS]; }
→   GIFHitList;

    bool SortHitbyStrip(RPCHit h1, RPCHit h2);
    bool SortHitbyTime(RPCHit h1, RPCHit h2);
  
```

2399 *Source Code B.8: Description of C++ object `RPCHit`.*

```
2400
  struct RAWData{
    int iEvent;        //Event i
    int TDCNHits;    //Number of hits in event i
    int QFlag;         //Quality flag list (1 flag digit per TDC)
    vector<Uint> *TDCCh; //List of channels giving hits per event
    vector<float> *TDCTS; //List of the corresponding time stamps
  };

```

2401 *Source Code B.9: Description of C++ structure `RAWData`.*

2402 Each member of the structure is then linked to the corresponding branch of the ROOT data tree,
 2403 as shown in the example of Source Code B.10, and using the method `GetEntry(int i)` of the ROOT
 2404 class `TTree` will update the state of the members of `RAWData`.

```

2405 TTree* dataTree = (TTree*)dataFile.Get("RAWData");
2406 RAWData data;
2407
2408 dataTree->SetBranchAddress("EventNumber", &data.iEvent);
2409 dataTree->SetBranchAddress("number_of_hits", &data.TDCNHits);
2410 dataTree->SetBranchAddress("Quality_flag", &data.QFlag);
2411 dataTree->SetBranchAddress("TDC_channel", &data.TDCCh);
2412 dataTree->SetBranchAddress("TDC_TimeStamp", &data.TDCTS);

```

2407 *Source Code B.10: Example of link in between RAWData and TTree.*

2408 The data is then analysed entry by entry and to each element of the TDC channel list, a `RPCHit` is
 2409 constructed by linking each TDC channel to the corresponding RPC channel thanks to the `Mapping`
 2410 object. The information carried by the RPC channel format allows to easily retrieve the trolley and
 2411 slot from which the hit was recorded (see section B.3.2). Using these 2 values, the readout partition
 2412 can be found by knowing the strip channel and comparing it with the number of partitions and strips
 2413 per partition stored into the `Infrastructure` object.

2414 Thus `RPCHit` objects are then stored into 3D dynamical list called `GIFHitList` (Source Code B.9)
 2415 where the 3 dimensions refer to the 3 layers of the readout in `GIF++` : in the bunker there are *trolleys*
 2416 (τ) holding detectors in *slots* (s) and each detector readout is divided into 1 or more pseudo-rapidity
 2417 *partitions* (p). Using these 3 information allows to assign an address to each readout partition and
 2418 this address will point to a specific hit list.

2419

2420 B.5.2 Clusters of hits

2421 All the hits contained in the ROOT file have been sorted into the different hit lists through the
 2422 `GIFHitList`. At this point, it is possible to start looking for clusters. A cluster is a group of adjacent
 2423 strips getting hits within a time window of 25 ns. These strips are then assumed to be part of the same
 2424 physical avalanche signal generated by a muon passing through the chamber or by the interaction of
 2425 a gamma stopping into the electrodes of the RPCs.

2426 To keep the cluster information, `RPCCluster` objects have been defined as shown in Source
 2427 Code B.11. Using the information of each individual `RPCHit` taken out of the hit list, it stores
 2428 the cluster size (number of adjacent strips composing the cluster), the first and last hit, the center for
 2429 spatial reconstruction and finally the start and stop time stamps as well as te time spread in between
 2430 the first and last hit.

```

2431
class RPCCluster{
    private:
        Uint ClusterSize; //Size of cluster #ID
        Uint FirstStrip; //First strip of cluster #ID
        Uint LastStrip; //Last strip of cluster #ID
        float Center; //Center of cluster #ID ((first+last)/2)
        float StartStamp; //Time stamp of the earliest hit of cluster #ID
        float StopStamp; //Time stamp of the latest hit of cluster #ID
        float TimeSpread; //Time difference between earliest and latest hits
                           //of cluster #ID
    public:
        //Constructors, destructor & operator =
        RPCCluster();
        RPCCluster(HitList List, Uint cID, Uint cSize, Uint first, Uint firstID);
        RPCCluster(const RPCCluster& other);
        ~RPCCluster();
        RPCCluster& operator=(const RPCCluster& other);

        //Get Cluster members
        Uint GetID();
        Uint GetSize();
        Uint GetFirstStrip();
        Uint GetLastStrip();
        float GetCenter();
        float GetStart();
        float GetStop();
        float GetSpread();
    };

typedef vector<RPCCluster> ClusterList;

//Other functions to build cluster lists out of hit lists
void BuildClusters(HitList &cluster, ClusterList &clusterList);
void Clusterization(HitList &hits, TH1 *hcSize, TH1 *hcMult);

```

2433 *Source Code B.11: Description of C++ object Cluster.*

2434 To investigate the hit list of a given detector partition, the function `Clusterization()` defined
 2435 in `include/Cluster.h` needs the hits in the list to be time sorted. This is achieved by calling func-
 2436 tion `sort()` of library `<algorithm>` using the comparator `SortHitbyTime(RPCHit h1, RPCHit h2)`
 2437 defined in `include/RPCHit.h` that returns `true` if the time stamp of hit `h1` is lower than that of `h2`.
 2438 A first isolation of strips is made only based on time information. All the hits within the 25 ns win-
 2439 dow are taken separately from the rest. Then, this sub-list of hits is sorted this time by ascending
 2440 strip number, using this time the comparator `SortHitbyStrip(RPCHit h1, RPCHit h2)`. Finally, the
 2441 groups of adjacent strips are used to construct `RPCCluster` objects that are then stored in a temporary
 2442 list of clusters that is at the end of the process used to know how many clusters were reconstructed
 2443 and to fill their sizes into an histogram that will allows to know the mean size of muon or gamma
 2444 clusters.

2445

2446 B.6 DAQ data Analysis

2447 All the ingredients to analyse GIF++ data have been defined. This section will focus on the different
 2448 part of the analysis performed on the data, from determining the type of data the tool is dealing with

2449 to calculating the rate in each detector or reconstructing muon or gamma clusters.

2450 B.6.1 Determination of the run type

2451 In GIF++, both the performance of the detectors in detecting muons in an irradiated environment and
 2452 the gamma background can be independantly measured. These corresponds to different run types
 2453 and thus, to different TDC settings giving different data to look at.

2454
 2455 In the case of performance measurements, the trigger for data taking is provided by the coïncidence
 2456 of several scintillators when muons from the beam passing through the area are detected. Data
 2457 is collected in a 600 ns wide window around the arrival of muons in the RPCs. The expected time
 2458 distribution of hits is shown in Figure B.1a. The muon peak is clearly visible in the center of the
 2459 distribution and is to be extracted from the gamma background that composes the flat part of the
 2460 distribution.

2461 On the other hand, gamma background or noise measurements are focussed on the non muon
 2462 related physics and the trigger needs to be independant from the muons to give a good measurement
 2463 of the gamma/noise distribution as seen by the detectors. The trigger is then provided by a pulse
 2464 generator at a frequency of 300 Hz whose pulse is not likely to be on time with a muon. In order
 2465 to increase the integrated time without increasing the acquisition time too much, the width of the
 2466 acquisition windows are increased to 10 μ s. The time distribution of the hits is expected to be flat, as
 2467 shown by Figure B.1b.

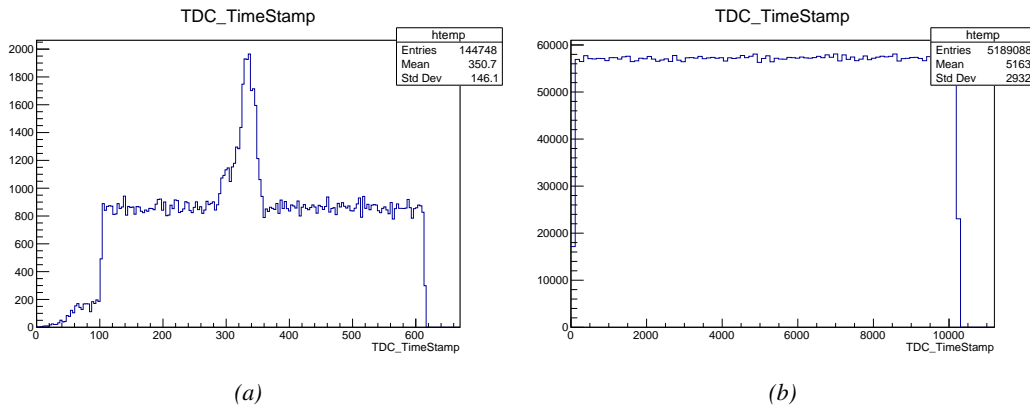


Figure B.1: Example of expected hit time distributions in the cases of efficiency (Figure B.1a) and noise/gamma rate per unit area (Figure B.1b) measurements as extracted from the raw ROOT files. The unit along the x-axis corresponds to ns. The fact that "the" muon peak is not well defined in Figure B.1a is due to the contribution of all the RPCs being tested at the same time that don't necessarily have the same signal arrival time. Each individual peak can have an offset with the ones of other detectors. The inconsistency in the first 100 ns of both time distributions is an artefact of the TDCs and are systematically rejected during the analysis.

2468 The ROOT files include a TTree called RunParameters containing, among other things, the in-
 2469 formation related to the type of run. The run type can then be accessed as described by Source
 2470 Code B.12 and the function IsEfficiencyRun() is then used to determine if the run file is an effi-
 2471 ciency run or, on the contrary, another type of run (noise or gamma measurement).

```

2472     TTree* RunParameters = (TTree*)dataFile.Get("RunParameters");
2473     TString* RunType = new TString();
2474     RunParameters->SetBranchAddress("RunType", &RunType);
2475     RunParameters->GetEntry(0);

```

2474 *Source Code B.12: Access to the run type contained in TTree* RunParameters.*

2475 Finally, the data files will have a slightly different content whether it was collected before or after
 2476 October 2017 and the upgrade of the DAQ software that brought a new information into the ROOT
 2477 output. This is discussed in Appendix A.4.3 and implies that the analysis will differ a little depending
 2478 on the data format. Indeed, as no information on the data quality is stored, in older data files, the cor-
 2479 rections for missing events has to be done at the end of the analysis. The information about the type
 2480 of data format is stored in the variable **bool** `isNewFormat` by checking the list of branches contained
 2481 in the data tree via the methods `TTree::GetListOfBranches()` and `TCollection::Contains()`.

2482 B.6.2 Beam time window calculation for efficiency runs

2483 Knowing the run type is important first of all to know the width of the acquisition window to be used
 2484 for the rate calculation and finally to be able to seek for muons. Indeed, the peak that appears in the
 2485 time distribution for each detectors is then fitted to extract the most probable time window in which
 2486 the tool should look for muon hits. The data outside of this time window is then used to evaluate the
 2487 noise or gamma background the detector was subjected to during the data taking. Computing the
 2488 position of the peak is done calling the function `SetBeamWindow()` defined in file `src/RPCHit.cc` that
 2489 loops a first time on the data. The data is first sorted in a 3D array of 1D histograms (`GIFH1Array`, see
 2490 `include/types.h`). Then the location of the highest bin is determined using `TH1::GetMaximumBin()`
 2491 and is used to define a window in which a gaussian fit will be applied to compute the peak width.
 2492 This window is a 80 ns defined by Formula B.1 around the central bin.

$$t_{center}(ns) = bin \times width_{bin}(ns) \quad (\text{B.1a})$$

$$[t_{low}; t_{high}] = [t_{center} - 40; t_{center} + 40] \quad (\text{B.1b})$$

2493 Before the fit is performed, the average number of noise/gamma hits per bin is evaluated using
 2494 the data outside of the fit window. Excluding the first 100 ns, the average number of hits per bin
 2495 due to the noise or gamma is defined by Formula B.2 after extracting the amount of hits in the time
 2496 windows $[100; t_{low}]$ and $[t_{high}; 600]$ thanks to the method `TH1::Integral()`. This average number
 2497 of hits is then subtracted to every bin of the 1D histogram, in order to *clean* it from the noise or
 2498 gamma contribution as much as possible to improve the fit quality. Bins where $\langle n_{hits} \rangle$ is greater
 2499 than the actual bin content are set to 0.

$$\Delta t_{noise}(ns) = 600 \overbrace{-t_{high} + t_{low}}^{-80ns} - 100 = 420ns \quad (\text{B.2a})$$

$$\langle n_{hits} \rangle = width_{bin}(ns) \times \frac{\sum_{t=100}^{t_{low}} + \sum_{t=t_{high}}^{600}}{\Delta t_{noise}(ns)} \quad (\text{B.2b})$$

2500 Finally, the fit parameters are extracted and saved for each detector in 3D arrays of **float**
 2501 (`muonPeak`, see `include/types.h`), a first one for the mean arrival time of the muons, `PeakTime`,

2502 and a second one for the width of the peak, `PeakWidth`. The width is defined as 6σ of the gaussian
 2503 fit. The same settings are applied to every partitions of the same detector. To determine which one
 2504 of the detector's partitions is directly illuminated by the beam, the peak height of each partition is
 2505 compared and the highest one is then used to define the peak settings.

2506 **B.6.3 Data loop and histogram filling**

2507 3D arrays of histogram are created to store the data and display it on the DQM of GIF++ webDCS
 2508 for the use of shifters. These histograms, presented in section B.2.1.1, are filled while looping on
 2509 the data. Before starting the analysis loop, it is necessary to control the entry quality for the new
 2510 file formats featuring `QFlag`. If the `QFlag` value for this entry shows that 1 TDC or more have a
 2511 `CORRUPTED` flag, then this event is discarded. The loss of statistics is low enough to be neglected.
 2512 `QFlag` is controled using the function `IsCorruptedEvent()` defined in `src/utils.cc`. As explained
 2513 in Appendix A.4.3, each digit of this integer represent a TDC flag that can be 1 or 2. Each 2 is
 2514 the sign of a `CORRUPTED` state. Then, the data is accessed entry by entry in the ROOT `TTree` using
 2515 `RAWData` and each hit in the hit list is assigned to a detector channel and saved in the corresponding
 2516 histograms. In the first part of the analysis, in which the loop over the ROOT file's content is
 2517 performed, the different steps are:

2518 **1- RPC channel assignment and control:** a check is done on the RPC channel extracted thanks
 2519 to the mapping via the method `Mapping::GetLink()`. If the channel is not initialised and is 0, or if
 2520 the TDC channel was greater than 5127, the hit is discarded. This means there was a problem in the
 2521 mapping. Often a mapping problem leads to the crash of the offline tool.

2522 **2- Creation of a `RPCHit` object:** to easily get the trolley, slot and partition in which the hit has
 2523 been assigned, this object is particularly helpful.

2524 **3- General histograms are filled:** the hit is filled into the time distribution and the general hit
 2525 distribution histograms, and if the arrival time is within the first 100 ns, it is discarded and nothing
 2526 else happens and the loop proceeds with the next hit in the list.

2527 **4- Multiplicity counter:** the hit multiplicity counter of the corresponding detectors incremented.

2528 **5-a- Efficiency runs - Is the hit within the peak window? :** if the peak is contained in the peak
 2529 window previously defined in section B.6.2, the hit is filled into the beam hit profile histogram of
 2530 the corresponding chamber, added into the list of muon hits and increments the counter of *in time*
 2531 hits. The term *in time* here refers to the hits that are likely to be muons by arriving in the expected
 2532 time window. If the hit is outside of the peak window, it is filled into the noise profile histogram
 2533 of the corresponding detector, added into the list of noise/gamma hits and increments the counter of
 2534 noise/gamma hits.

2535 **5-b- Noise/gamma rate runs - Noise histograms are filled:** the hit is filled into the noise profile
 2536 histogram of the corresponding detector, added into the list of noise/gamma hits and increments the
 2537 counter of noise/gamma hits.

2539 After the loop on the hit list of the entry is over, the next step is to clusterize the 3D lists filled
 2540 in the previous steps. A 3D loop is then started over the active trolley, slot and RPC partitions to
 2541 access these objects. Each `NoiseHitList` and `MuonHitList`, in case of efficiency run, are clusterized
 2542 as described in section B.5.2. There corresponding cluster size and multiplicity histograms are filled
 2543 at the end of the clustering process. Then, the efficiency histogram is filled in case of efficiency run.
 2544 The selection is simply made by checking whether the RPC detected signals in the peak window
 2545 during this event. Nevertheless, it is useful to highlight that at this level, it is not possible yet to
 2546 discriminate in between a muon hit and noise or gamma hit. Thus, `MuonCSize_H`, `MuonCMult_H`
 2547 and `Efficiency0_H` are subjected to noise and gamma contamination. This contamination will be
 2548 estimated and corrected at the moment the results will be written into output CSV files. Finally, the
 2549 loop ends on the filling of the general hit multiplicity histogram.

2550 **B.6.4 Results calculation**

2551 As mentioned in section B.2.1, the analysis of DAQ data provides the user with 3 CSV files and
 2552 a ROOT file associated to each and every ROOT data file. The fourth CSV file is provided by the
 2553 extraction of the CEAN main frame data monitored during data taking and will be discussed later.
 2554 After looping on the data in the previous part of the analysis macro, the output files are created and a
 2555 3D loop on each RPC readout partitions is started to extract the histograms parameters and compute
 2556 the final results.

2557

2558 **B.6.4.1 Rate normalisation**

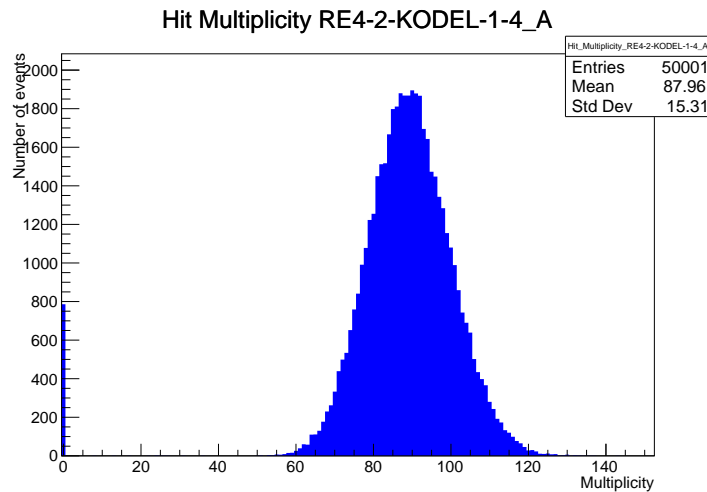


Figure B.2: The effect of the quality flag is explained by presenting the reconstructed hit multiplicity of a data file without `Quality_flag`. The artificial high content of bin 0 is the effect of corrupted data.

2559 To analyse old data format files, not containing any quality flag, it is needed to estimate the amount
 2560 of corrupted data via a fit as the corrupted data will always fill events with a fake "0 multiplicity".
 2561 Indeed, as no hits were stored in the DAQ ROOT files, these events artificially contribute to fill
 2562 the bin corresponding to a null multiplicity, as shown in Figure B.2. In the case the mean of the

hit multiplicity distribution is high, the contribution of the corrupted data can easily be evaluated for later correction by comparing the level of the bin at multiplicity 0 and of a skew fit curve that should indicate a value consistent with 0. A skew fit has been chosen over a Poisson fit as it was giving better results for lower mean multiplicity values. Nevertheless, for low irradiation cases, as explained in Appendix A.4.3, the hit multiplicity distribution mean is, on the contrary, rather small and the probability to record events without hits can't be considered small anymore, leading to a difficult and non-reliable estimation of the corruption. As can be seen in Source Code B.13, conditions have been applied to prevent bad fits and wrong corruption estimation in cases where :

- The difference in between the data for multiplicity 1 and the corresponding fit value should be lower than 1% of the total amount of data : $\frac{|n_{m=1} - sk(1)|}{N_{tot}} < 0.01$ where $n_{m=1}$ is the number of entries with multiplicity 1, $sk(1)$ the value of the skew fit, as defined by Formula 4.3, for multiplicity 1 and N_{tot} the total number of entries.

- The amount of data contained in the multiplicity 0 bin should not exceed 40% : $\frac{n_{m=0}}{N_{tot}} \leq 0.4$ where $n_{m=0}$ is the number of entries with multiplicity 0. This number has been determined to be the maximum to be able to separate the excess of data due to corruption from the hit multiplicity distribution.

Those 2 conditions need to be fulfilled to estimate the corruption of old data format files. If the fit was successful, the level of corruption is written in `Offline-Corrupted.csv` and the number of corrupted entries, refered as the integer `nEmptyEvent`, is subtracted from the total number of entries when the rate normalisation factor is computed as explicit in Source Code B.13. Note that for new data format files, the number of corrupted entries being set to 0, the definition of `rate_norm` stays valid.

```

2585   if(!isNewFormat){
2586     TF1* GaussFit = new TF1("gaussfit","[0]*exp(-0.5*((x-[1])/[2])**2)",0,Xmax);
2587     GaussFit->SetParameter(0,100);
2588     GaussFit->SetParameter(1,10);
2589     GaussFit->SetParameter(2,1);
2590     HitMultiplicity_H.rpc[T][S][p]->Fit(GaussFit,"LIQR","");
2591
2592     TF1* SkewFit = new TF1("skewfit","[0]*exp(-0.5*((x-[1])/[2])**2) / (1 +
2593     → exp(-[3]*(x-[4])))",0,Xmax);
2594     SkewFit->SetParameter(0,GaussFit->GetParameter(0));
2595     SkewFit->SetParameter(1,GaussFit->GetParameter(1));
2596     SkewFit->SetParameter(2,GaussFit->GetParameter(2));
2597     SkewFit->SetParameter(3,1);
2598     SkewFit->SetParameter(4,1);
2599     HitMultiplicity_H.rpc[T][S][p]->Fit(SkewFit,"LIQR","");
2600
2601     double fitValue = SkewFit->Eval(1,0,0,0);
2602     double dataValue = (double)HitMultiplicity_H.rpc[T][S][p]->GetBinContent(2);
2603     double difference = TMath::Abs(dataValue - fitValue);
2604     double fitTOdataVSentries_ratio = difference / (double)nEntries;
2605     bool isFitGOOD = fitTOdataVSentries_ratio < 0.01;
2606
2607     double nSinglehit = (double)HitMultiplicity_H.rpc[T][S][p]->GetBinContent(1);
2608     double lowMultRatio = nSinglehit / (double)nEntries;
2609     bool isMultLOW = lowMultRatio > 0.4;
2610
2611     if(isFitGOOD && !isMultLOW){
2612       nEmptyEvent = HitMultiplicity_H.rpc[T][S][p]->GetBinContent(1);
2613       nPhysics = (int)SkewFit->Eval(0,0,0,0);
2614       if(nPhysics < nEmptyEvent)
2615         nEmptyEvent = nEmptyEvent-nPhysics;
2616     }
2617
2618     double corrupt_ratio = 100.*(double)nEmptyEvent / (double)nEntries;
2619     outputCorrCSV << corrupt_ratio << '\t';
2620
2621     float rate_norm = 0.;
2622     float stripArea = GIFIInfra->GetStripGeo(tr,sl,p);
2623
2624     if(IsEfficiencyRun(RunType)){
2625       float noiseWindow = BMTDCWINDOW - TIMEREJECT - 2*PeakWidth.rpc[T][S][p];
2626       rate_norm = (nEntries-nEmptyEvent)*noiseWindow*1e-9*stripArea;
2627     } else
2628       rate_norm = (nEntries-nEmptyEvent)*RDMNOISEWDW*1e-9*stripArea;

```

Source Code B.13: Definition of the rate normalisation variable. It takes into account the number of non corrupted entries and the time window used for noise calculation, to estimate the total integrated time, and the strip active area to express the result as rate per unit area.

2588 B.6.4.2 Rate and activity

2589 At this point, the strip rate histograms, StripNoiseProfile_H.rpc[T][S][p], only contain an information about the total number of noise or rate hits each channel received during the data taking.
2590 As described in Source Code B.14, a loop on the strip channels will be used to normalise the content
2591 of the rate distribution histogram for each detector partitions. The initial number of hits recorded for
2592 a given bin will be extracted and 2 values will be computed:

- 2594 ● the strip rate, defined as the number of hits recorded in the bin normalised like described in
 2595 the previous section, using the variable `rate_norm`, and

- 2596 ● the strip activity, defined as the number of hits recorded in the bin normalised to the average
 2597 number of hits per bin contained in the partition histogram, using the variable `averageNhit`.
 2598 This value provides an information on the homogeneity of the detector response to the gamma
 2599 background or of the detector noise. An activity of 1 corresponds to an average response.
 2600 Above 1, the channel is more active than the average and bellow 1, the channel is less active.

```

int nNoise = StripNoiseProfile_H.rpc[T][S][p]->GetEntries();
float averageNhit = (nNoise>0) ? (float)(nNoise/nStripsPart) : 1.;

for(Uint st = 1; st <= nStripsPart; st++) {
    float stripRate =
        StripNoiseProfile_H.rpc[T][S][p]->GetBinContent(st)/rate_norm;
    float stripAct =
        StripNoiseProfile_H.rpc[T][S][p]->GetBinContent(st)/averageNhit;

    StripNoiseProfile_H.rpc[T][S][p]->SetBinContent(st,stripRate);
    StripActivity_H.rpc[T][S][p]->SetBinContent(st,stripAct);
}

```

2602 *Source Code B.14: Description of the loop that allows to set the content of each strip rate and strip activity
 channel for each detector partition.*

2603 On each detector partitions, which are readout by a single FEE, all the channels are not processed
 2604 by the same chip. Each chip can give a different noise response and thus, histograms using a chip
 2605 binning are used to investigate chip related noise behaviours. The average values of the strip rate
 2606 or activity grouped into a given chip are extracted using the using the function `GetChipBin()` and
 2607 stored in dedicated histograms as described in Source Codes B.15 and B.16 respectively.

```

2608 float GetChipBin(TH1* H, Uint chip){
    Uint start = 1 + chip*NSTRIPSCHIP;
    int nActive = NSTRIPSCHIP;
    float mean = 0.;

    for(Uint b = start; b <= (chip+1)*NSTRIPSCHIP; b++) {
        float value = H->GetBinContent(b);
        mean += value;
        if(value == 0.) nActive--;
    }

    if(nActive != 0) mean /= (float)nActive;
    else mean = 0.;

    return mean;
}

```

2610 *Source Code B.15: Function used to compute the content of a bin for an histogram using chip binning.*

```

2611   for(UInt ch = 0; ch < (nStripsPart/NSTRIPSCHIP); ch++) {
2612     ChipMeanNoiseProf_H.rpc[T][S][p]->
2613       SetBinContent(ch+1,GetChipBin(StripNoiseProfile_H.rpc[T][S][p],ch));
2614     ChipActivity_H.rpc[T][S][p]->
2615       SetBinContent(ch+1,GetChipBin(StripActivity_H.rpc[T][S][p],ch));
2616   }

```

Source Code B.16: Description of the loop that allows to set the content of each chip rate and chip activity bins for each detector partition knowing the information contained in the corresponding strip distribution histograms.

The activity variable is used to evaluate the homogeneity of the detector response to background or of the detector noise. The homogeneity h_p of each detector partition can be evaluated using the formula $h_p = \exp(-\sigma_p^R / \langle R \rangle_p)$, where $\langle R \rangle_p$ is the partition mean rate and σ_p^R is the rate standard deviation calculated over the partition channels. The more homogeneously the rates are distributed and the smaller will σ_p^R be, and the closer to 1 will h_p get. On the contrary, if the standard deviation of the channel's rates is large, h_p will rapidly get to 0. This value is saved into histograms as shown in Source Code B.17 and could in the future be used to monitor through time, once extracted, the evolution of every partition homogeneity. This could be of great help to understand the apparition of eventual hot spots due to ageing of the chambers subjected to high radiation levels. The monitored homogeneity information could then be combined with a monitoring of the activity of each individual channel in order to have a finer information. Monitoring tools have been suggested and need to be developed for this purpose.

```

2625   float MeanPartSDev = GetTH1StdDev(StripNoiseProfile_H.rpc[T][S][p]);
2626   float strip_homog = (MeanPartRate==0)
2627     ? 0.
2628     : exp(-MeanPartSDev/MeanPartRate);
2629   StripHomogeneity_H.rpc[T][S][p]->Fill("exp -#left(#frac{\#sigma_{Strip}
2630     \rightarrow Rate}{\#mu_{Strip Rate}}\#right)",strip_homog);
2631   StripHomogeneity_H.rpc[T][S][p]->GetYaxis()->SetRangeUser(0.,1.);
2632
2633   float ChipStDevMean = GetTH1StdDev(ChipMeanNoiseProf_H.rpc[T][S][p]);
2634   float chip_homog = (MeanPartRate==0)
2635     ? 0.
2636     : exp(-ChipStDevMean/MeanPartRate);
2637   ChipHomogeneity_H.rpc[T][S][p]->Fill("exp -#left(#frac{\#sigma_{Chip}
2638     \rightarrow Rate}{\#mu_{Chip Rate}}\#right)",chip_homog);
2639   ChipHomogeneity_H.rpc[T][S][p]->GetYaxis()->SetRangeUser(0.,1.);

2640
2641
2642
2643
2644
2645
2646
2647
2648
2649
2650
2651
2652
2653
2654
2655
2656
2657
2658
2659
2660
2661
2662
2663
2664
2665
2666
2667
2668
2669
2670
2671
2672
2673
2674
2675
2676
2677
2678
2679
2680
2681
2682
2683
2684
2685
2686
2687
2688
2689
2690
2691
2692
2693
2694
2695
2696
2697
2698
2699
2700
2701
2702
2703
2704
2705
2706
2707
2708
2709
2710
2711
2712
2713
2714
2715
2716
2717
2718
2719
2720
2721
2722
2723
2724
2725
2726
2727
2728
2729
2730
2731
2732
2733
2734
2735
2736
2737
2738
2739
2740
2741
2742
2743
2744
2745
2746
2747
2748
2749
2750
2751
2752
2753
2754
2755
2756
2757
2758
2759
2760
2761
2762
2763
2764
2765
2766
2767
2768
2769
2770
2771
2772
2773
2774
2775
2776
2777
2778
2779
2780
2781
2782
2783
2784
2785
2786
2787
2788
2789
2790
2791
2792
2793
2794
2795
2796
2797
2798
2799
2800
2801
2802
2803
2804
2805
2806
2807
2808
2809
2810
2811
2812
2813
2814
2815
2816
2817
2818
2819
2820
2821
2822
2823
2824
2825
2826
2827
2828
2829
2830
2831
2832
2833
2834
2835
2836
2837
2838
2839
2840
2841
2842
2843
2844
2845
2846
2847
2848
2849
2850
2851
2852
2853
2854
2855
2856
2857
2858
2859
2860
2861
2862
2863
2864
2865
2866
2867
2868
2869
2870
2871
2872
2873
2874
2875
2876
2877
2878
2879
2880
2881
2882
2883
2884
2885
2886
2887
2888
2889
2890
2891
2892
2893
2894
2895
2896
2897
2898
2899
2900
2901
2902
2903
2904
2905
2906
2907
2908
2909
2910
2911
2912
2913
2914
2915
2916
2917
2918
2919
2920
2921
2922
2923
2924
2925
2926
2927
2928
2929
2930
2931
2932
2933
2934
2935
2936
2937
2938
2939
2940
2941
2942
2943
2944
2945
2946
2947
2948
2949
2950
2951
2952
2953
2954
2955
2956
2957
2958
2959
2960
2961
2962
2963
2964
2965
2966
2967
2968
2969
2970
2971
2972
2973
2974
2975
2976
2977
2978
2979
2980
2981
2982
2983
2984
2985
2986
2987
2988
2989
2990
2991
2992
2993
2994
2995
2996
2997
2998
2999
2999
3000
3001
3002
3003
3004
3005
3006
3007
3008
3009
3010
3011
3012
3013
3014
3015
3016
3017
3018
3019
3020
3021
3022
3023
3024
3025
3026
3027
3028
3029
3030
3031
3032
3033
3034
3035
3036
3037
3038
3039
3040
3041
3042
3043
3044
3045
3046
3047
3048
3049
3050
3051
3052
3053
3054
3055
3056
3057
3058
3059
3060
3061
3062
3063
3064
3065
3066
3067
3068
3069
3070
3071
3072
3073
3074
3075
3076
3077
3078
3079
3080
3081
3082
3083
3084
3085
3086
3087
3088
3089
3090
3091
3092
3093
3094
3095
3096
3097
3098
3099
3099
3100
3101
3102
3103
3104
3105
3106
3107
3108
3109
3110
3111
3112
3113
3114
3115
3116
3117
3118
3119
3120
3121
3122
3123
3124
3125
3126
3127
3128
3129
3130
3131
3132
3133
3134
3135
3136
3137
3138
3139
3139
3140
3141
3142
3143
3144
3145
3146
3147
3148
3149
3149
3150
3151
3152
3153
3154
3155
3156
3157
3158
3159
3159
3160
3161
3162
3163
3164
3165
3166
3167
3168
3169
3169
3170
3171
3172
3173
3174
3175
3176
3177
3178
3179
3179
3180
3181
3182
3183
3184
3185
3186
3187
3187
3188
3189
3190
3191
3192
3193
3194
3195
3196
3197
3198
3199
3199
3200
3201
3202
3203
3204
3205
3206
3207
3208
3209
3209
3210
3211
3212
3213
3214
3215
3216
3217
3217
3218
3219
3220
3221
3222
3223
3224
3225
3226
3227
3228
3229
3229
3230
3231
3232
3233
3234
3235
3236
3237
3238
3239
3239
3240
3241
3242
3243
3244
3245
3246
3247
3248
3249
3249
3250
3251
3252
3253
3254
3255
3256
3257
3258
3259
3259
3260
3261
3262
3263
3264
3265
3266
3267
3268
3269
3269
3270
3271
3272
3273
3274
3275
3276
3277
3278
3279
3279
3280
3281
3282
3283
3284
3285
3286
3287
3287
3288
3289
3290
3291
3292
3293
3294
3295
3296
3297
3298
3299
3299
3300
3301
3302
3303
3304
3305
3306
3307
3308
3309
3309
3310
3311
3312
3313
3314
3315
3316
3317
3318
3319
3319
3320
3321
3322
3323
3324
3325
3326
3327
3328
3329
3329
3330
3331
3332
3333
3334
3335
3336
3337
3338
3338
3339
3340
3341
3342
3343
3344
3345
3346
3347
3348
3348
3349
3350
3351
3352
3353
3354
3355
3356
3357
3358
3358
3359
3360
3361
3362
3363
3364
3365
3366
3367
3368
3368
3369
3370
3371
3372
3373
3374
3375
3376
3377
3378
3378
3379
3380
3381
3382
3383
3384
3385
3386
3387
3387
3388
3389
3390
3391
3392
3393
3394
3395
3396
3397
3397
3398
3399
3399
3400
3401
3402
3403
3404
3405
3406
3407
3408
3409
3409
3410
3411
3412
3413
3414
3415
3416
3417
3418
3418
3419
3420
3421
3422
3423
3424
3425
3426
3427
3428
3428
3429
3430
3431
3432
3433
3434
3435
3436
3437
3438
3438
3439
3440
3441
3442
3443
3444
3445
3446
3447
3448
3448
3449
3450
3451
3452
3453
3454
3455
3456
3457
3458
3458
3459
3460
3461
3462
3463
3464
3465
3466
3467
3468
3468
3469
3470
3471
3472
3473
3474
3475
3476
3477
3478
3478
3479
3480
3481
3482
3483
3484
3485
3486
3487
3487
3488
3489
3490
3491
3492
3493
3494
3495
3496
3497
3497
3498
3499
3499
3500
3501
3502
3503
3504
3505
3506
3507
3508
3509
3509
3510
3511
3512
3513
3514
3515
3516
3517
3518
3518
3519
3520
3521
3522
3523
3524
3525
3526
3527
3528
3528
3529
3530
3531
3532
3533
3534
3535
3536
3537
3538
3538
3539
3540
3541
3542
3543
3544
3545
3546
3547
3548
3548
3549
3550
3551
3552
3553
3554
3555
3556
3557
3558
3558
3559
3560
3561
3562
3563
3564
3565
3566
3567
3568
3568
3569
3570
3571
3572
3573
3574
3575
3576
3577
3578
3578
3579
3580
3581
3582
3583
3584
3585
3586
3587
3587
3588
3589
3590
3591
3592
3593
3594
3595
3596
3597
3597
3598
3599
3599
3600
3601
3602
3603
3604
3605
3606
3607
3608
3609
3609
3610
3611
3612
3613
3614
3615
3616
3617
3618
3618
3619
3620
3621
3622
3623
3624
3625
3626
3627
3628
3628
3629
3630
3631
3632
3633
3634
3635
3636
3637
3638
3638
3639
3640
3641
3642
3643
3644
3645
3646
3647
3648
3648
3649
3650
3651
3652
3653
3654
3655
3656
3657
3658
3658
3659
3660
3661
3662
3663
3664
3665
3666
3667
3668
3668
3669
3670
3671
3672
3673
3674
3675
3676
3677
3678
3678
3679
3680
3681
3682
3683
3684
3685
3686
3687
3687
3688
3689
3690
3691
3692
3693
3694
3695
3696
3697
3697
3698
3699
3699
3700
3701
3702
3703
3704
3705
3706
3707
3708
3709
3709
3710
3711
3712
3713
3714
3715
3716
3717
3718
3718
3719
3720
3721
3722
3723
3724
3725
3726
3727
3728
3728
3729
3730
3731
3732
3733
3734
3735
3736
3737
3738
3738
3739
3740
3741
3742
3743
3744
3745
3746
3747
3748
3748
3749
3750
3751
3752
3753
3754
3755
3756
3757
3758
3758
3759
3760
3761
3762
3763
3764
3765
3766
3767
3768
3768
3769
3770
3771
3772
3773
3774
3775
3776
3777
3778
3778
3779
3780
3781
3782
3783
3784
3785
3786
3787
3787
3788
3789
3790
3791
3792
3793
3794
3795
3796
3797
3797
3798
3799
3799
3800
3801
3802
3803
3804
3805
3806
3807
3808
3809
3809
3810
3811
3812
3813
3814
3815
3816
3817
3818
3818
3819
3820
3821
3822
3823
3824
3825
3826
3827
3828
3828
3829
3830
3831
3832
3833
3834
3835
3836
3837
3838
3838
3839
3840
3841
3842
3843
3844
3845
3846
3847
3848
3848
3849
3850
3851
3852
3853
3854
3855
3856
3857
3858
3858
3859
3860
3861
3862
3863
3864
3865
3866
3867
3868
3868
3869
3870
3871
3872
3873
3874
3875
3876
3877
3878
3878
3879
3880
3881
3882
3883
3884
3885
3886
3887
3887
3888
3889
3890
3891
3892
3893
3894
3895
3896
3897
3897
3898
3899
3899
3900
3901
3902
3903
3904
3905
3906
3907
3908
3909
3909
3910
3911
3912
3913
3914
3915
3916
3917
3918
3918
3919
3920
3921
3922
3923
3924
3925
3926
3927
3928
3928
3929
3930
3931
3932
3933
3934
3935
3936
3937
3938
3938
3939
3940
3941
3942
3943
3944
3945
3946
3947
3948
3948
3949
3950
3951
3952
3953
3954
3955
3956
3957
3958
3958
3959
3960
3961
3962
3963
3964
3965
3966
3967
3968
3968
3969
3970
3971
3972
3973
3974
3975
3976
3977
3978
3978
3979
3980
3981
3982
3983
3984
3985
3986
3987
3987
3988
3989
3990
3991
3992
3993
3994
3995
3996
3997
3997
3998
3999
3999
4000
4001
4002
4003
4004
4005
4006
4007
4008
4009
4009
4010
4011
4012
4013
4014
4015
4016
4017
4018
4018
4019
4020
4021
4022
4023
4024
4025
4026
4027
4028
4028
4029
4030
4031
4032
4033
4034
4035
4036
4037
4038
4038
4039
4040
4041
4042
4043
4044
4045
4046
4047
4048
4048
4049
4050
4051
4052
4053
4054
4055
4056
4057
4058
4058
4059
4060
4061
4062
4063
4064
4065
4066
4067
4068
4068
4069
4070
4071
4072
4073
4074
4075
4076
4077
4078
4078
4079
4080
4081
4082
4083
4084
4085
4086
4087
4088
4088
4089
4090
4091
4092
4093
4094
4095
4096
4097
4097
4098
4099
4099
4100
4101
4102
4103
4104
4105
4106
4107
4108
4109
4109
4110
4111
4112
4113
4114
4115
4116
4117
4118
4118
4119
4120
4121
4122
4123
4124
4125
4126
4127
4128
4128
4129
4130
4131
4132
4133
4134
4135
4136
4137
4138
4138
4139
4140
4141
4142
4143
4144
4145
4146
4147
4148
4148
4149
4150
4151
4152
4153
4154
4155
4156
4157
4158
4159
4159
4160
4161
4162
4163
4164
4165
4166
4167
4168
4168
4169
4170
4171
4172
4173
4174
4175
4176
4177
4178
4178
4179
4180
4181
4182
4183
4184
4185
4186
4187
4188
4188
4189
4190
4191
4192
4193
4194
4195
4196
4197
4197
4198
4199
4199
4200
4201
4202
4203
4204
4205
4206
4207
4208
4209
4209
4210
4211
4212
4213
4214
4215
4216
4217
4218
4218
4219
4220
4221
4222
4223
4224
4225
4226
4227
4228
4228
4229
4230
4231
4232
4233
4234
4235
4236
4237
4238
4238
4239
4240
4241
4242
4243
4244
4245
4246
4247
4248
4248
4249
4250
4251
4252
4253
4254
4255
4256
4257
4258
4259
4259
4260
4261
4262
4263
4264
4265
4266
4267
4268
4268
4269
4270
4271
4272
4273
4274
4275
4276
4277
4278
4278
4279
4280
4281
4282
4283
4284
4285
4286
4287
4288
4288
4289
4290
4291
4292
4293
4294
4295
4296
4297
4297
4298
4299
4299
4300
4301
4302
4303
4304
4305
4306
4307
4308
4309
4309
4310
4311
4312
4313
4314
4315
4316
4317
4318
4318
4319
4320
4321
4322
4323
4324
4325
4326
4327
4328
4328
4329
4330
4331
4332
4333
4334
4335
4336
4337
4338
4338
4339
4340
4341
4342
4343
4344
4345
4346
4347
4348
4348
4349
4350
4351
4352
4353
4354
4355
4356
4357
4358
4359
4359
4360
4361
4362
4363
4364
4365
4366
4367
4368
4368
4369
4370
4371
4372
4373
4374
4375
4376
4377
4378
4378
4379
4380
4381
4382
4383
4384
4385
4386
4387
4388
4388
4389
4390
4391
4392
4393
4394
4395
4396
4397
4397
4398
4399
4399
4400
4401
4402
4403
4404
4405
4406
4407
4408
4409
4409
4410
4411
4412
4413
4414
4415
4416
4417
4418
4418
4419
4420
4421
4422
4423
4424
4425
4426
4427
4428
4428
4429
4430
4431
4432
4433
4434
4435
4436
4437
4438
4438
4439
4440
4441
4442
4443
4444
4445
4446
4447
4448
4448
4449
4450
4451
4452
4453
4454
4455
4456
4457
4458
4459
4459
4460
4461
4462
4463
4464
4465
4466
4467
4468
4468
4469
4470
4471
4472
4473
4474
4475
4476
4477
4478
4478
4479
4480
4481
4482
4483
4484
4485
4486
4487
4488
4488
4489
4490
4491
4492
4493
4494
4495
4496
4497
4497
4498
4499
4499
4500
4501
4502
4503
4504
4505
4506
4507
4508
4509
4509
4510
4511
4512
4513
4514
4515
4516
4517
4518
4518
451
```

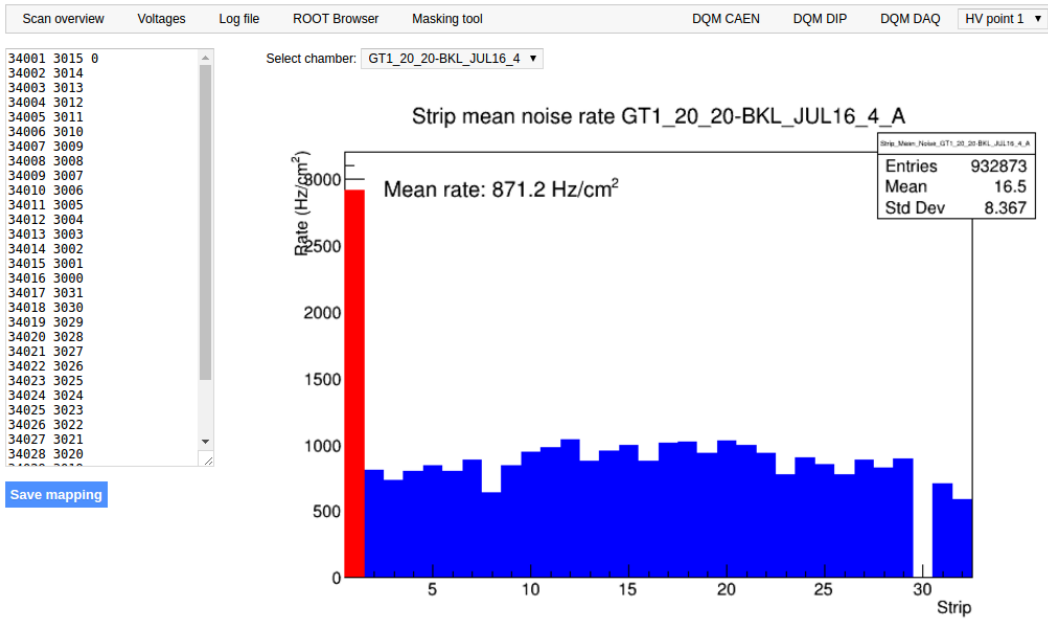


Figure B.3: Display of the masking tool page on the webDCS. The window on the left allows the shifter to edit ChannelsMapping.csv. To mask a channel, it only is needed to set the 3rd field corresponding to the strip to mask to 0. It is not necessary for older mapping file formats to add a 1 for each strip that is not masked as the code is versatile and the default behaviour is to consider missing mask fields as active strips. The effect of the mask is directly visible for noisy channels as the corresponding bin turns red. The global effect of masking strips will be an update of the rate value showed on the histogram that will take into consideration the rejected channels.

2634 From the code point of view, the function `GetTH1Mean()` is used to retrieve the mean rate par-
 2635 tition by partition after the rates have been calculated strip by strip and filled into the histograms
 2636 `StripNoiseProfile_H.rpc[T][S][p]`, as described through Source Code B.18.

2637 Once the mask for each rejected channel has been updated, the shifter can manually run the of-
 2638 fline tool again to update the DQM plots, now including the masked strips, as well the rate results
 2639 written in the output CSV file `Offline-Rate.csv`. If not done during the shifts, the strip masking
 2640 procedure needs to be carefully done by the person in charge of data analysis on the scans that were
 2641 selected to produce the final results.

```

2642
2643     float GetTH1Mean(TH1* H) {
2644         int nBins = H->GetNbinsX();
2645         int nActive = nBins;
2646         float mean = 0.;

2647         for(int b = 1; b <= nBins; b++) {
2648             float value = H->GetBinContent(b);
2649             mean += value;
2650             if(value == 0.) nActive--;
2651         }

2652         if(nActive != 0) mean /= (float)nActive;
2653         else mean = 0.;

2654         return mean;
2655     }

```

Source Code B.18: The function `GetTH1Mean()` is used to return the mean along the y-axis of `TH1` histograms containing rate information. In order to take into account masked strips whose rate is set to 0, the function looks for masked channels and decrement the number of active channels for each null value found.

2645 B.6.4.4 Output CSV files filling

2646 All the histograms have been filled. Parameters will then be extracted from them to compute the
 2647 final results that will later be used to produce plots. Once the results have been computed, the very
 2648 last step of the offline macro is to write these values into the corresponding CSV outputs. Aside of
 2649 the file `Offline-Corrupted.csv`, 2 CSV files are being written by the macro `offlineAnalysis()`,
 2650 `Offline-Rates.csv` and `Offline-L0-EffCl.csv` that respectively contain information about noise
 2651 or gamma rates, cluster size and multiplicity, and about level 0 reconstruction of the detector effi-
 2652 ciency, muon cluster size and multiplicity. Details on the computation and file writing are respec-
 2653 tively given in Sources Codes B.19 and B.20.

2654 **Noise/gamma background variables** are computed and written in the output file for each detector
 2655 partitions. A detector average of the hit and cluster rate is also provided, as shown through Sources
 2656 Code B.19. The variables that are written for each partition are:

- 2657 • The mean partition hit rate per unit area, `MeanPartRate`, that is extracted from the histogram
 2658 `StripNoiseProfile_H` as the mean value along the y-axis, as described in section B.6.4.3. No
 2659 error is recorded for the hit rate as this is considered a single measurement. No statistical error
 2660 can be associated to it and the systematics are unknown.
- 2661 • The mean cluster size, `cSizePart`, is extracted from the histogram `NoiseCSize_H` and it's
 2662 statistical error, `cSizePartErr`, is taken to be 2σ of the total distribution.
- 2663 • The mean cluster multiplicity per trigger, `cMultPart`, is extracted from the histogram `NoiseCMult_H`
 2664 and it's statistical error, `cMultPartErr`, is taken to be 2σ of the total distribution. It is impor-
 2665 tant to point to the fact that this variable gives an information that is dependent on the buffer
 2666 window width used for each trigger for the calculation.
- 2667 • The mean cluster rate per unit area, `ClustPartRate`, is defined as the mean hit rate normalised

2668 to the mean cluster size and it's statistical error, `ClustPartRateErr`, is then obtained using the
 2669 relative statistical error on the mean cluster size.

```

for (UInt tr = 0; tr < GIFInfra->GetNTrolleys(); tr++) {
  UInt T = GIFInfra->GetTrolleyID(tr);

  for (UInt sl = 0; sl < GIFInfra->GetNSlots(tr); sl++) {
    UInt S = GIFInfra->GetSlotID(tr,sl) - 1;

    float MeanNoiseRate = 0.;
    float ClusterRate = 0.;
    float ClusterSDev = 0.;

    for (UInt p = 0; p < GIFInfra->GetNPartitions(tr,sl); p++) {
      float MeanPartRate = GetTH1Mean(StripNoiseProfile_H.rpc[T][S][p]);
      float cSizePart = NoiseCSIZE_H.rpc[T][S][p]->GetMean();
      float cSizePartErr = (NoiseCSIZE_H.rpc[T][S][p]->GetEntries()==0)
        ? 0.
        : 2*NoiseCSIZE_H.rpc[T][S][p]->GetStdDev() /
          sqrt(NoiseCSIZE_H.rpc[T][S][p]->GetEntries());
      float cMultPart = NoiseCMult_H.rpc[T][S][p]->GetMean();
      float cMultPartErr = (NoiseCMult_H.rpc[T][S][p]->GetEntries()==0)
        ? 0.
        : 2*NoiseCMult_H.rpc[T][S][p]->GetStdDev() /
          sqrt(NoiseCMult_H.rpc[T][S][p]->GetEntries());
      float ClustPartRate = (cSizePart==0) ? 0.
        : MeanPartRate/cSizePart;
      float ClustPartRateErr = (cSizePart==0) ? 0.
        : ClustPartRate * cSizePartErr/cSizePart;

      outputRateCSV << MeanPartRate << '\t'
        << cSizePart << '\t' << cSizePartErr << '\t'
        << cMultPart << '\t' << cMultPartErr << '\t'
        << ClustPartRate << '\t' << ClustPartRateErr << '\t';

      RPCarea += stripArea * nStripsPart;
      MeanNoiseRate += MeanPartRate * stripArea * nStripsPart;
      ClusterRate += ClustPartRate * stripArea * nStripsPart;
      ClusterSDev += (cSizePart==0)
        ? 0.
        : ClusterRate*cSizePartErr/cSizePart;
    }

    MeanNoiseRate /= RPCarea;
    ClusterRate /= RPCarea;
    ClusterSDev /= RPCarea;

    outputRateCSV << MeanNoiseRate << '\t'
      << ClusterRate << '\t' << ClusterSDev << '\t';
  }
}

```

2671 *Source Code B.19: Description of rate result calculation and writing into the CSV output Offline-Rate.csv.
 Are saved into the file for each detector, the mean partition rate, cluster size and cluster mutiplicity, along with
 their errors, for each partition and as well as a detector average.*

2672 **Muon performance variables** are computed and written in the output file for each detector parti-
 2673 tions as shown through Sources Code B.20. The variables that are written for each partition are:

- 2674 ● The muon efficiency, `eff`, extracted from the histogram `Efficiency0_H`. It is reminded that
2675 this offline tool doesn't include any tracking algorithm to identify muons from the beam and
2676 only relies on the hits arriving in the time window corresponding to the beam time. The con-
2677 tent of the efficiency histogram is thus biased by the noise/gamma background contribution
2678 into this window and is thus corrected by estimating the muon data content in the peak re-
2679 gion knowing the noise/gamma content in the rate calculation region. Both time windows
2680 being different, the choice was made to normalise the noise/gamma background calculation
2681 window to it's equivalent beam window in order to have comparable values using the variable
2682 `windowRatio`. Finally, to estimate the data ratio in the peak region, the variable `DataRatio`
2683 is defined as the ratio in between the estimated mean cluster multiplicity of the muons in the
2684 peak region, `MuonCM`, and of the total mean cluster multiplicity in the peak region, `PeakCM`.
2685 `MuonCM` is itself defined as the difference in between the total mean cluster multiplicity in the
2686 peak region and the normalised mean noise/gamma cluster multiplicity calculated outside of
2687 the peak region. The statistical error related to the efficiency, `eff_err`, is computed using a
2688 binomial distribution, as the efficiency measure the probability of "success" and "failure" to
2689 detect muons.
- 2690 ● The mean muon cluster size, `MuonCS`, is calculated using the total mean cluster size and multi-
2691 plicity in the peak region, respectively extracted from histograms `MuonCSize_H` and `MuonCMult_H`,
2692 the noise/gamma background mean cluster size and normalised multiplicity, extracted from
2693 `NoiseCSize_H` and `NoiseCMult_H`, and of the estimated muon cluster multiplicity `MuonCM` pre-
2694 viously explicated. The associated statistical error, `MuonCM_err`, is calculated using the propa-
2695 gation of errors of the mentioned variables.
- 2696 ● The mean muon cluster multiplicity in the peak region, `MuonCM`, explicated above whose sta-
2697 tistical error, `MuonCM_err`, is the sum of statistical error associated to the total mean clus-
2698 ter multiplicity in the peak reagion, `PeakCM_err`, and of the mean noise/gamma cluster size,
2699 `NoiseCM_err`.

2700 In addition to these 2 CSV files, the histograms are saved in ROOT file `Scan00XXXX_HVY_Offline.root`
2701 as explained in section B.2.1.1.

2702

```

for (UInt tr = 0; tr < GIFInfra->GetNTrolleys(); tr++) {
    UInt T = GIFInfra->GetTrolleyID(tr);
    for (UInt sl = 0; sl < GIFInfra->GetNSlots(tr); sl++) {
        UInt S = GIFInfra->GetSlotID(tr,sl) - 1;
        for (UInt p = 0; p < GIFInfra->GetNPartitions(tr,sl); p++) {
            float noiseWindow =
                BMTDCWINDOW - TIMEREJECT - 2*PeakWidth.rpc[T][S][p];
            float peakWindow = 2*PeakWidth.rpc[T][S][p];
            float windowRatio = peakWindow/noiseWindow;

            float PeakCM = MuonCMult_H.rpc[T][S][p]->GetMean();
            float PeakCS = MuonCSize_H.rpc[T][S][p]->GetMean();
            float NoiseCM = NoiseCMult_H.rpc[T][S][p]->GetMean() *windowRatio;
            float NoiseCS = NoiseCSize_H.rpc[T][S][p]->GetMean();
            float MuonCM = (PeakCM<NoiseCM) ? 0. : PeakCM-NoiseCM;
            float MuonCS = (MuonCM==0 || PeakCM*PeakCS<NoiseCM*NoiseCS)
                ? 0.
                : (PeakCM*PeakCS-NoiseCM*NoiseCS) / MuonCM;
            float PeakCM_err = (MuonCMult_H.rpc[T][S][p]->GetEntries()==0.)
                ? 0.
                : 2*MuonCMult_H.rpc[T][S][p]->GetStdDev() /
                    sqrt(MuonCMult_H.rpc[T][S][p]->GetEntries());
            float PeakCS_err = (MuonCSize_H.rpc[T][S][p]->GetEntries()==0.)
                ? 0.
                : 2*MuonCSize_H.rpc[T][S][p]->GetStdDev() /
                    sqrt(MuonCSize_H.rpc[T][S][p]->GetEntries());
            float NoiseCM_err = (NoiseCMult_H.rpc[T][S][p]->GetEntries()==0.)
                ? 0.
                : windowRatio*2*NoiseCMult_H.rpc[T][S][p]->GetStdDev() /
                    sqrt(NoiseCMult_H.rpc[T][S][p]->GetEntries());
            float NoiseCS_err = (NoiseCSize_H.rpc[T][S][p]->GetEntries()==0.)
                ? 0.
                : 2*NoiseCSize_H.rpc[T][S][p]->GetStdDev() /
                    sqrt(NoiseCSize_H.rpc[T][S][p]->GetEntries());
            float MuonCM_err = (MuonCM==0) ? 0. : PeakCM_err+NoiseCM_err;
            float MuonCS_err = (MuonCS==0 || MuonCM==0) ? 0.
                : (PeakCS*PeakCM_err + PeakCM*PeakCS_err +
                    NoiseCS*NoiseCM_err + NoiseCM*NoiseCS_err +
                    MuonCS*MuonCM_err) / MuonCM;

            float DataRatio = MuonCM/PeakCM;
            float DataRatio_err = (MuonCM==0) ? 0.
                : DataRatio*(MuonCM_err/MuonCM + PeakCM_err/PeakCM);
            float eff = DataRatio*Efficiency0_H.rpc[T][S][p]->GetMean();
            float eff_err = DataRatio*2*Efficiency0_H.rpc[T][S][p]->GetStdDev() /
                sqrt(Efficiency0_H.rpc[T][S][p]->GetEntries()) +
                Efficiency0_H.rpc[T][S][p]->GetMean()*DataRatio_err;

            outputEffCSV << eff << '\t' << eff_err << '\t'
                << MuonCS << '\t' << MuonCS_err << '\t'
                << MuonCM << '\t' << MuonCM_err << '\t';
        }
    }
}

```

2703

2704

Source Code B.20: Description of efficiency result calculation and writing into the CSV output Offline-L0-EffCl.csv. Are saved into the file for each detector, the efficiency, corrected taking into account the background in the peak window of the time profile, muon cluster size and muon cluster multiplicity, along with their errors, for each partition and as well as a detector average.

2705 B.7 Current data Analysis

2706 Detectors under test at GIF++ are connected both to a CAEN HV power supply and to a CAEN
2707 ADC that reads the currents inside of the RPC gaps bypassing the supply cable. During data tak-
2708 ing, the webDCS records into a ROOT file called `Scan00XXXX_HVY_CAEN.root` histograms with the
2709 monitored parameters of both CAEN devices. Are recorded for each RPC channels (in most cases,
2710 a channel corresponds to an RPC gap):

- 2711 • the effective voltage, HV_{eff} , set by the webDCS using the PT correction on the CAEN power
2712 supply,
- 2713 • the applied voltage, HV_{app} , monitored by the CAEN power supply, and the statistical error
2714 related to the variations of this value through time to follow the variation of the environmental
2715 parameters defined as the RMS of the histogram divided by the square root of the number of
2716 recorded points,
- 2717 • the monitored current, I_{mon} , monitored by the CAEN power supply, and the statistical error
2718 related to the variations of this value through time to follow the variation of the environmental
2719 parameters defined as the RMS of the histogram divided by the square root of the number of
2720 recorded points,
- 2721 • the corresponding current density, J_{mon} , defined as the monitored current per unit area,
2722 $J_{mon} = I_{mon}/A$, where A is the active area of the corresponding gap,
- 2723 • the ADC current, I_{ADC} , recorded through the CAEN ADC module that monitors the dark
2724 current in the gap itself. First of all, the resolution of such a module is better than that of
2725 CAEN power supplies and moreover, the current is not read-out through the HV supply line
2726 but directly at the chamber level giving the real current inside of the detector. The statistical
2727 error is defined as the RMS of the histogram distribution divided by the square root of the
2728 number of recorded points.

2729 Once extracted through a loop over the element of GIF++ infrastructure via the C++ macro
2730 `GetCurrent()`, these parameters, organised in 9 columns per detector HV supply line, are written in
2731 the output CSV file `Offline-Current.csv`. The macro can be found in the file `Current.cc`.

References

- [1] T. Massam et al. “Experimental observation of antideuteron production”. In: *Il Nuovo Cimento A* 63 (1965), pp. 10–14.
- [2] UA1 Collaboration. “Experimental observation of isolated large transverse energy electrons with associated missing energy at $s = 540 \text{ GeV}$ ”. In: *Physics Letters B* 122 (1983), pp. 103–116.
- [3] UA2 Collaboration. “Observation of single isolated electrons of high transverse momentum in events with missing transverse energy at the CERN pp collider”. In: *Physics Letters B* 122 (1983), pp. 476–485.
- [4] UA1 Collaboration. “Experimental observation of lepton pairs of invariant mass around $95 \text{ GeV}/c^2$ at the CERN SPS collider”. In: *Physics Letters B* 126 (1983), pp. 398–410.
- [5] UA2 Collaboration. “Evidence for $Z_0 \rightarrow e^+e^-$ at the CERN pp collider”. In: *Physics Letters B* 129 (1983), pp. 130–140.
- [6] ALEPH Collaboration. “Determination of the number of light neutrino species”. In: *Physics Letters B* 231 (1989), pp. 519–529.
- [7] CERN, ed. (1985).
- [8] CERN, ed. (1986).
- [9] CERN, ed. (1994).
- [10] CERN, ed. (1998).
- [11] CERN, ed. (1999).
- [12] CERN. Geneva. LHC Experiments Committee. *Letter of Intent for A Large Ion Collider Experiment [ALICE]*, note = CERN-LHCC-93-016. Tech. rep. ALICE Collaboration, 1993.
- [13] CERN. Geneva. LHC Experiments Committee. *ATLAS : technical proposal for a general-purpose pp experiment at the Large Hadron Collider at CERN*, note = CERN-LHCC-94-43. Tech. rep. ATLAS Collaboration, 1994.
- [14] CERN. Geneva. LHC Experiments Committee. *CMS : letter of intent by the CMS Collaboration for a general purpose detector at LHC*, note = CERN-LHCC-92-003. Tech. rep. CMS Collaboration, 1992.
- [15] CERN. Geneva. LHC Experiments Committee. *LHCb : letter of intent*. Tech. rep. CERN-LHCC-95-5. LHCb Collaboration, 1995.
- [16] L. Evans and P. Bryant. “LHC Machine”. In: *JINST* 3 (2008). S08001.
- [17] CMS Collaboration ATLAS Collaboration. “Combined Measurement of the Higgs Boson Mass in pp Collisions at $\sqrt{s} = 7$ and 8 TeV with the ATLAS and CMS Experiments”. In: *Physical Review Letters* 114 (2015). 191803.
- [18] LHCb Collaboration. “Observation of $J/\psi p$ Resonances Consistent with Pentaquark States in $\Lambda_b^0 \rightarrow J/\psi K^- p$ Decays”. In: *Physical Review Letters* 115 (2015). 072001.

- [19] LHCb Collaboration. “Observation of $J/\psi\phi$ Structures Consistent with Exotic States from Amplitude Analysis of $B^+ \rightarrow J/\psi\phi K^+$ Decays”. In: *Physical Review Letters* 118 (2017). 022003.
- [20] CERN. Geneva. *High-Luminosity Large Hadron Collider (HL-LHC) Technical Design Report V. 0.1*. Tech. rep. CERN-2017-007-M. 2017.
- [21] CERN. Geneva. LHC Experiments Committee. *The CMS muon project : Technical Design Report*. Tech. rep. CERN-LHCC-97-032. CMS Collaboration, 1997.
- [22] CERN. Geneva. LHC Experiments Committee. *Technical Proposal for the Phase-II Upgrade of the CMS Detector*. Tech. rep. CERN-LHCC-2015-010. CMS Collaboration, 2015.
- [23] CERN. Geneva. LHC Experiments Committee. *CMS, the Compact Muon Solenoid : technical proposal*. Tech. rep. CERN-LHCC-94-38. CMS Collaboration, 1994.
- [24] R. Santonico and R. Cardarelli. “Development of resistive plate counters”. In: *Nucl. Instr. Meth. Phys. Res.* 187 (1981), pp. 377–380.
- [25] Yu.N. Pestov and G.V. Fedotovich. *A picosecond time-of-flight spectrometer for the VEPP-2M based on local-discharge spark counter*. Tech. rep. SLAC-TRANS-0184. SLAC, 1978.
- [26] W.W. Ash, ed. *Spark Counter With A Localized Discharge*. Vol. SLAC-R-250. 1982, pp. 127–131.
- [27] I. Crotty et al. “The non-spark mode and high rate operation of resistive parallel plate chambers”. In: *NIMA* 337 (1993), pp. 370–381.
- [28] I. Crotty et al. “Further studies of avalanche mode operation of resistive parallel plate chambers”. In: *NIMA* 346 (1994), pp. 107–113.
- [29] R. Cardarelli et al. “Avalanche and streamer mode operation of resistive plate chambers”. In: *NIMA* 382 (1996), pp. 470–474.
- [30] E. Cerron Zeballos et al. “A new type of resistive plate chamber: The multigap RPC”. In: *NIMA* 374 (1996), pp. 132–135.
- [31] M.C.S. Williams. “The development of the multigap resistive plate chamber”. In: *Nucl. Phys. B* 61 (1998), pp. 250–257.
- [32] H. Czyrkowski et al. “New developments on resistive plate chambers for high rate operation”. In: *NIMA* 419 (1998), pp. 490–496.
- [33] P. Camarri et al. “Streamer suppression with SF₆ in RPCs operated in avalanche mode”. In: *NIMA* 414 (1998), pp. 317–324.
- [34] E. Cerron Zeballos et al. “Effect of adding SF₆ to the gas mixture in a multigap resistive plate chamber”. In: *NIMA* 419 (1998), pp. 475–478.
- [35] CERN. Geneva. LHC Experiments Committee. *ATLAS muon spectrometer: Technical design report*. Tech. rep. CERN-LHCC-97-22. ATLAS Collaboration, 1997.
- [36] CERN. Geneva. LHC Experiments Committee. *ALICE Time-Of-Flight system (TOF) : Technical Design Report*. Tech. rep. CERN-LHCC-2000-012. ALICE Collaboration, 2000.
- [37] The CALICE collaboration. “First results of the CALICE SDHCAL technological prototype”. In: *JINST* 11 (2016).
- [38] PoS, ed. *Density Imaging of Volcanoes with Atmospheric Muons using GRPCs*. International Europhysics Conference on High Energy Physics - HEP 2011. 2011.
- [39] C. Lippmann. “Detector Physics of Resistive Plate Chambers”. PhD thesis. Johann Wolfgang Goethe-Universität, 2003.

BIBLIOGRAPHY

- 2811 [40] M. Abbrescia et al. “Properties of C₂H₂F₄-based gas mixture for avalanche mode operation
2812 of resistive plate chambers”. In: *NIMA* 398 (1997), pp. 173–179.
- 2813 [41] G.Battistoni et al. “Sensitivity of streamer mode to single ionization electrons”. In: *NIMA*
2814 235 (1985), pp. 91–97.
- 2815 [42] W. Riegler. “Induced signals in resistive plate chambers”. In: *NIMA* 491 (2002), pp. 258–271.
- 2816 [43] E. Cerron Zeballos et al. “A comparison of the wide gap and narrow gap resistive plate
2817 chamber”. In: *NIMA* 373 (1996), pp. 35–42.
- 2818 [44] M. Abbrescia et al. “Cosmic ray tests of double-gap resistive plate chambers for the CMS
2819 experiment”. In: *NIMA* 550 (2005), pp. 116–126.
- 2820 [45] ALICE Collaboration. “A study of the multigap RPC at the gamma irradiation facility at
2821 CERN”. In: *NIMA* 490 (2002), pp. 58–70.
- 2822 [46] B. Bonner et al. “A multigap resistive plate chamber prototype for time-of-flight for the STAR
2823 experiment at RHIC”. In: *NIMA* 478 (2002), pp. 176–179.
- 2824 [47] S. Yang et al. “Test of high time resolution MRPC with different readout modes for the
2825 BESIII upgrade”. In: *NIMA* 763 (2014), pp. 190–196.
- 2826 [48] A. Akindinov et al. “RPC with low-resistive phosphate glass electrodes as a candidate for
2827 the CBM TOF”. In: *NIMA* 572 (2007), pp. 676–681.
- 2828 [49] JINST, ed. *Development of the MRPC for the TOF system of the MultiPurpose Detector.*
2829 RPC2016: XII Workshop on Resistive Plate Chambers and Related Detectors. 2016.
- 2830 [50] M.C.S. Williams. “Particle identification using time of flight”. In: *Journal of Physics G* 39
2831 (2012).
- 2832 [51] A. Alici et al. “Aging and rate effects of the Multigap RPC studied at the Gamma Irradiation
2833 Facility at CERN”. In: *NIMA* 579 (2007), pp. 979–988.
- 2834 [52] M. Abbrescia et al. “The simulation of resistive plate chambers in avalanche mode: charge
2835 spectra and efficiency”. In: *NIMA* 431 (1999), pp. 413–427.
- 2836 [53] M. Abbrescia et al. “Study of long-term performance of CMS RPC under irradiation at the
2837 CERN GIF”. In: *NIMA* 533 (2004), pp. 102–106.
- 2838 [54] H.C. Kim et al. “Quantitative aging study with intense irradiation tests for the CMS forward
2839 RPCs”. In: *NIMA* 602 (2009), pp. 771–774.
- 2840 [55] S. Agosteo et al. “A facility for the test of large-area muon chambers at high rates”. In: *NIMA*
2841 452 (2000), pp. 94–104.
- 2842 [56] PoS, ed. *CERN GIF ++ : A new irradiation facility to test large-area particle detectors for*
2843 *the high-luminosity LHC program*. Vol. TIPP2014. 2014, pp. 102–109.
- 2844 [57] A. Fagot. *GIF++ DAQ v4.0*. 2017. URL: https://github.com/afagot/GIF_DAQ.
- 2845 [58] CAEN. *Mod. V1190-VX1190 A/B, 128/64 Ch Multihit TDC*. 14th ed. 2016.
- 2846 [59] CAEN. *Mod. V1718 VME USB Bridge*. 9th ed. 2009.
- 2847 [60] W-Ie-Ne-R. *VME 6021-23 VXI*. 5th ed. 2016.
- 2848 [61] Wikipedia. *INI file*. 2017. URL: https://en.wikipedia.org/wiki/INI_file.
- 2849 [62] S. Carrillo A. Fagot. *GIF++ Offline Analysis v6*. 2017. URL: https://github.com/afagot/GIF_OfflineAnalysis.